SANDIA REPORT

SAND99–0635
Unlimited Release
Printed March 1999

Failure Surfaces and Related Mechanical Properties for Poled and Unpoled PZT 95/5-2Nb Voltage Bar Ceramic

D. H. Zeuch, S. T. Montgomery, L. W. Carlson, and J. M. Grazier

Prepared by
Sandia National Laboratories
Albuquerque, New Mexico 87185 and Livermore, California 94550

Sandia is a multiprogram laboratory operated by Sandia Corporation, a Lockheed Martin Company, for the United States Department of Energy under Contract DE-AC04-94AL85000.

Sandia National Laboratories

Issued by Sandia National Laboratories, operated for the United States Depart-ment of Energy by Sandia Corporation.

Available to DOE and DOE contractors from
Office of Scientific and Technical Information
P.O. Box 62
Oak Ridge, TN 37831

Prices available from (703) 605-6000
Web site: http://www.ntis.gov/ordering.htm

Available to the public from
National Technical Information Service
U.S. Department of Commerce
5285 Port Royal Rd
Springfield, VA 22161

NTIS price codes
Printed copy: A06
Microfiche copy: A01

SAND99-0635
Unlimited Release
Printed March 1999

Failure Surfaces and Related Mechanical Properties for Poled and Unpoled PZT 95/5-2Nb Voltage Bar Ceramic

D. H. Zeuch
Geomechanics Department

S. T. Montgomery
Integrated Product Development Department

L. W. Carlson and J. M. Grazier
Geomechanics Department

P.O. Box 5800
Sandia National Laboratories
Albuquerque, NM 87185-0751

Abstract

Thirty-six triaxial compression experiments were performed at room temperature on jacketed, PZT 95/5-2Nb ceramic specimens from a single hifire. Confining pressures ranged from ambient to 800 MPa, and strain rates were 10^{-2} or $10^{-4}s^{-1}$. Approximately half of the experiments were conducted on specimens poled transverse to the axis of deviatoric loading ("normal mode") and the remainder were conducted on specimens poled parallel to the axis of deviatoric loading ("axial mode"). At a strain rate of $10^{-4}s^{-1}$, compressive strength under unconfined conditions is approximately 558 MPa. Strength increases to approximately 940 MPa at a confining pressure of 400 MPa. Interestingly, the two experiments conducted at a confining pressure of 800 MPa exhibited strengths comparable to the specimens tested at σ_3=400 MPa, suggesting that some sort of strength limit was reached between these two pressures at $10^{-4}s^{-1}$. It also appears the pore collapse begins somewhere between 400 and 800 MPa. A similar trend was observed at a strain rate of $10^{-2}s^{-1}$. Under unconfined conditions, compressive strength is approximately 663 MPa, increasing to 1044 MPa at σ_3=400 MPa. Under unconfined conditions, the two-order-of-magnitude increase in strain rate results in a 19% increase in strength; at 400 MPa, the same increase leads to an

11% increase in compressive strength. The usual transition in failure modes with increasing confining pressure–from axial splitting to discrete shear failure to distributed microcracking–was observed. As expected, the relationship between poling direction and axis of compression had no clearly detectable influence on strength. A series of experiments on unpoled ceramic confirmed that this hifire behaves similarly to others that we have characterized in the recent past.

Contents

1 Introduction **1**

2 Experimental Material and Techniques **7**
2.1 Experimental Materials 7
2.2 Experimental Techniques 8

3 Experimental Results: Triaxial Compression Experiments on Poled Ceramic **15**
3.1 A Few Preliminary Remarks on Transformation Effects and Stress-Strain Data 15
3.2 Effect of Confining Pressure on Compressive Strength and Ductility 23
3.3 Effect of Strain Rate on Compressive Strength 28
3.4 Orientation Effects 30
3.4.1 Strength and Ductility 30
3.4.2 Stress-Strain Response: Elastic, Dipole Rotation and Transformation Effects 31
3.4.3 Effect of Poling Direction on Onset of the $F_{R1} \rightarrow A_O$ Transformation in Triaxial Compression 38
3.5 Additional Observations on Poled 453 Ceramic 40

4 Experimental Results: Confirmatory Experiments on Unpoled Ceramic **51**
4.1 Uniaxial Compression Experiments: Strength and Elastic Properties 51
4.2 Hydrostatic Compression and Constant-Stress-Difference Experiments 54

5 Discussion and Conclusions **63**

6 References **67**

A Hifire 453: Normal–Mode Experiments at $\dot{\epsilon}$=10^{-4} s^{-1} 71

B Hifire 453: Normal–Mode Experiments at $\dot{\epsilon}$=10^{-2} s^{-1} 77

C Hifire 453: Axial–Mode Experiments at $\dot{\epsilon}$=10^{-4} s^{-1} 83

D Hifire 453: Axial–Mode Experiments at $\dot{\epsilon}$=10^{-2} s^{-1} 89

E Hifire 424: Uniaxial Compression Experiments on Unpoled Ceramic 95

F Hifire 541-1: Uniaxial Compression Experiments on Unpoled Ceramic 99

G Hifire 541-1: Uniaxial Compression Experiments on Poled Ceramic 103

H Hifire 453: Hydrostatic Compression and CSD Experiments on Unpoled Ceramic 105

List of Figures

1.1 Pressure-temperature phase diagram for PZT 95/5-2Nb. . . . 2

2.1 Distribution of large pores formed by added Lucite microspheres. 9
2.2 Stages in specimen assembly. 10
2.3 Apparatus used in this investigation. 12

3.1 Normal-mode uniaxial compression experiment at $\dot{\epsilon}=10^{-4}s^{-1}$. . 18
3.2 Normal-mode, triaxial compression experiment at $\dot{\epsilon}=10^{-4}s^{-1}$ and σ_3=100 MPa. 19
3.3 Normal-mode, triaxial compression experiment at $\dot{\epsilon}=10^{-4}s^{-1}$ and σ_3=200 MPa. 20
3.4 Normal-mode, triaxial compression experiment at $\dot{\epsilon}=10^{-4}s^{-1}$ and σ_3=400 MPa. 21
3.5 Normal-mode, triaxial compression experiment at $\dot{\epsilon}=10^{-4}s^{-1}$ and σ_3=800 MPa. 22
3.6 Axial-mode, uniaxial compression experiment at $\dot{\epsilon}=10^{-4}s^{-1}$. . 23
3.7 Axial-mode, triaxial compression experiment at $\dot{\epsilon}=10^{-4}s^{-1}$ and σ_3=100 MPa. 24
3.8 Axial-mode, triaxial compression experiment at $\dot{\epsilon}=10^{-4}s^{-1}$ and σ_3=200 MPa. 25
3.9 Axial-mode, triaxial compression experiment at $\dot{\epsilon}=10^{-4}s^{-1}$ and σ_3=400 MPa. 26
3.10 Detailed view of the lateral strains for the normal-mode uniaxial compression experiment shown in Figure 3.1. 27
3.11 Detailed view of the lateral strains for the axial-mode uniaxial compression experiment shown in Figure 3.6. 28
3.12 Hydrostatic compression stages of triaxial compression experiments performed at σ_3=400 or 800 MPa. 29
3.13 Failure modes at various confining pressures. 30
3.14 Summary plot of the effects of confining pressure on strength and ductility for normal-mode deformation at $\dot{\epsilon}=10^{-4}s^{-1}$. . . . 31

3.15 Summary plot of the effects of confining pressure on strength and ductility for axial-mode deformation at $\dot{\epsilon}$=10^{-4}s^{-1}. 32
3.16 Summary plot of the effects of confining pressure on strength and ductility for normal-mode deformation at $\dot{\epsilon}$=10^{-2}s^{-1}. . . . 33
3.17 Summary plot of the effects of confining pressure on strength and ductility for axial-mode deformation at $\dot{\epsilon}$=10^{-2}s^{-1}. 34
3.18 Summary plot of the effects of confining pressure and strain rate on the strength of poled, hifire 453 ceramic. 35
3.19 Stress difference *vs.* volume strain for normal-mode experiments at $\dot{\epsilon}$=10^{-4}s^{-1}. 36
3.20 Stress difference *vs.* volume strain for axial-mode experiments at $\dot{\epsilon}$=10^{-4}s^{-1}. 37
3.21 Normal- and axial-mode, uniaxial compression experiments on hifire 453 ceramic. 38
3.22 Anisotropic strain behavior of poled PZT 95/5-2Nb ceramic during the $F_{R1} \rightarrow A_O$ transformation under hydrostatic compression. 42
3.23 Plots of mean stress *vs.* volume strain for normal-mode, uniaxial and triaxial compression experiments at $\dot{\epsilon}$=10^{-4}s^{-1} and confining pressures $\leq$200 MPa. 43
3.24 Plots of mean stress *vs.* volume strain for axial-mode, uniaxial and triaxial compression experiments at $\dot{\epsilon}$=10^{-4}s^{-1} and confining pressures $\leq$200 MPa. 44
3.25 Top: Plots of pressure *vs.* time for the hydrostatic compression stages of experiments conducted at 400 or 800 MPa. Bottom: Plots of mean stress *vs.* time for the same normal-mode experiments shown in Fig. 3.24. 45
3.26 Plots of mean stress *vs.* volume strain for normal-mode, uniaxial and triaxial compression experiments at $\dot{\epsilon}$=10^{-2}s^{-1} and confining pressures $\leq$200 MPa. 46
3.27 Plots of mean stress *vs.* volume strain for axial-mode, uniaxial and triaxial compression experiments at $\dot{\epsilon}$=10^{-2}s^{-1} and confining pressures $\leq$200 MPa. 47
3.28 Top: Plot of stress-difference *vs.* volume strain for normal-mode, uniaxial and triaxial compression experiments at $\dot{\epsilon}$=10^{-4}s^{-1} and confining pressures $\leq$200 MPa. Bottom: Plots of mean stress *vs.* volume strain for the same experiments shown above. 48
3.29 Plots of σ_1 and mean stress *vs.* time for three normal-mode experiments at $\dot{\epsilon}$=10^{-4}s^{-1}. 49

3.30 Plots of $\frac{\sigma_1+\sigma_3}{2}$ *vs.* volume strain for normal-mode (top), and axial-mode (bottom) uniaxial and triaxial compression experiments at $\dot{\epsilon}$=10^{-2}s^{-1} and confining pressures $\leq$200 MPa. . . . 50

4.1 Uniaxial compression experiment at 10^{-4} s^{-1} on unpoled 453 ceramic. Capacitance is plotted *vs.* volume strain on the right abscissa. 52
4.2 Uniaxial compression experiment at 10^{-4} s^{-1} on unpoled 453 ceramic. Capacitance is plotted *vs.* volume strain on the right abscissa. 53
4.3 Plot of mean stress or pressure *vs.* volume strain for hydrostatic and uniaxial compression, and constant-stress-difference experiments on unpoled, hifire 453 ceramic. 56
4.4 Plot of capacitance *vs.* pressure for hydrostatic compression experiments on unpoled 453 ceramic. 57
4.5 Plot of capacitance *vs.* mean stress for constant-stress-difference experiments on unpoled 453 ceramic at $\sigma_1 - \sigma_3$=50 MPa. . . . 58
4.6 Plot of capacitance *vs.* mean stress for constant-stress-difference experiments on unpoled 453 ceramic at $\sigma_1 - \sigma_3$=100 MPa. . . 59
4.7 Plot of capacitance *vs.* mean stress for constant-stress-difference experiments on unpoled 453 ceramic at $\sigma_1 - \sigma_3$=150 MPa. . . 60
4.8 Plots of pressure or σ_1 *vs.* volume strain for selected uniaxial and hydrostatic compression, and constant-stress-difference experiments on hifire 453 ceramic. 61
4.9 Plot of peak capacitance *vs.* pressure, or corrected values of σ_1 or mean stress. 62

A.1 Normal–mode, unconfined, $\dot{\epsilon}$=10^{-4} s^{-1}. 72
A.2 Normal–mode, unconfined, $\dot{\epsilon}$=10^{-4} s^{-1}. 72
A.3 Normal–mode, σ_3 =100 MPa, $\dot{\epsilon}$=10^{-4} s^{-1}. 73
A.4 Normal–mode, σ_3 =100 MPa, $\dot{\epsilon}$=10^{-4} s^{-1}. 73
A.5 Normal–mode, σ_3 =200 MPa, $\dot{\epsilon}$=10^{-4} s^{-1}. 74
A.6 Normal–mode, σ_3 =200 MPa, $\dot{\epsilon}$=10^{-4} s^{-1}. 74
A.7 Normal–mode, σ_3 =400 MPa, $\dot{\epsilon}$=10^{-4} s^{-1}. 75
A.8 Normal–mode, σ_3 =400 MPa, $\dot{\epsilon}$=10^{-4} s^{-1}. 75
A.9 Normal–mode, σ_3 =800 MPa, $\dot{\epsilon}$=10^{-4} s^{-1}. 76
A.10 Normal–mode, σ_3 =800 MPa, $\dot{\epsilon}$=10^{-4} s^{-1}. 76

B.1 Normal–mode, unconfined, $\dot{\epsilon}$=10^{-2} s^{-1}. 78
B.2 Normal–mode, unconfined, $\dot{\epsilon}$=10^{-2} s^{-1}. 78
B.3 Normal–mode, σ_3=100 MPa, $\dot{\epsilon}$=10^{-2} s^{-1}. 79
B.4 Normal–mode, σ_3=100 MPa, $\dot{\epsilon}$=10^{-2} s^{-1}. 79

B.5 Normal–mode, σ_3=200 MPa, $\dot{\epsilon}$=10^{-2} s^{-1}. 80
B.6 Normal–mode, σ_3=200 MPa, $\dot{\epsilon}$=10^{-2} s^{-1}. 80
B.7 Normal–mode, σ_3=400 MPa, $\dot{\epsilon}$=10^{-2} s^{-1}. 81
B.8 Normal–mode, σ_3=400 MPa, $\dot{\epsilon}$=10^{-2} s^{-1}. 81

C.1 Axial–mode, unconfined, $\dot{\epsilon}$=10^{-4} s^{-1}. 84
C.2 Axial–mode, unconfined, $\dot{\epsilon}$=10^{-4} s^{-1}. 84
C.3 Axial–mode, σ_3 =100 MPa, $\dot{\epsilon}$=10^{-4} s^{-1}. 85
C.4 Axial–mode, σ_3 =100 MPa, $\dot{\epsilon}$=10^{-4} s^{-1}. 85
C.5 Axial–mode, σ_3 =200 MPa, $\dot{\epsilon}$=10^{-4} s^{-1}. 86
C.6 Axial–mode, σ_3 =200 MPa, $\dot{\epsilon}$=10^{-4} s^{-1}. 86
C.7 Axial–mode, σ_3 =400 MPa, $\dot{\epsilon}$=10^{-4} s^{-1}. 87
C.8 Axial–mode, σ_3 =400 MPa, $\dot{\epsilon}$=10^{-4} s^{-1}. 87

D.1 Axial–mode, unconfined, $\dot{\epsilon}$=10^{-2} s^{-1}. 90
D.2 Axial–mode, unconfined, $\dot{\epsilon}$=10^{-2} s^{-1}. 90
D.3 Axial–mode, unconfined, $\dot{\epsilon}$=10^{-2} s^{-1}. 91
D.4 Axial–mode, unconfined, $\dot{\epsilon}$=10^{-2} s^{-1}. 91
D.5 Axial–mode, σ_3 =100 MPa, $\dot{\epsilon}$=10^{-2} s^{-1}. 92
D.6 Axial–mode, σ_3 =100 MPa, $\dot{\epsilon}$=10^{-2} s^{-1}. 92
D.7 Axial–mode, σ_3 =200 MPa, $\dot{\epsilon}$=10^{-2} s^{-1}. 93
D.8 Axial–mode, σ_3 =200 MPa, $\dot{\epsilon}$=10^{-2} s^{-1}. 93
D.9 Axial–mode, σ_3 =400 MPa, $\dot{\epsilon}$=10^{-2} s^{-1}. 94
D.10 Axial–mode, σ_3 =400 MPa, $\dot{\epsilon}$=10^{-2} s^{-1}. 94

E.1 Unpoled hifire 424. Unconfined, $\dot{\epsilon}$=10^{-4} s^{-1}. 96
E.2 Unpoled hifire 424. Unconfined, $\dot{\epsilon}$=10^{-4} s^{-1}. 96
E.3 Unpoled hifire 424. Unconfined, $\dot{\epsilon}$=10^{-4} s^{-1}. 97
E.4 Unpoled hifire 424. Unconfined, $\dot{\epsilon}$=10^{-4} s^{-1}. 97
E.5 Unpoled hifire 424. Unconfined, $\dot{\epsilon}$=10^{-4} s^{-1}. 98
E.6 Unpoled hifire 424. Unconfined, $\dot{\epsilon}$=10^{-4} s^{-1}. 98

F.1 Unpoled hifire 541-1. Unconfined, $\dot{\epsilon}$=10^{-4} s^{-1}. 100
F.2 Unpoled hifire 541-1. Unconfined, $\dot{\epsilon}$=10^{-4} s^{-1}. 100
F.3 Unpoled hifire 541-1. Unconfined, $\dot{\epsilon}$=10^{-4} s^{-1}. 101
F.4 Unpoled hifire 541-1. Unconfined, $\dot{\epsilon}$=10^{-4} s^{-1}. 101
F.5 Unpoled hifire 541-1. Unconfined, $\dot{\epsilon}$=10^{-4} s^{-1}. 102

G.1 Poled hifire 541-1. Unconfined, $\dot{\epsilon}$=10^{-4} s^{-1}. 104
G.2 Poled hifire 541-1. Unconfined, $\dot{\epsilon}$=10^{-4} s^{-1}. 104

H.1 Unpoled hifire 453: hydrostatic compression. 106

H.2 Capacitance data for hydrostatic compression experiment CSD453-01, above. 106
H.3 Unpoled hifire 453: hydrostatic compression. 107
H.4 Capacitance data for hydrostatic compression experiment CSD453-05, above. 107
H.5 Unpoled hifire 453: $\sigma_1 - \sigma_3 = 50$ MPa. 108
H.6 Load path for experiment CSD453-03, above. 108
H.7 Capacitance data for experiment CSD453-03, above. 109
H.8 Unpoled hifire 453: $\sigma_1 - \sigma_3 = 50$ MPa. 110
H.9 Load path for experiment CSD453-06, above. 110
H.10 Capacitance data for experiment CSD453-06, above. 111
H.11 Unpoled hifire 453: $\sigma_1 - \sigma_3 = 100$ MPa. 112
H.12 Load path for experiment CSD453-02, above. 112
H.13 Capacitance data for experiment CSD453-02, above. 113
H.14 Unpoled hifire 453: $\sigma_1 - \sigma_3 = 100$ MPa. 114
H.15 Load path for experiment CSD453-07, above. 114
H.16 Capacitance data for experiment CSD453-07, above. 115
H.17 Unpoled hifire 453: $\sigma_1 - \sigma_3 = 150$ MPa. 116
H.18 Load path for experiment CSD453-04, above. 116
H.19 Capacitance data for experiment CSD453-04, above. 117
H.20 Unpoled hifire 453: $\sigma_1 - \sigma_3 = 150$ MPa. 118
H.21 Load path for experiment CSD453-08, above. 118
H.22 Capacitance data for experiment CSD453-08, above. 119

List of Tables

3.1 Normal mode, uniaxial and triaxial compression experiments on poled hifire 453 ceramic. 16
3.2 Axial mode, uniaxial and triaxial compression experiments on poled hifire 453 ceramic. 17

4.1 Uniaxial compression experiments on unpoled, hifire 453 ceramic. 54
4.2 Uniaxial compression experiments on unpoled, hifire 541-1 ceramic. 54
4.3 Uniaxial compression experiments on unpoled, hifire 424 ceramic. 55
4.4 Normal-mode, uniaxial compression experiments on poled, hifire 541-1 ceramic. 55

Chapter 1

Introduction

$PbZrO_3$ and $PbTiO_3$ form a complete solid-solution series (lead-zirconate-titanate, or PZT) of great technological importance. It is used in various Zr:Ti ratios and with numerous dopants to manufacture a wide range of electronic and electromechanical devices(*e.g.*, Newnham [1989]; Haun *et al.* [1989]). One of these modifications, $Pb_{0.99}Nb_{0.02}(Zr_{0.95},Ti_{0.05})_{0.98}O_3$ (referred to hereafter as PZT 95/5-2Nb), is used in shock-actuated power supplies of the sort used in neutron generators [Lysne and Percival, 1975; Bauer *et al.*, 1976].

At room temperature, PZT 95/5-2Nb has a rhombohedrally distorted perovskite structure (F_{R1}), and is ferroelectric [Fritz and Keck, 1978] (Figure 1.1); that is, a crystal (as well as subdomains within a single crystal) exhibits a spontaneous polarization in any one of eight crystallographically-equivalent directions. Thus, single crystals or polycrystals can be polarized ("poled") in an electric field. Domains with dipoles more closely aligned with the electric field grow at the expense of domains whose dipoles are less favorably aligned. When the electric field is relaxed, some remnant polarization persists and a bound charge is stored. At a hydrostatic pressure of about 300 MPa, the poled material undergoes a weak, displacive, first-order phase transformation to an orthorhombic, antiferroelectric (macroscopically electrically neutral) structure (A_O) [Belincourt *et al.*, 1964; Fritz and Keck, 1978; Fritz, 1978]. The structural change is accompanied by a volume decrease of about 0.7%. When the transformation occurs, the bound charge is released. Under shock-wave conditions this takes place rapidly and very high currents and voltages can be obtained.

As designs and testing become more expensive, it becomes increasingly cost-effective to use finite-element methods to model and optimize neutron generator power supply designs prior to construction and testing of prototypes. In order to do this, constitutive models must be available for the

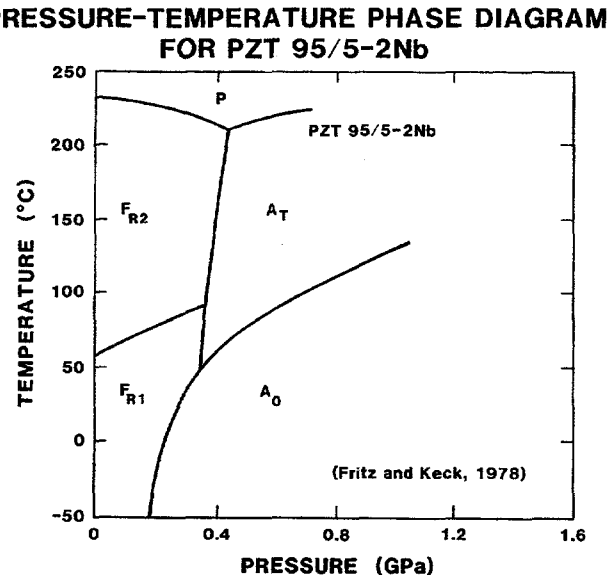

Figure 1.1: Pressure-temperature phase diagram for PZT 95/5-2Nb [Fritz and Keck, 1978]. Other known phases are: a high temperature, ferroelectric rhomobohedral phase (F_{R2}), an antiferroelectric, tetragonal phase (A_T), and a paraelectric, cubic polymorph (P).

various materials used in the component, including one for the electromechanical behavior of poled PZT 95/5-2Nb during the polymorphic transformation (*e.g.*, Montgomery [1986]; Horie *et al.* [in preparation]).

As part of an ongoing effort to develop constitutive models for the electromechanical behavior of PZT 95/5-2Nb during the ferroelectric-antiferroelectric (FE-AFE) polymorphic phase transformation, we have performed an extensive series of quasistatic, hydrostatic and triaxial compression experiments on both poled and unpoled PZT 95/5-2Nb specimens from several sintering batches, also referred to as "hifires." Our efforts have focused exclusively on the effects of nonhydrostatic stresses on the FE-AFE transformation. In those experiments, deviatoric stresses were small, causing only elastic strains. We have summarized results of these investigations elsewhere [Zeuch *et al.*, 1992a; 1992b; 1994; 1995; in preparation], and will not review them here.

In this report we focus on a different problem related to constitutive modeling of PZT 95/5-2Nb ceramic. The conditions under which mechanical failure of the ceramic, and, hence, the power supply, might occur are subjects of both interest and concern. Under shock loading, the ceramic is

subjected to large, compressive, mean and deviatoric stresses. Like brittle rocks and minerals, ceramics fall into the category of *pressure-sensitive, dilatant* materials. That is, their compressive fracture strengths and failure mechanisms are dependent upon the ambient pressure or mean stress [Paterson, 1978; Meredith, 1990; Hallam and Ashby, 1990]. Compressive strengths are similarly strain rate dependent [Paterson, 1978]. Thus, the objective of this investigation has been to quantify the compressive strength of PZT 95/5- 2Nb ceramic as functions of pressure and strain rate, for extrapolation to shock wave conditions.

Thirty-six triaxial compression experiments were performed at room temperature on ceramic specimens from a single sintering batch ("hifire"). Confining pressures ranged from ambient (unconfined) to 800 MPa, and nominal strain rates were 10^{-2} or $10^{-4}s^{-1}$. Although it was not expected to profoundly influence compressive strength, all specimens were poled in order to maximize similarity to the ceramic actually used in power supplies. Approximately half of the experiments were conducted on specimens poled transverse to the axis of deviatoric loading (the so-called "normal mode") and the remainder were conducted on specimens poled parallel to the axis of deviatoric loading ("axial mode").

At an axial strain rate, $\dot{\epsilon}$, of $10^{-4}s^{-1}$, compressive strength under unconfined conditions is approximately 558 MPa. Strength increases to approximately 940 MPa at a confining pressure, σ_3, of 400 MPa. Interestingly, the two experiments conducted at a confining pressure of 800 MPa exhibited strengths comparable to the specimens tested at σ_3=400 MPa, suggesting that some sort of strength limit was reached between these two pressures at $\dot{\epsilon}$ of $10^{-4}s^{-1}$: this issue should be investigated further. A similar trend was observed at a strain rate of $10^{-2}s^{-1}$. Under unconfined conditions, compressive strength is approximately 663 MPa, increasing to 1044 MPa at σ_3=400 MPa. The usual transition in failure modes with increasing confining pressure–from axial splitting to discrete shear failure to distributed microcracking–was observed [Paterson, 1978]. As expected, the relationship between poling direction and axis of compression had no clearly detectable influence on strength.

Under unconfined conditions, the two-order-of-magnitude increase in strain rate results in a 19% increase in strength; at 400 MPa, the same increase leads to an 11% increase in compressive strength. It appears that the strength of PZT 95/5-2Nb may increase somewhat more strongly with strain rate than some rocks. Paterson [1978; p.32] summarizes results of several investigations at comparable strain rates that found strengths of various rock types to increase by about 10% for a 10^3-fold increase in strain rate; we see 10-20% increases with only a 10^2-fold increase in strain rate. Nevertheless, our results are generally consistent with those for rocks.

Interestingly, the $F_{R1} \rightarrow A_O$ transformation can be triggered in simple uniaxial compression [Fritz, 1979; Zeuch *et al.*, 1997; in preparation]. This results in some highly unusual strain responses at confining pressures below that for onset of the transformation, 250-300 MPa. There are distinct differences between the strain responses of specimens compressed in the normal and axial modes, which are, in turn, different from the strain response of unpoled ceramic. As we will discuss at length below, these differences are due, in part, to differences in the amounts of stress-induced dipole rotation that can occur, as well as to stress-induced transformation effects. As a consequence of the fact that the transformation is triggered by axial compression, the pure FE phase does not have a failure strength. When failure occurs in all of our experiments, the ceramic always consists, at least partly, of the AFE phase.

Although this report is principally concerned with the failure properties of PZT 95/5-2Nb ceramic, we will dwell at some length on the associated transformation effects that are incidentally observed in the experiments. We have shown that much can be learned about the nature of the transformation even from uniaxial compression experiments [Zeuch *et al.*, 1997; in preparation; *see also:* Fritz, 1979]. Much can also be learned about stress-induced dipole rotation by examining differences amongst normal– and axial–mode experiments, and experiments on unpoled ceramic. While many of the results that we report here are consistent with our earlier observations and conclusions about the transformation and the circumstances under which it occurs [Zeuch *et al.*, 1997; in preparation], there are differences that will be discussed.

Finally, we have performed a series of hydrostatic, uniaxial and triaxial compression experiments on unpoled specimens from the same hifire from which we fabricated the foregoing poled specimens. Batch-to-batch variations in electromechanical properties of PZT 95/5-2Nb are well-documented [Dungan and Storz, 1985; Zeuch *et al.*, 1992a,b], despite the tight quality control measures that appear to be applied to production of WR-qualified PZT 95/5-2Nb (*e.g.*, Keck [1990]). Insofar as possible, we wished to ensure that the properties of the particular hifire that we report on here are generally similar to those that we have investigated previously [Zeuch *et al.*, 1992a,b; 1994; 1995; 1997; in preparation]. (We are also attempting to create a database in order to define the range of "typical" properties of accepted voltage bar ceramic.) Thus, on unpoled ceramic we have conducted: (1) hydrostatic compression experiments to determine the transformation pressure of the unpoled material; (2) constant- stress-difference (CSD) experiments to measure the effects of nonhydrostatic stress on the transformation; and (3) uniaxial compression experiments to determine the failure strength, Young's

modulus and Poisson's ratio. As with the experiments on poled ceramic, results from these experiments confirm the general similarity of this hifire to those that we have investigated previously, although there are some significant differences that should be investigated more fully. In the interest of completeness, we report these results here, too.

In the following section, we discuss our experimental materials and techniques. We will then briefly present the results of our characterization experiments on unpoled ceramic. A detailed presentation of the results of our experiments on poled specimens will follow. We will conclude with a discussion of our results and their implications, and recommendations for future directions.

THIS PAGE INTENTIONALLY LEFT BLANK

Chapter 2

Experimental Material and Techniques

2.1 Experimental Materials

The PZT 95/5-2Nb ceramic specimens used in this investigation came from hifire 453, which was prepared from mixed oxide powders in Sandia National Laboratories' Ceramic Shop when the Shop was QER'd (Qualification Evaluation Release) to produce WR (war-reserve) quality hifires for use in assembling MC (military characteristic) components [J. D. Keck, pers. comm., 1998]. The ceramic was qualified on December 22, 1981 for use as voltage bar ceramic in the MC3037 neutron generator subassembly for the W79.

Testing yielded an average depoling pressure of 38.6 kpsi (266 MPa), an average depoling charge of 30.1 μC cm^{-2}, and an average density of 7.30 g cm^{-3}. Referred to a theoretical density of 8.00 g cm^{-3}, the average porosity of hifire 453 is therefore about 9%. The pore former used in hifire 453 was Lucite microspheres 50-100 microns in diameter, added in the quantity of 6.5 g per kilogram of PZT powder. Nomarski microscopy performed by R. E. Setchell (Dept. 1152) reveals a distinctly inhomogeneous Lucite-formed pore distribution from area to area (Figure 2.1)

Beyond this, we have no detailed information on the microstructure of the hifire, *i.e.*, grain, fine pore and domain sizes, shapes and distributions. However, owing to the tight controls that are typically applied to manufacture of WR-qualified PZT 95/5-2Nb (*e.g.*, Keck [1990]), we are reasonably confident that hifire 453 is similar in grain size, domain size, and fine pore size distribution to other mixed oxide hifires that have been examined by us [Zeuch *et al.*, 1992a,b] and by others [Chhabildas *et al.*, 1986; Storz and Dungan, 1986]. (By "fine" pores we mean those small pores that normally remain after sintering, and which were not caused by the added Lucite.) That is,

grain size is *probably* in the range of 5-10 microns, and the fine pore size after sintering is likely to be about 1-10 microns. Domain size is probably about 1 micron.

We will be comparing some of the results obtained for hifire 453 with results of similar experiments performed earlier on specimens from hifires 541-1 and 424. Apart from mentioning here that the former is qualified voltage bar material and the latter qualified current stack material, we note only that additional details about these two hifires are available elsewhere [Keck, 1990; Zeuch *et al.*, 1992a,b].

2.2 Experimental Techniques

In all experiments, specimens were right rectangular prisms measuring 1.080 cm $\times$ 1.080 cm $\times$ 2.540 cm, with the two opposing square faces ground flat and parallel within 0.0003 cm (Figure 2.2). Depending upon the particular type of experiment to be performed, silver electrodes were evaporated onto various pairs of opposing faces.

For all unpoled specimens, two opposing rectangular prism faces were electroded to permit capacitance measurements to be performed. Specimens that were to be poled for normal mode deformation were similarly electroded, to permit poling transverse to the long direction. Specimens to be deformed in the axial mode were electroded on the two square faces to permit poling parallel to the long direction.

Transversely poled specimens were "hot-poled" in electric fields corresponding to 50 V per 0.003 cm (0.001 in) of thickness. Specimens were heated in oil to 105 °C, and the electric field applied. The temperature was then lowered to 70 °C over a period of 5 minutes, whereupon the electric field was removed. Cooling to room temperature then continued. Specimens poled parallel to the specimens' long axis were treated similarly, except that they were poled in an electric field of 30 V per 0.003 cm (0.001 in). Though we had originally planned to pole all specimens in the same electric field, this proved not to be possible with the equipment at hand. Thus, the specimens most probably do not have identical remnant polarizations and preferred crystallographic orientations about their respective poling axes. As we discuss in a later section, this may be important when comparing the stress-induced transformation of ceramic deformed in the normal and axial modes. Note that the earlier poled specimens from other hifires that we have tested in the normal mode in constant-stress-difference experiments [Zeuch *et al.*, 1995; in preparation] were poled in the same strength of field used here to prepare normal-mode specimens.

Strains were measured using standard, foil-backed, resistance strain gauges

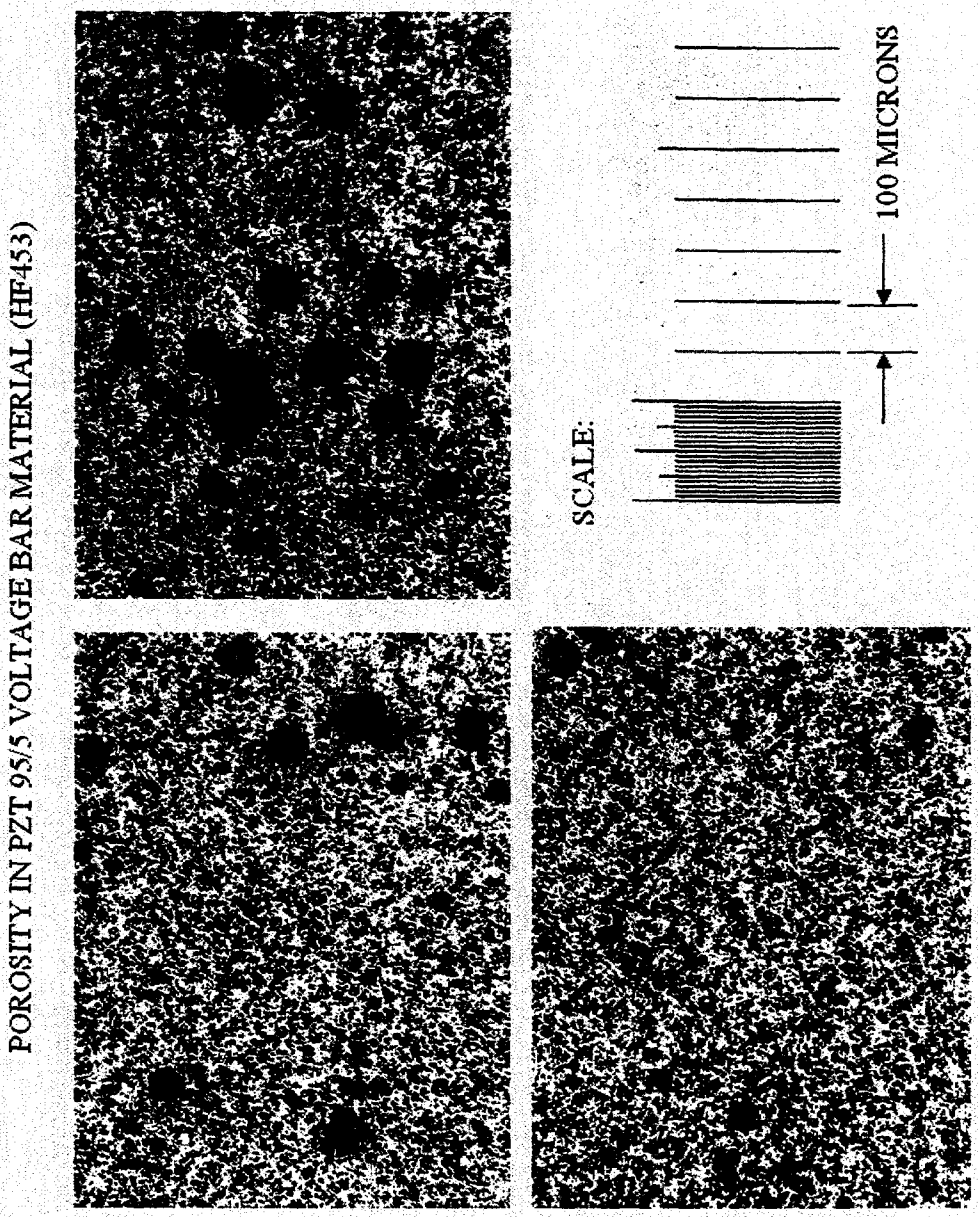

Figure 2.1: Distribution of large pores formed by added Lucite microspheres (black circles approximately 100 microns in diameter). Note differing distributions from micrograph to micrograph. Figure courtesy of R. E. Setchell, Dept. 1152.

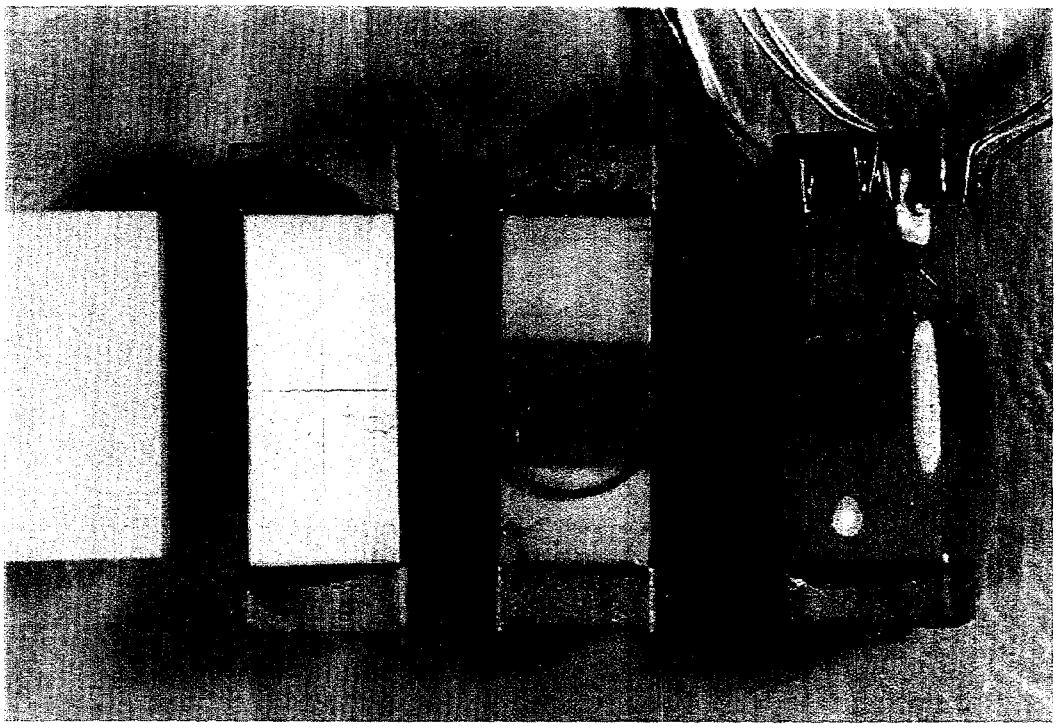

Figure 2.2: From left to right, stages in specimen assembly. Unassembled specimen (left) is 2.54 cm long.

bonded to the rectangular prism faces. In the discussion that follows, axial strains are those parallel to the long sample dimension, and lateral (or transverse) strains are those measured on the prism faces in directions perpendicular to the long direction. Again, depending upon the particular purpose to which a specimen was to be put, the number of strain gauges varied. This is because our pressure vessel (discussed below) is equipped with only twelve electrical feedthroughs: the number of possible strain gauges is sometimes reduced to allow other types of measurements. Because of their known mechanical anisotropy [Zeuch *et al.*, 1995], all poled specimens were instrumented with three pairs of orthogonal gauges. Owing to the number of strains that had to be measured, capacitance measurements were not performed on poled specimens.

For unpoled specimens, one axial gauge was sacrificed so that capacitance measurements could be performed as well. Both specimens thus had some measure of redundancy of strain measurements, and, where appropriate, redundant (*i.e.*, parallel) gauges were summed and averaged before calculating axial, lateral and volumetric strains.

Slightly outsized tungsten carbide endcaps were glued to the ends of the samples. Because of the number of strains that had to be measured on poled specimens, we lacked sufficient feedthroughs to also measure discharge voltage (or capacitance) during the experiments (*e.g.*, Zeuch *et al.*, 1995]. In this report, electrodes were simply shorted together with a connecting wire. Specimen assembly was completed with a coating of urethane, which prevented intrusion of the confining fluid into the ceramic during hydrostatic and triaxial compression experiments.

All experiments were done at room temperature in the same standard liquid-medium triaxial testing apparatus used by us previously [Zeuch *et al.*, 1992a; 1992b; 1995]. The apparatus (Figure 2.3) consists of a 1000 MPa pressure vessel and 1.78 MN hydraulic actuator enclosed in a stiff reaction frame that allows transfer of force from the actuator to the test specimen *via* the moving piston. The pressure vessel end closure is fitted with twelve high-pressure electrical feedthroughs which make the strain gauge and capacitance measurement on the specimens possible. In hydrostatic compression experiments, the piston is locked in place and only the confining liquid, ISOPAR^{TM}, is pressurized. In nonhydrostatic experiments, deviatoric stresses are applied axially using the independently controlled actuator and piston. In uniaxial compression experiments, of course, the pressure vessel is not needed at all, and simply serves as additional protection from the explosive failure of the ceramic specimens.

In the foregoing experimental configuration, $\sigma_1 > \sigma_2 = \sigma_3$, where σ_1, σ_2 and σ_3 are the greatest, intermediate and least principal stresses, compressive stresses reckoned positive. σ_1 is applied parallel to the long dimension of the test specimens using the movable piston; $\sigma_2 = \sigma_3 =$ the fluid (or *confining*) pressure. In what follows, we will frequently refer to the *stress difference*, $\sigma_1 - \sigma_3$. The stress difference is twice the maximum resolved shear stress on the specimen, $\tau = \left(\frac{\sigma_1 - \sigma_3}{2}\right)$.

Load was measured using an external load cell with a maximum rating of 0.445 MN, and fluid pressure was measured with a pressure cell. Calibration against known standards indicates that the load cell is accurate to $\pm$480 N. The pressure cell has a resolution of $\pm$0.008 MPa over the pressure range 0 to 448 MPa. Capacitance measurements were performed using a Hewlett-Packard HP4192A LF Impedance Analyzer operating at 1 kHz. The impedance analyzer is equipped with an analog output.

The signals from the impedance analyzer, strain gauges, and load and pressure cells, were transmitted to a Keithly 500 data acquisition system and written to the hard disk on an IBM-compatible personal computer. Preliminary data reduction was accomplished during acquisition using the program DATAVG [Hardy, 1993; 1997], and subsequent data analysis was performed

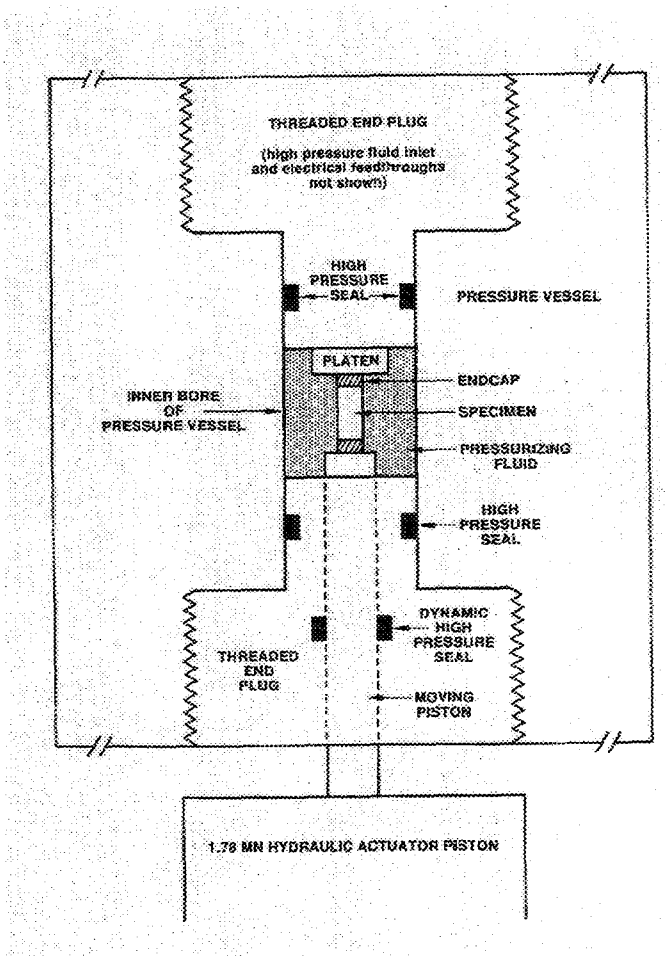

Figure 2.3: Schematic illustration of the apparatus used in this investigation. The stiff reaction frame is not shown.

using PSIPLOT,^{TM} a commercially-available data processing and plotting package.

Three different types of experiments were conducted. The preponderance of those discussed in this report are standard, triaxial compression experiments on poled specimens, deformed at constant strain rate. In these experiments, the specimen is first pressurized to the appropriate confining pressure, 0.1 (unconfined), 100, 200, 400 or (in two experiments) 800 MPa. The hydraulic actuator is then used to slowly advance the movable piston into contact with the test specimen; contact is determined by a small rise in load above that caused jointly by piston-seal friction and reaction to the hydrostatic pressure. At this point, the piston is backed well off of the speci-

men, then brought just into contact again and held. This yields a full friction hysteresis loop (negligible under unconfined conditions, and different at each of the four elevated pressures) that would later be used during data reduction to correct the load record for piston-seal friction. The piston is then advanced into the pressure vessel at a constant displacement rate, corresponding to a nominal axial strain rate, $\dot{\epsilon}_a$, of 10^{-2} or 10^{-4} s^{-1}. Deformation continued until failure.

Eighteen each of such experiments were performed on specimens poled parallel and perpendicular to the axis of compression; of these, half were performed at each of the two strain rates.

As noted earlier, we also performed ten additional characterization experiments on unpoled specimens from hifire 453, for comparison with earlier results on three other hifires that we have investigated: 424, 541-1 and 435 [Zeuch *et al.*, 1992a,b]. These experiments consisted of hydrostatic compression and constant-stress-difference (CSD) experiments, as well as two uniaxial compression tests. We discussed uniaxial compression experiments in the previous paragraph, and hydrostatic compression tests should require no explanation. We have described our CSD experiments in detail elsewhere [Zeuch *et al.*, 1992a,b; 1995], but briefly review them again here. The interested reader is referred to our earlier reports for detailed discussion.

In CSD tests, the samples are first pressurized hydrostatically to 69 MPa. This initial pressurization is performed to minimize any possibility of microcracking. Then an additional axial load is superimposed, using the hydraulically-actuated piston, to increase the stress difference, σ_1-σ_3, to 50, 100 or 150 MPa. These stress differences are far below the uniaxial (*i.e.*, unconfined) compressive strength of approximately 650 MPa that we have measured for this same material (see below). The axial stress, σ_1, and fluid pressure, σ_3, are then increased simultaneously under microprocessor control so that the stress difference, and hence the maximum resolved shear stress, $(\frac{\sigma_1-\sigma_3}{2})$, remained constant through the transformation. In both hydrostatic compression and CSD experiments, the confining pressure, σ_3, was first increased, and then decreased at the same constant rate, 0.69 MPa sec^{-1}. In our previous investigations, we have shown that the loading conditions discussed in this report leave the specimens completely intact, macroscopically and microscopically entirely free of any cracks, chips, pore collapse or other evidence of damage [Zeuch *et al.*, 1992a,b; 1995]. We have seen no evidence in this study that contradicts our previous conclusion that no damage occurs in our hydrostatic compression and CSD experiments on 453 ceramic.

Because of the continually changing mean stress, it is not possible to correct for piston-seal friction in the CSD tests. However, we have measured friction of the moving piston as a function of confining pressure [Zeuch *et al.*,

1994] and shown that its effect on axial stress measurements is about 12 MPa in the range of the phase transformation (about 300 MPa) when referred to the sample's cross-sectional area. It must be remembered that during our constant-stress-difference experiments, the loading piston is always moving *into* the vessel, so the measured loads and, hence, axial stresses (σ_1) will always be *greater* than those acting on the samples. The result is that the mean stresses that we calculate for our constant-stress-difference experiments are even *further* depressed below the hydrostatic experiments than we show later.

Chapter 3

Experimental Results: Triaxial Compression Experiments on Poled Ceramic

3.1 A Few Preliminary Remarks on Transformation Effects and Stress-Strain Data

Tables 3.1 and 3.2 summarize the test conditions and important results for the triaxial compression experiments on poled specimens deformed in the normal and axial modes, respectively.

Plots of the stress-strain data from all successful experiments are presented in Appendices A-D. Representative plots of selected normal– and axial– mode experiments performed at a strain rate of 10^{-4} s^{-1} are shown in Figures 3.1-3.5 and 3.6-3.9, respectively. Examination of the two sets of figures, and the data summarized in Tables 3.1 and 3.2, reveals both expected and unexpected results. As expected, strength and ductility both increase with confining pressure at constant strain rate. Equally unsurprisingly, strength increases with applied strain rate at constant confining pressure.

Unexpected, however, are the peculiar forms of some of the plots of stress *versus* axial, lateral and volume strain. All of the specimens deformed at or below σ_3 =200 MPa exhibit surprising nonlinearity and/or sudden offsets in their strain responses at stress differences well below ultimate failure strength. Notice, for example, the sudden, compressive offsets in all strains at a stress difference of about 100 MPa in those experiments performed at σ_3 =200 (Figures 3.3 and 3.8). Notice also that the lateral strains completely reverse *twice* prior to failure, in experiments performed at or below σ_3=100 MPa (Figures 3.10 and 3.11; also Figures 3.1, 3.2, 3.6 and 3.7). This is re-

Experiment ID	$\dot{\epsilon}$ (s^{-1})	σ_3 (MPa)	σ_f (MPa)	ϵ_{a_f} (%)
453-09	10^{-4}	U (0.1)	539	0.8
453-10	10^{-4}	U (0.1)	559	0.8
453-07	10^{-4}	100	847	1.5
453-08	10^{-4}	100	845	1.4
453-01	10^{-4}	200	925	1.7
453-06	10^{-4}	200	894	1.6
453-02	10^{-4}	400	968	2.3
453-05	10^{-4}	400	956	2.2
453-03	10^{-4}	800	953	1.7
453-04	10^{-4}	800	895	1.7
453-11	10^{-2}	U (0.1)	672	0.9
453-12	10^{-2}	U (0.1)	679	1.0
453-13	10^{-2}	100	937	1.5
453-14	10^{-2}	100	911	1.5
453-15	10^{-2}	200	947	1.8
453-16	10^{-2}	200	992	1.7
453-17	10^{-2}	400	1021	2.2
453-18	10^{-2}	400	1063	2.2

Table 3.1: Normal mode, uniaxial ("U") and triaxial compression experiments on poled hifire 453 ceramic. σ_f and ϵ_{a_f} are the stress difference and axial strain at failure, respectively.

markable behavior for a brittle ceramic, especially in uniaxial compression. Additionally, volumetric strains are unusually large and compressive right up until failure. These oddities require a few explanatory remarks before proceeding to a discussion of the effects of confining pressure and strain rate on strength and ductility.

This particular voltage bar ceramic has a porosity of about 9%. Stable pore collapse accompanied by sudden, compressive axial and volumetric strains, is often observed during hydrostatic and triaxial compression of porous rock [Wong *et al.*, 1992; their Figs. 2 and 6]. Therefore, pore collapse *could* conceivably explain our observations at elevated confining pressures; however, it almost certainly cannot account for those under unconfined conditions. In the latter instance, we are uniaxially compressing a fairly strong, obviously brittle ceramic, and the catastrophic failure of our test specimens (see below) confirms that we are in the brittle deformation regime. Under unconfined conditions, it is far more likely that the pores will act as stress concentrators, not collapsing isotropically but rather promoting axial crack

Experiment ID	$\dot{\epsilon}$ (s^{-1})	σ_3 (MPa)	σ_f (MPa)	ϵ_{a_f} (%)
453-20	10^{-4}	U (0.1)	577	1.0
453-19	10^{-4}	U (0.1)	411	0.8
453-21	10^{-4}	100	857	1.5
453-22	10^{-4}	100	857	1.5
453-23	10^{-4}	200	922	1.8
453-24	10^{-4}	200	893	1.8
453-25	10^{-4}	400	879	2.1
453-26	10^{-4}	400	957	2.3
453-27	10^{-2}	U (0.1)	184	0.4
453-31	10^{-2}	U (0.1)	N/D	N/D
453-35	10^{-2}	U (0.1)	644	1.0
453-36	10^{-2}	U (0.1)	655	1.0
453-28	10^{-2}	100	928	1.6
453-32	10^{-2}	100	945	1.6
453-29	10^{-2}	200	1010	1.9
453-33	10^{-2}	200	995	1.9
453-30	10^{-2}	400	1038	2.3
453-34	10^{-2}	400	1080	2.3

Table 3.2: Axial mode, uniaxial ("U") and triaxial compression experiments on poled hifire 453 ceramic. σ_f and ϵ_{a_f} are the stress difference and axial strain at failure, respectively. N/D: not determined.

nucleation. This in turn would result in anomalously large, tensile, lateral strains and rapid volume increases (dilatancy) preceding or coincident with failure (*e.g.*, Paterson [1978]). Under uniaxial conditions, we observe these phenomena only after the lateral strains have reversed twice (Figures 3.10 and 3.11). These observations alone would lead us to conclude that pore collapse is not the cause of our observed, low-stress nonlinearities.

However, we have also performed optical and scanning electron microscopy on unpoled specimens from other PZT 95/5-2Nb ceramic hifires. Those specimens have been pressurized under both hydrostatic and constant-stress-difference conditions to much higher mean stresses without evidence of pore collapse [Zeuch *et al.*, 1992b; their Figure 4]. That earlier evidence further supports our present conclusion that pore collapse is not responsible for these peculiar observations. Fortunately, an alternative explanation is readily at hand.

As noted earlier, both we [Zeuch *et al.*, 1997; in preparation] and Fritz

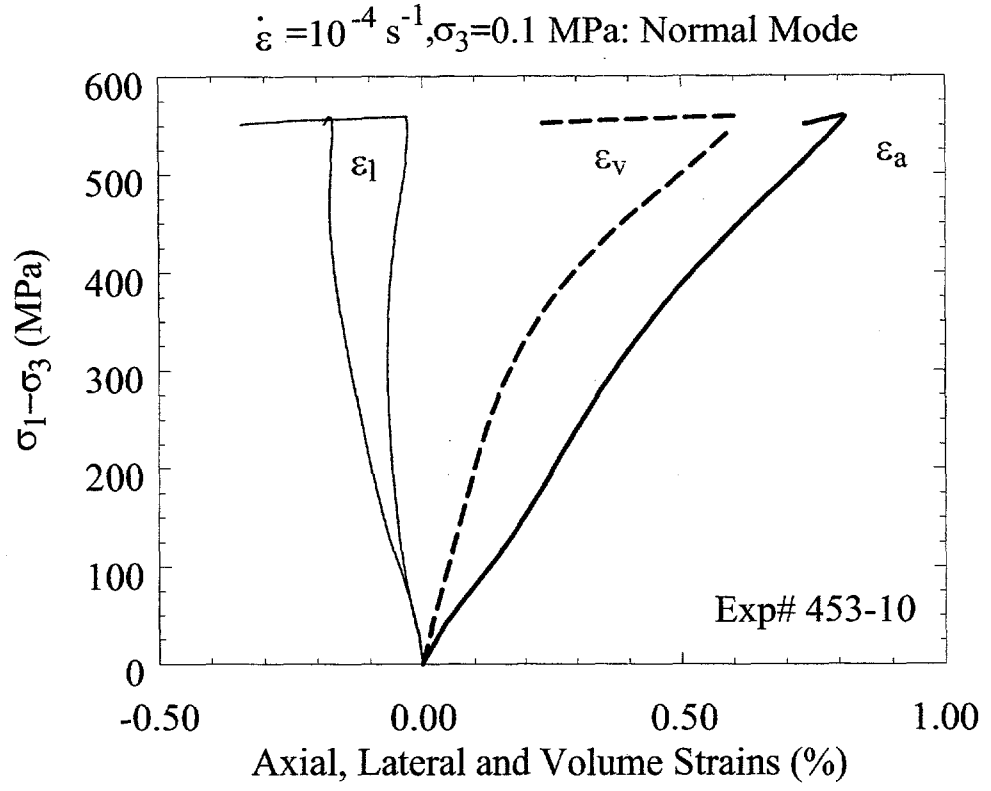

Figure 3.1: Normal-mode uniaxial compression experiment at $\dot{\epsilon}$=10^{-4}s^{-1}. ϵ_a, ϵ_l and ϵ_v are the axial, lateral and volume strains, respectively.

[1979] have shown that the $F_{R1} \rightarrow A_O$ transformation can be triggered during uniaxial compression of *unpoled* ceramic. The odd, extremely nonlinear stress-strain plots that we observe at confining pressures at and below 200 MPa (Figures 3.1-3.3 and 3.6-3.8) clearly indicate that the transformation is occurring during uniaxial and triaxial compression of *poled* ceramic, as well. The occurrence of a phase transformation accompanied by a volume decrease readily explains the (1) lateral strain reversals, (2) sudden strain offsets and (3) large, compressive volume strains prior to failure that are observed in the lower-pressure experiments [Zeuch *et al.*, in preparation; Fritz, 1979]. Simply put, compressive strains associated with the transformation overwhelm dilational strains associated with axial compression until close to the point of failure.

On the other hand, we can also explain the *absence* of peculiarities in the

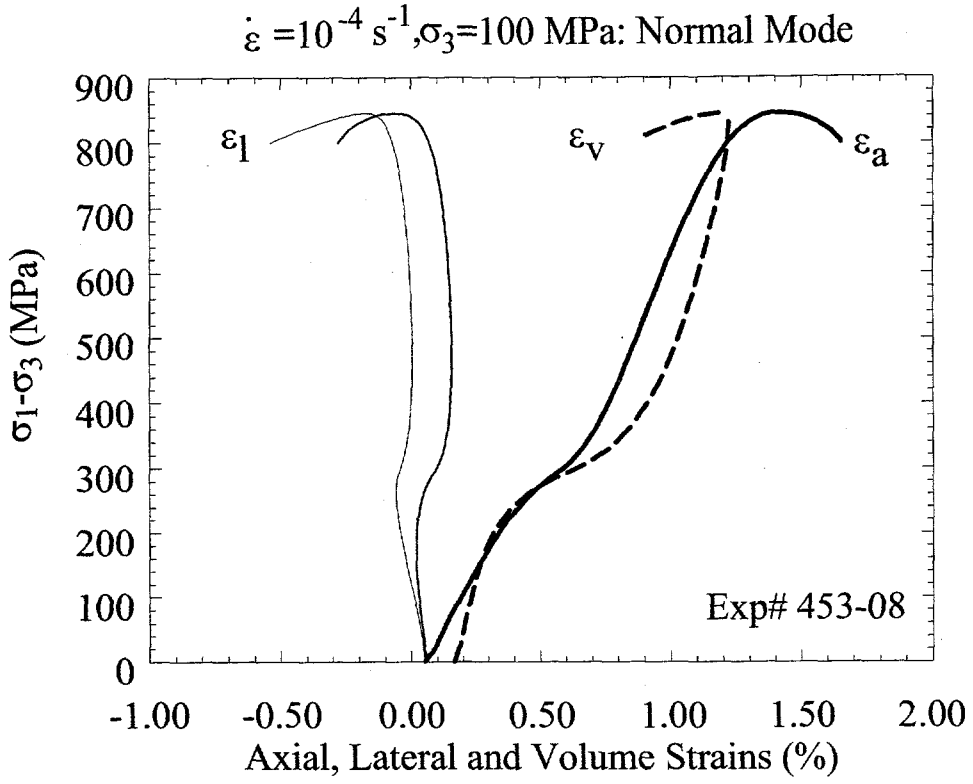

Figure 3.2: Normal-mode, triaxial compression experiment at $\dot{\epsilon}$=10^{-4}s^{-1} and σ_3=100 MPa. ϵ_a, ϵ_l and ϵ_v are the axial, lateral and volume strains, respectively.

strain response of specimens tested at 400 and 800 MPa. The hydrostatic pressurization stages of deformation experiments conducted at 400 and 800 MPa indicate that the transformation of poled 453 ceramic begins at about 225-250 MPa (Figure 3.12) under hydrostatic conditions; thus experiments at the higher confining pressures (Figures 3.4, 3.5 and 3.9) should begin deviatoric loading entirely in the AFE stability field, and, as observed, don't exhibit any of the oddities seen at the lower pressures. This constitutes another piece of evidence that the nonlinearities in many of our stress-strain plots are the result of triggering the transformation under deviatoric loading.

The volume strain responses shown in Figures 3.1 and 3.6 (and other plots, as well) further indicate that some of the low-stress nonlinearities in the axial and lateral strain records can also be attributed to dipole rotation. Note that the volume strain responses are essentially linear up until a stress difference

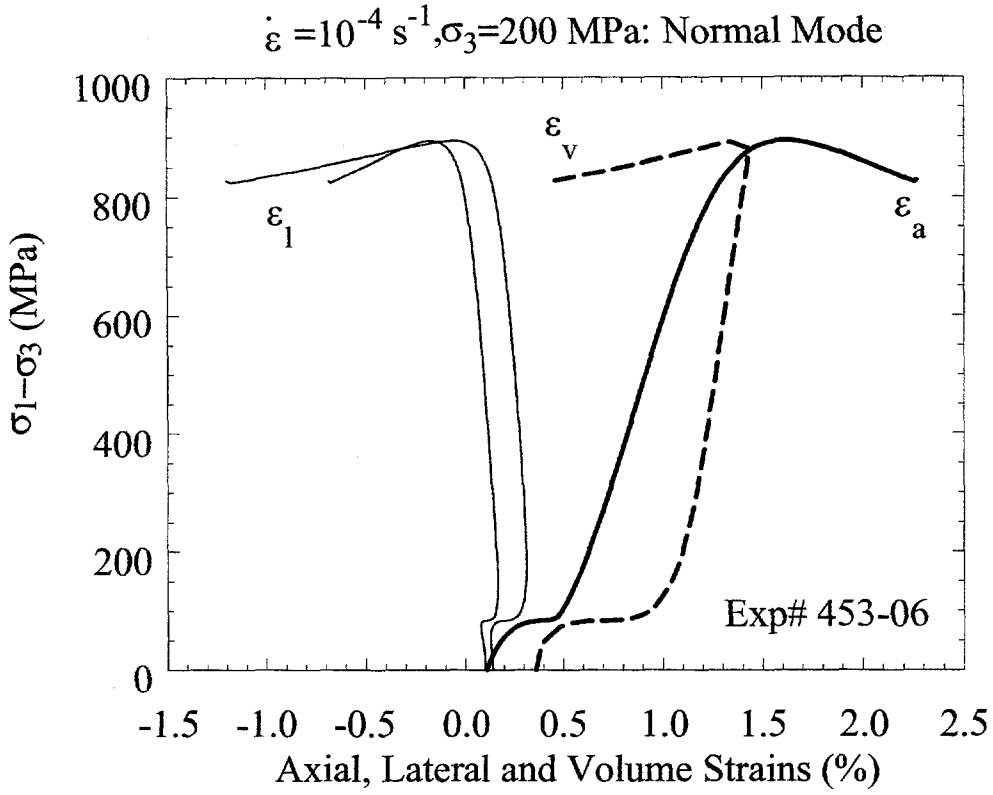

Figure 3.3: Normal-mode, triaxial compression experiment at $\dot{\epsilon}$=10^{-4}s^{-1} and σ_3=200 MPa. ϵ_a, ϵ_l and ϵ_v are the axial, lateral and volume strains, respectively.

of about 225-250 MPa, whereas the axial and lateral strain responses become quite nonlinear at much lower stresses, 50-75 MPa. Although we have not performed the careful, elastic analysis of Zeuch *et al.* [in preparation], we think that the low stress, linear portion of the volume strain plot is simply the normal volumetric response to uniaxial compression that is associated with Poisson's ratio. The departure of the volume strain response from linearity at 225-250 MPa probably represents onset of the transformation, though steadily increasing deviatoric stresses are required to drive the transformation forward [Zeuch *et al.*, in preparation].

If this is true, then based on the observations and reasoning of Zeuch *et al.* [in preparation], we further conclude that the nonlinearities in the axial and lateral strain responses that occur at low deviatoric stresses can be attributed to rotation of dipoles away from the maximum compressive stress [Fritz, 1978;

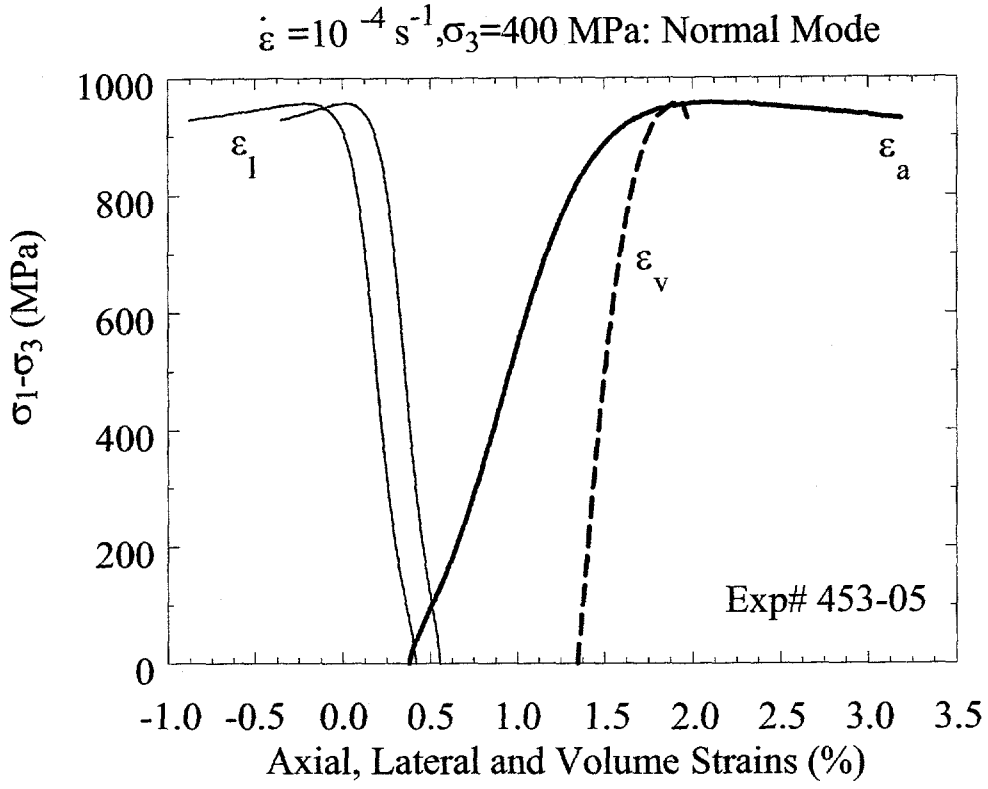

Figure 3.4: Normal-mode, triaxial compression experiment at $\dot{\epsilon}$=10^{-4}s^{-1} and σ_3=400 MPa. ϵ_a, ϵ_l and ϵ_v are the axial, lateral and volume strains, respectively.

1979]. Because the unit cell of the distorted perovskite cube is longer parallel to the dipole, this would be consistent with the observed, exaggerated axial compression and lateral rarefactions [Fritz, 1978; 1979]. Dipole rotation is an isovolumetric process, so the plot of stress *versus* volume strain would not display any sudden nonlinearities, as observed. We will also show later that differences in the behaviors of specimens deformed in the normal and axial modes provide added insight into the occurrence of dipole rotation during deformation.

We acknowledge that the foregoing observations and arguments do not constitute rigorous proof that deviatoric loading is triggering both the phase transformation and dipole switching in our experiments. We have only shown that our data are consistent with occurrence of these processes. Nor have we made any careful attempt to separate and quantify the contributions of

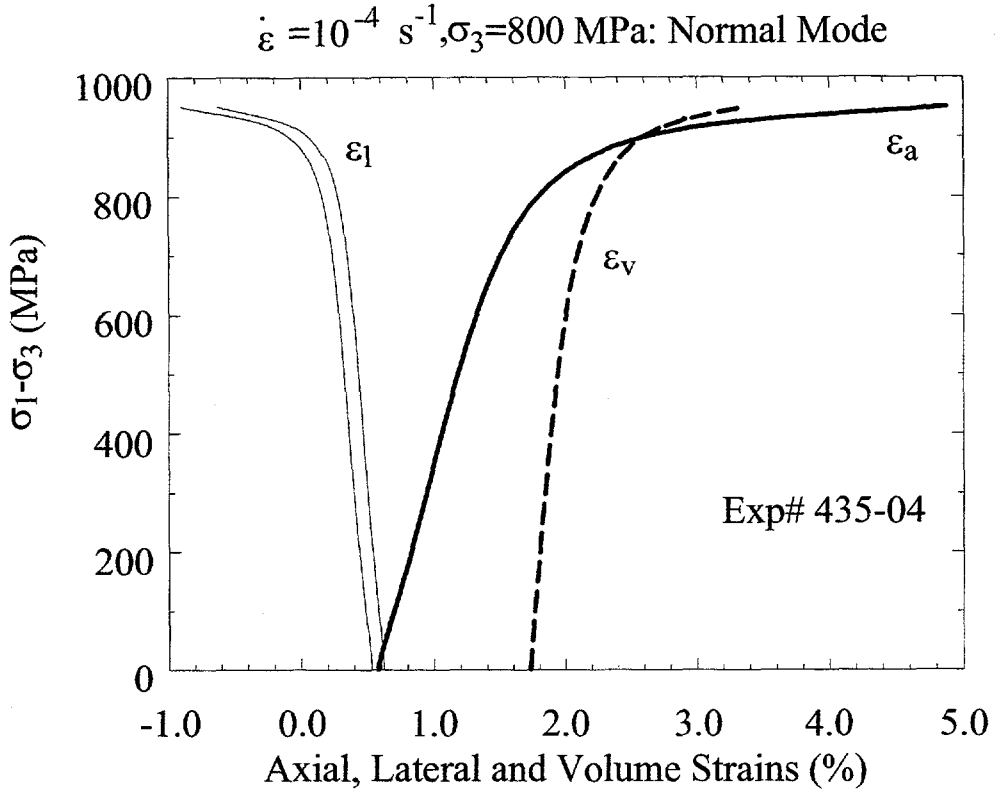

Figure 3.5: Normal-mode, triaxial compression experiment at $\dot{\epsilon}$=10^{-4}s^{-1} and σ_3=800 MPa. ϵ_a, ϵ_l and ϵ_v are the axial, lateral and volume strains, respectively.

each phenomenon to the total strain response. Investigation of this problem would be the subject of a lengthy report in itself, and, indeed, such a study is planned for the future. However, we believe that the qualitative evidence presented above is persuasive that (1) both processes are occuring, (2) we can roughly identify when each process begins, and (3) the two processes satisfactorily explain all of the observed pre-failure behavior.

We will discuss additional aspects of transformation and dipole rotation effects elsewhere in this report, particularly as they relate to the orientation-dependent, maximum compressive stress criterion that Zeuch *et al.* [1997; in preparation] have proposed for onset of the $F_{R1} \rightarrow A_O$ transformation under nonhydrostatic stress. Dipole rotation and transformation effects also contribute to differences between the stress-strain curves of specimens deformed in the normal and axial modes.

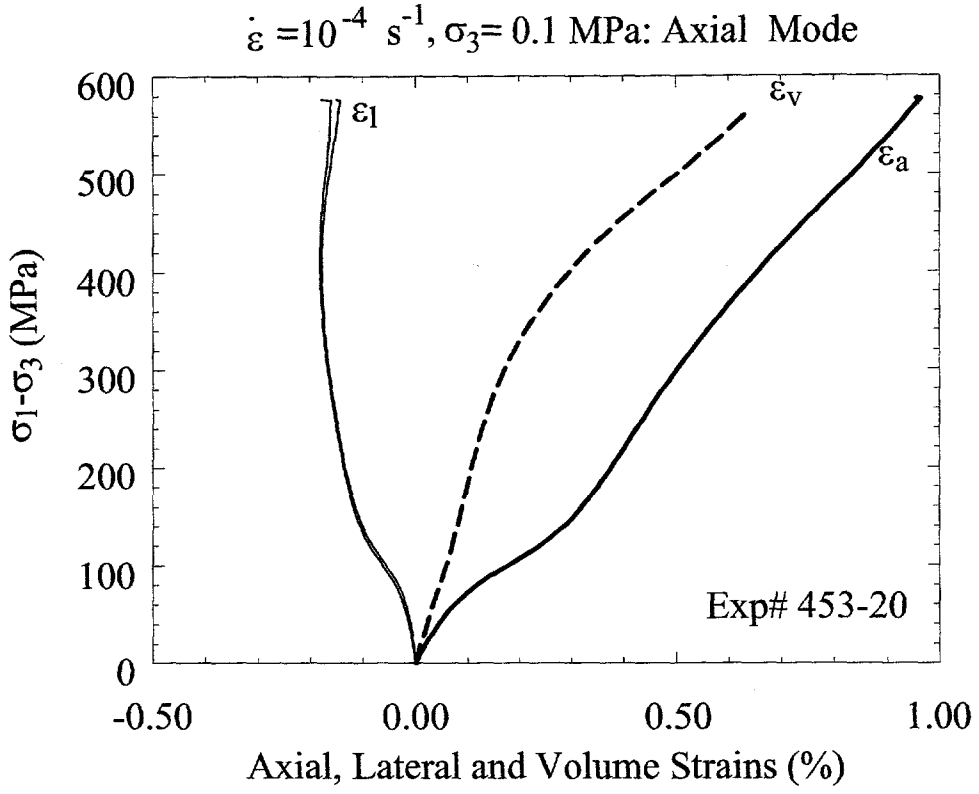

Figure 3.6: Axial-mode, uniaxial compression experiment at $\dot{\epsilon}$=10^{-4}s^{-1}. ϵ_a, ϵ_l and ϵ_v are the axial, lateral and volume strains, respectively.

3.2 Effect of Confining Pressure on Compressive Strength and Ductility

As expected (*e.g.*, Paterson [1978]), both strength and ductility (axial strain at failure) increase with confining pressure at constant strain rate (Tables 3.1 and 3.2). This is because application of increasing pressure progressively suppresses the nucleation, growth and connection of microcracks. The fracture mode changes progressively from explosive axial splitting in the absence of confinement (Figure 3.13a), to a single shear fracture (Figure 3.13b) at 100 MPa, to increasingly finely distributed shear microcracking at 200, 400 and 800 MPa (Figures 3.13c and 3.13d). Failure was marked by an audible "pop" at σ_3=0.1 and 100 MPa. No audible sounds were detected upon failure at or

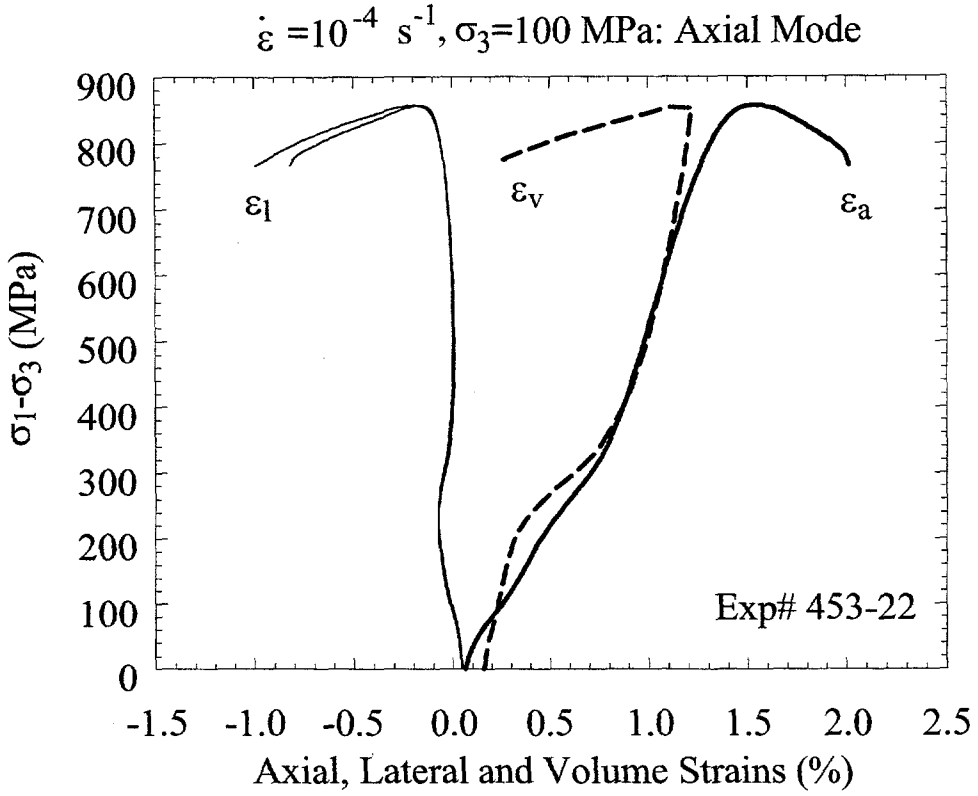

Figure 3.7: Axial-mode, triaxial compression experiment at $\dot{\epsilon}$=10^{-4}s^{-1} and σ_3=100 MPa. ϵ_a, ϵ_l and ϵ_v are the axial, lateral and volume strains, respectively.

above 200 MPa.

The form of the stress-strain curves also changes with increasing confining pressure, reflecting both the increases in strength and ductility. Figures 3.14-3.17 summarize the effects of confining pressure on strength and axial strain response for both strain rates, and deformation modes. As with other brittle polycrystalline materials [Paterson, 1978], the peak strength not only increases, but shifts to higher strains with increasing confinement.

Strength loss is instantaneous and catastrophic only under unconfined conditions. Although strength drops precipitously at σ_3=100 MPa, it is, nevertheless, at a measurable rate; the rate continues to slow with increasing confinement. At 200 and 400 MPa, strength loss is usually incomplete, with the ceramic continuing to support some stress well after reaching a peak. Eventually, at the highest confining pressure (800 MPa), the ceramic yields

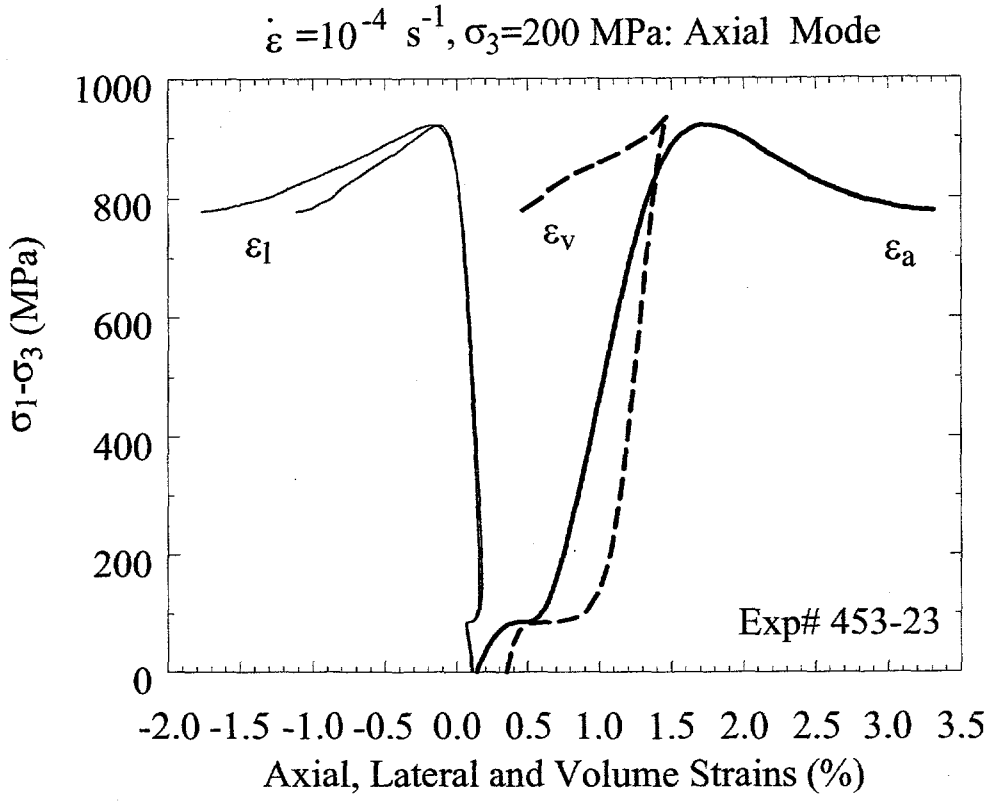

Figure 3.8: Axial-mode, triaxial compression experiment at $\dot{\epsilon}$=10^{-4}s^{-1} and σ_3=200 MPa. ϵ_a, ϵ_l and ϵ_v are the axial, lateral and volume strains, respectively.

but continues to work harden out to axial strains of 5-6%. It becomes difficult to pick a yield or failure strength under this last condition; we have somewhat arbitrarily picked the intersections of tangents to the initial and final portions of the curves (Table 3.1), which are substantially lower than the highest values attained (Figure 3.14).

Examination of Figures 3.14-3.17 indicates that increases in confining pressure above 100 MPa have steadily diminishing effects on strength at both strain rates. The data further suggest that by 800 MPa, confining pressure has no additional effect on strength, or, possibly, even reduces strength depending upon where one chooses "yield" or "failure" (Figure 3.14). This nonlinear and decreasing effect of confining pressure is conveniently summarized in Figure 3.18, and is identical to that reported for rocks [Paterson,

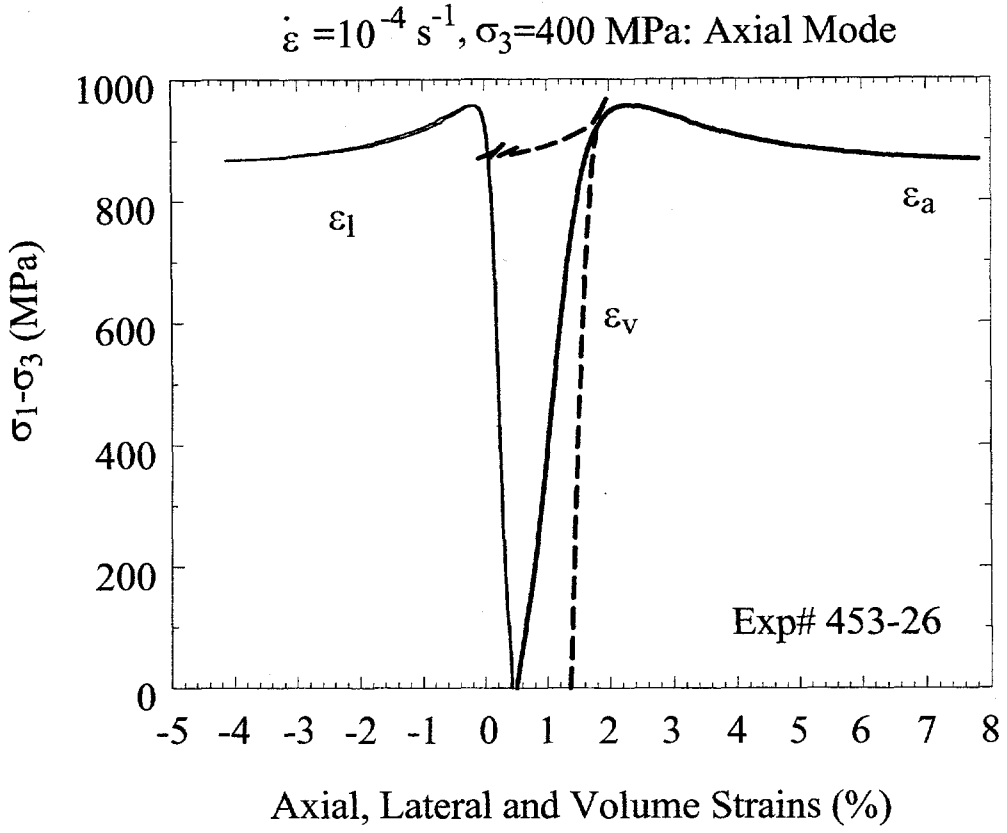

Figure 3.9: Axial-mode, triaxial compression experiment at $\dot{\epsilon}$=10^{-4}s^{-1} and σ_3=400 MPa. ϵ_a, ϵ_l and ϵ_v are the axial, lateral and volume strains, respectively.

1978; his Figures 8 and 9].

In the case of PZT 95/5-2Nb, this diminishing effect represents a change in the deformation mechanism between confining pressures of 400 and 800 MPa, as indicated in the plots of stress difference *versus* volume strain shown in Figures 3.19 and 3.20. Under unconfined conditions, the volumetric strain response is dominated by the $F_{Rl} \rightarrow A_O$ transformation right up until failure. Beyond the transformation at σ_3 =100 or 200 MPa, volumetric strain response is essentially linear elastic until failure. Concurrent with failure, the specimens begin to dilate rapidly. At 400 MPa, however, we observe another inflection point in the stress difference-volume strain plots just prior to failure, indicating that the specimen is once again beginning to compact. The compaction phase lasts only briefly, however, and the samples again dilate

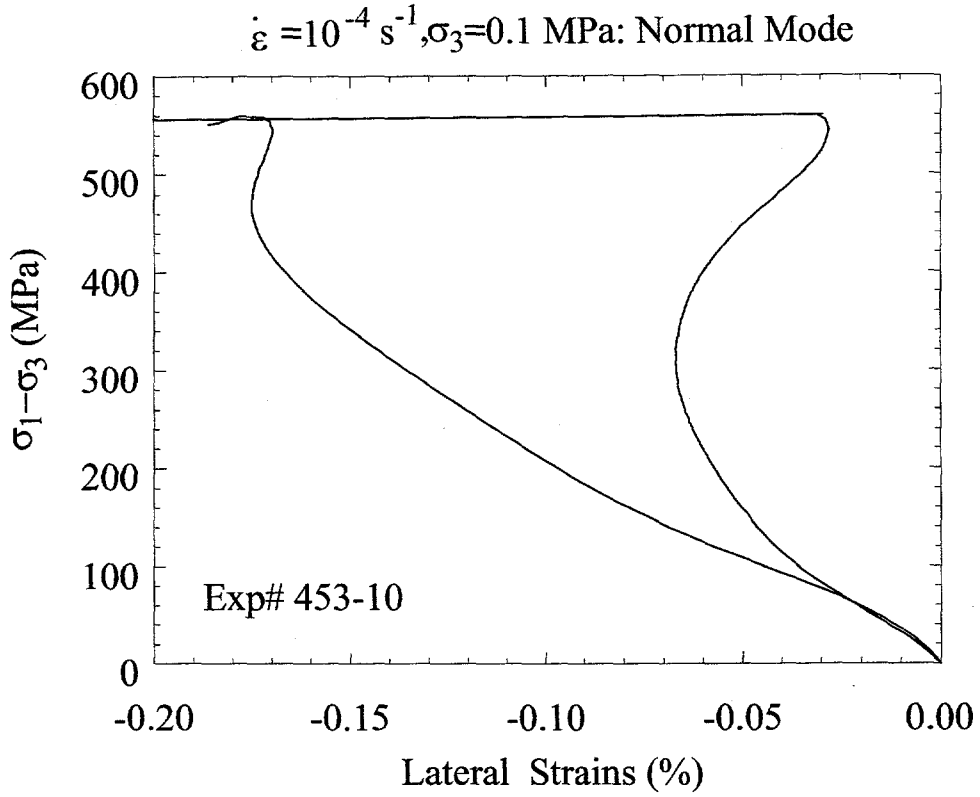

Figure 3.10: Detailed view of the lateral strains for the normal-mode uniaxial compression experiment shown in Figure 3.1. Note the two complete reversals of the strains prior to failure.

rapidly, slightly beyond the peak stress. This behavior is quite consistent at 400 MPa, for both orientations and both strain rates. In the two experiments that we performed at 800 MPa, however, the specimens continue to compact indefinitely.

We interpret these second episodes of compaction as the onset of pore collapse during deformation because we are not in the vicinity of any known transformations under these conditions [Fritz and Keck, 1978]. However, microstructural investigation would be required to confirm this. Such studies might prove difficult, owing to the crumbling nature At 400 MPa, we infer that microcracking still dominates pore collapse, and the samples eventually begin to dilate and soften. But by 800 MPa microcracking is sufficiently suppressed that pore collapse is stabilized. The specimens continue to harden as void space is reduced. In dynamic experiments, Chhabildas [1984] reported

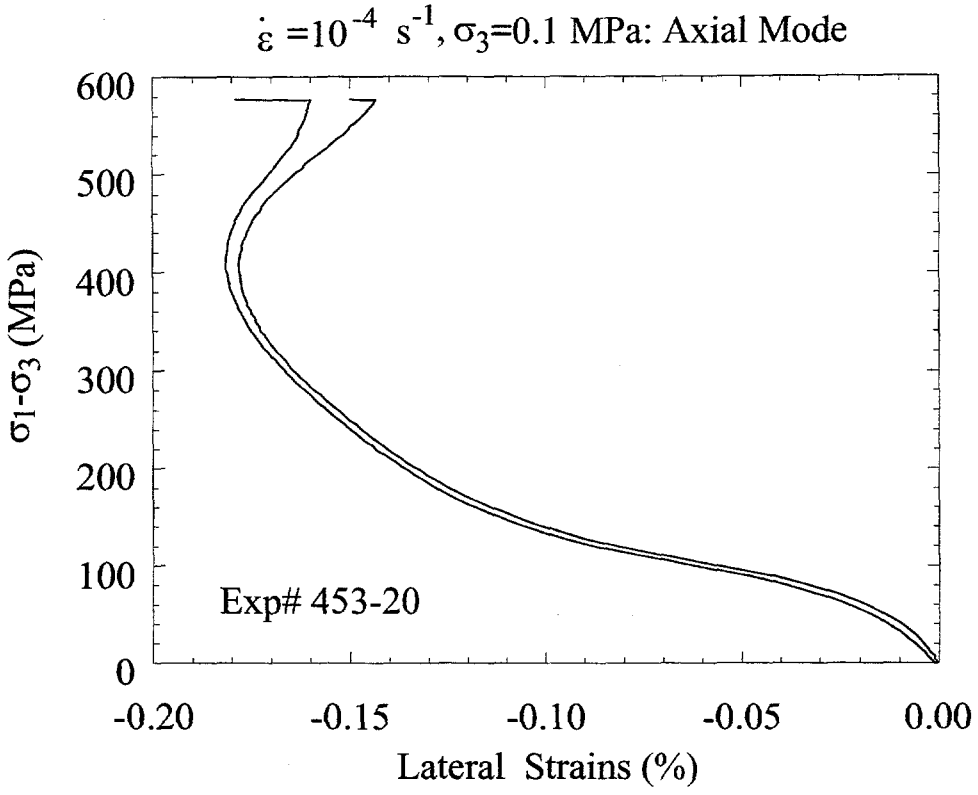

Figure 3.11: Detailed view of the lateral strains for the axial-mode uniaxial compression experiment shown in Figure 3.6. Note the two (almost) complete reversals of the strains prior to failure.

the onset of pore collapse at a nominal pressure of 2.6 GPa. This is substantially higher than the mean stress of about 0.7-1 GPa at which we observe the onset of pore collapse at a strain rate of 10^{-4} s^{-1}.

3.3 Effect of Strain Rate on Compressive Strength

Figure 3.18 also conveniently summarizes the effects of strain rate on compressive strength. At all confining pressures, the two-order-of-magnitude increase in strain rate uniformly results in a roughly 100 MPa increase in compressive strength. This corresponds to about a 19% increase in strength under unconfined conditions, and about an 11% increase at 400 MPa. Paterson [1978; p.32] cites an increase in compressive strength of about 10% for a

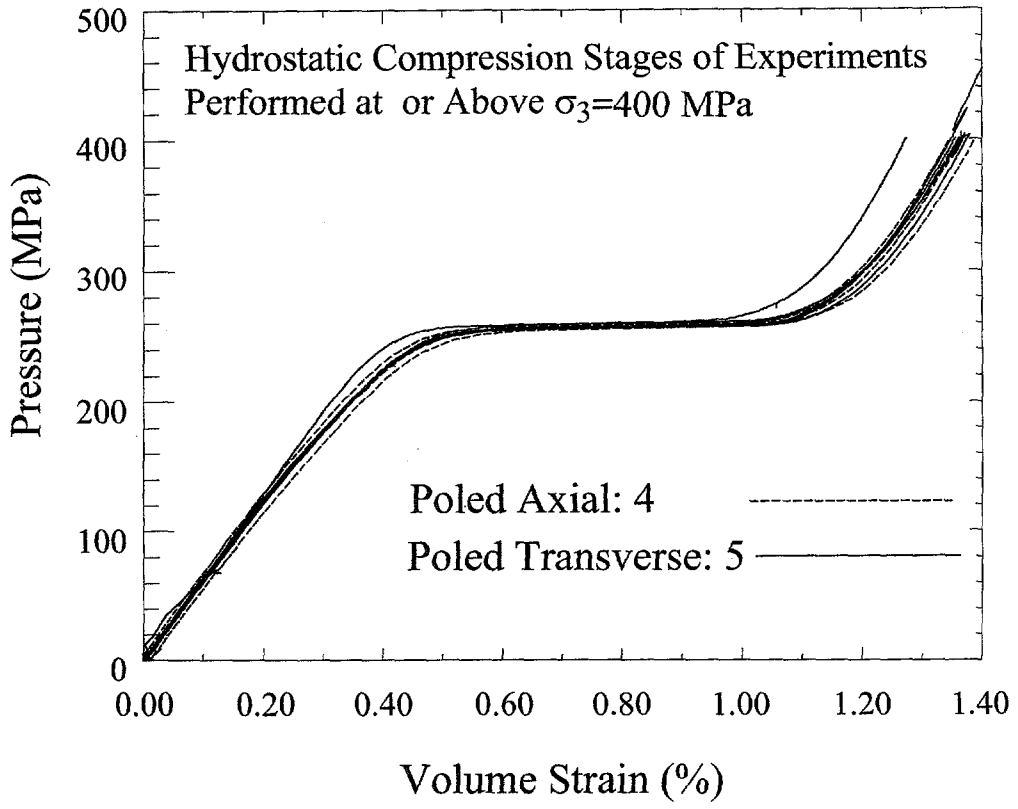

Figure 3.12: Hydrostatic compression stages of triaxial compression experiments performed at σ_3=400 or 800 MPa. Despite differences in poling direction and field, results are essentially identical.

10^3 increase in strain rate for limestone and several igneous rocks. Thus, PZT 95/5-2Nb appears to be somewhat more rate sensitive than other pressure-sensitive materials, but not greatly so.

Strict extrapolation of this strain rate effect to dynamic conditions would probably result in an underestimate of the true strength. Strain rate sensitivity generally increases dramatically above about $10^2 s^{-1}$ [Lankford, 1981; Olsson, 1991].

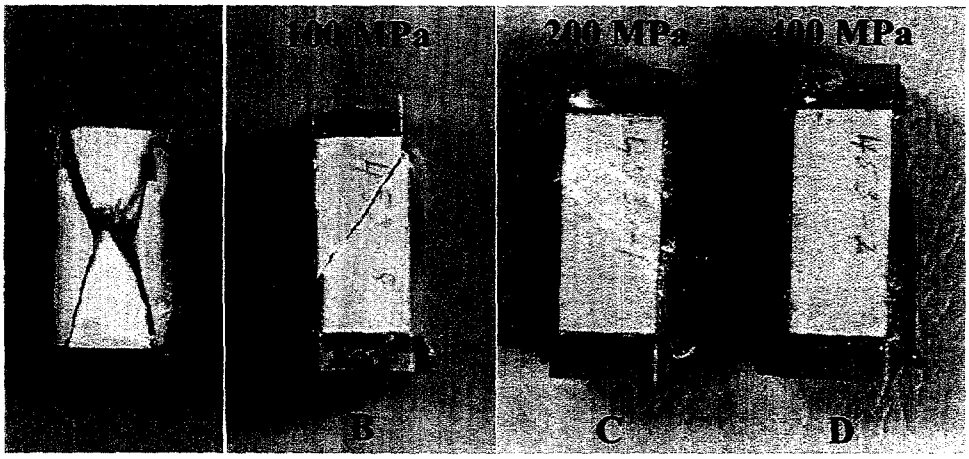

Figure 3.13: Failure modes at various confining pressures.

3.4 Orientation Effects

3.4.1 Strength and Ductility

The alert reader will note that the compressive strength data plotted for each strain rate in Figure 3.18 include results from specimens compressed in both the normal and axial modes. This is because we see no clear evidence that one orientation is consistently stronger than the other at either strain rate. We do, however, see some very weak indications that specimens compressed parallel to the poling direction exhibit more erratic behavior than those compressed perpendicular to the poling axis.

This evidence is most pronounced under unconfined conditions, where two of five axial-mode specimens (Table 3.2: 453-19 and 453-27) exhibited anomalously low strengths at both strain rates. Similarly, one axial-mode specimen exhibited an unusually low strength at σ_3 =400 MPa and $\dot{\epsilon}_a$ =10^{-4} s^{-1} (453- 25). These observations suggest the *possibility* that specimens poled parallel to the axis of compression have a wider range of strengths at the low end than specimens poled perpendicular to the axis of compression. However, many more experiments would have to be performed to establish this.

Specimens deformed in both the axial and normal modes undergo a brief period of apparent weakening, or enhanced axial ductility at onset of the transformation (*e.g.*, Figures 3.3 and 3.8). This effect is particularly pronounced in axial-mode specimens. However, this does not appear to translate to any significantly greater axial strains at failure. This effect might be considered a form of transformational plasticity, but that term is usually reserved for enhanced ductility that occurs under load during repeated cycling

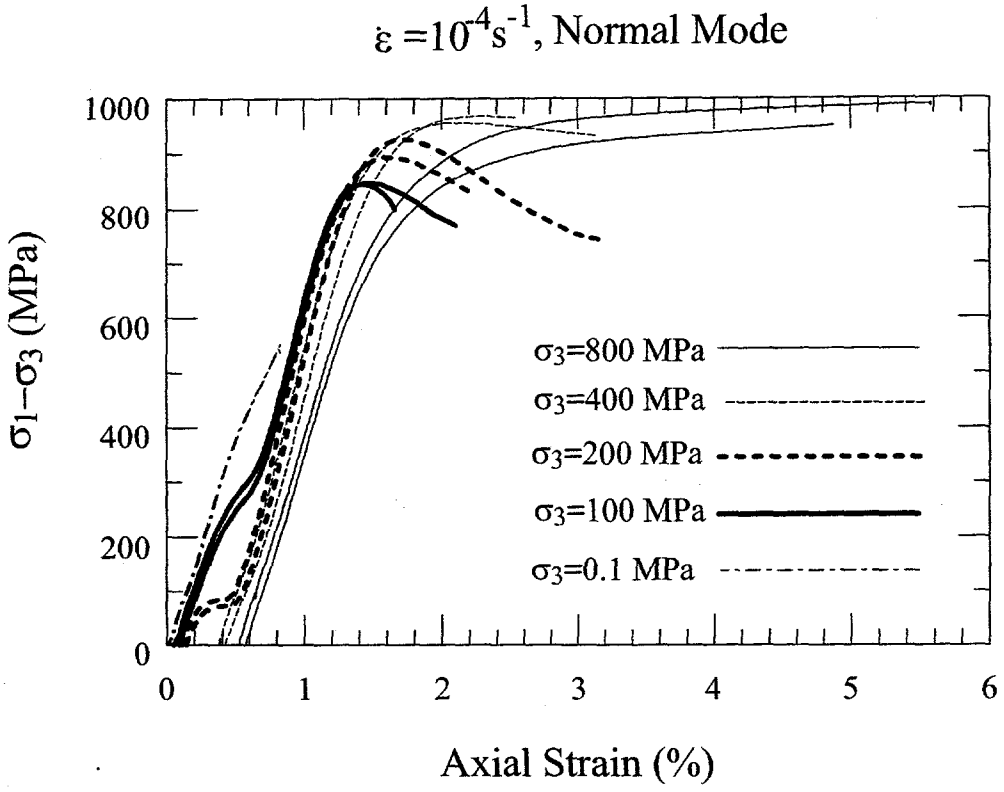

Figure 3.14: Summary plot of the effects of confining pressure on strength and ductility for normal-mode deformation at $\dot{\epsilon}$=$10^{-4}s^{-1}$.

across a polymorphic phase boundary [Poirier, 1982].

3.4.2 Stress-Strain Response: Elastic, Dipole Rotation and Transformation Effects

Despite similarities in maximum compressive strengths, there are pronounced differences in the stress-strain data for the two poling orientations for confining pressures at or below 200 MPa. Figure 3.21 compares results for unconfined experiments in the two different orientations at a strain rate of 10^{-4} s^{-1}. Axial and lateral strains are very different, which we attribute to several different, but related phenomena. We plan to investigate these processes in detail at a later date, and only offer qualitative explanations for the observations at this time. Our observations and explanations are generally consistent with those of Fritz [1979], and based in part on some earlier observations made by us during uniaxial compression experiments on poled

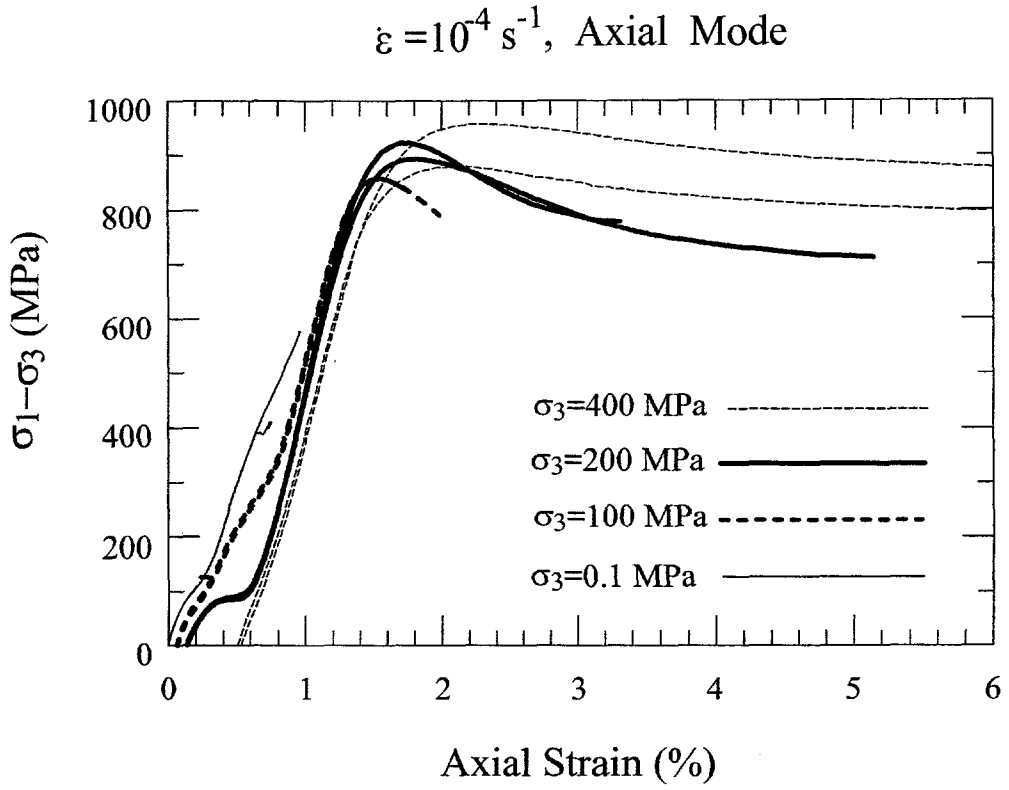

Figure 3.15: Summary plot of the effects of confining pressure on strength and ductility for axial-mode deformation at $\dot{\epsilon}=10^{-4}s^{-1}$.

and unpoled specimens from other PZT 95/5-2Nb hifires [Zeuch *et al.*, 1997; in preparation].

The poling process aligns a large fraction of the domains parallel or subparallel to the electric field, resulting in what is probably a concentric distribution about, and having a maximum parallel to, the poling direction. This results in mechanical anisotropy that is detectable even in hydrostatic compression experiments both prior to and during the phase transformation [Zeuch *et al.*, 1995]; this is illustrated in Figure 3.22 for hifire 453 ceramic. The anisotropy prior to the transformation is a consequence of the fact that PZT 95/5-2Nb is elastically softer parallel to the dipole [Fritz, 1979]. The anisotropy during the transformation is probably a consequence of release of locked-in mechanical strains caused by poling ("electrostrictive" strains), and/or greater intrinsic compressive strains parallel to the dipole direction during transformation. We have not investigated the relative contributions of the two effects.

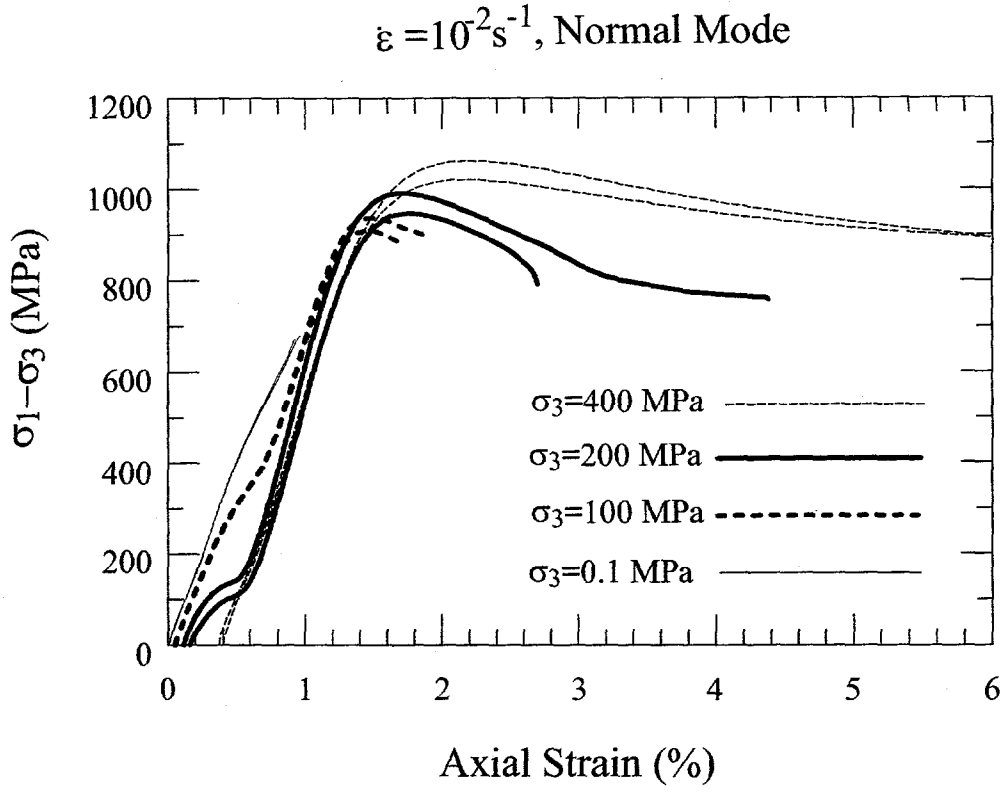

Figure 3.16: Summary plot of the effects of confining pressure on strength and ductility for normal-mode deformation at $\dot{\epsilon}$=$10^{-2}s^{-1}$.

In the case of axial mode deformation, the orientation distribution is coaxial with, and symmetric about, the directions of maximum compressive stress and strain. In the normal mode, the axis of the distribution is perpendicular to the directions of maximum compressive stress and strain. Even in the earliest stages of loading then, we would expect both (1) differences in elastic strain response between the two modes of deformation, (2) elastic anisotropy parallel to the axis of compression during axial-mode deformation, and (3) elastic anisotropy in the plane perpendicular to compression during normal-mode deformation.

In fact, the two types of specimens exhibit essentially linear, identical responses up to about axial stresses of 50-75 MPa, at which point they both depart dramatically from linearity, and from each other. It seems likely that the elastic differences are too small to resolve at these low stresses, and are masked at higher stresses first by inelastic dipole rotation and later by transformation effects.

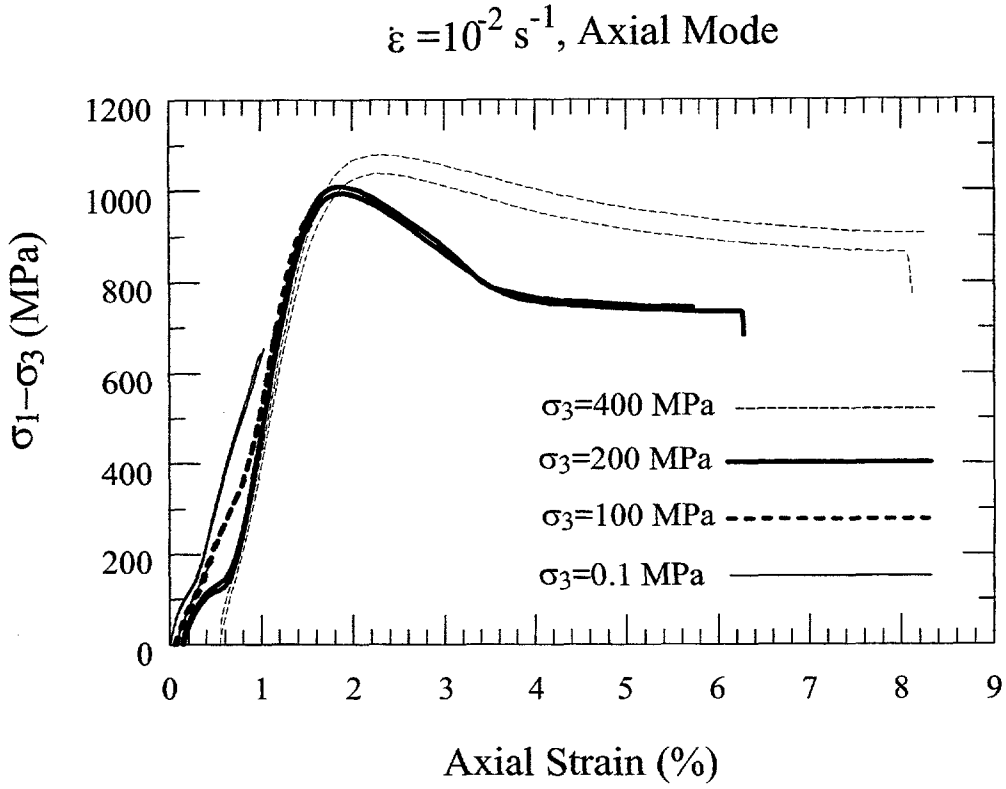

Figure 3.17: Summary plot of the effects of confining pressure on strength and ductility for axial-mode deformation at $\dot{\epsilon}$=10^{-2}s^{-1}.

If, as we suggest above and elsewhere [Zeuch *et al.*, 1997; in preparation], onset of the phase transformation begins when the volumetric strain response departs from linearity in the range of σ_1=200-250 MPa, then the nonlinearities starting at 50 to 75 MPa must be due to some other process or processes. As discussed above, and also shown by us elsewhere [Zeuch *et al.*, in preparation], these low-stress nonlinearities can reasonably be attributed to onset of stress-induced dipole rotation, rather than some sort of nonlinear elastic effect. We would expect the strain effects associated with dipole rotation to be different for the two differently poled specimens varieties.

Specimens deformed in the axial mode have a preponderance of dipoles oriented subparallel to the maximum compressive stress, and should therefore exhibit the greatest amount of rotation of dipoles away from the applied stress. Specimens deformed in the normal mode *already* have a preponderance of dipoles oriented perpendicular to the maximum compressive stress, and should therefore experience comparatively less strain caused by dipole

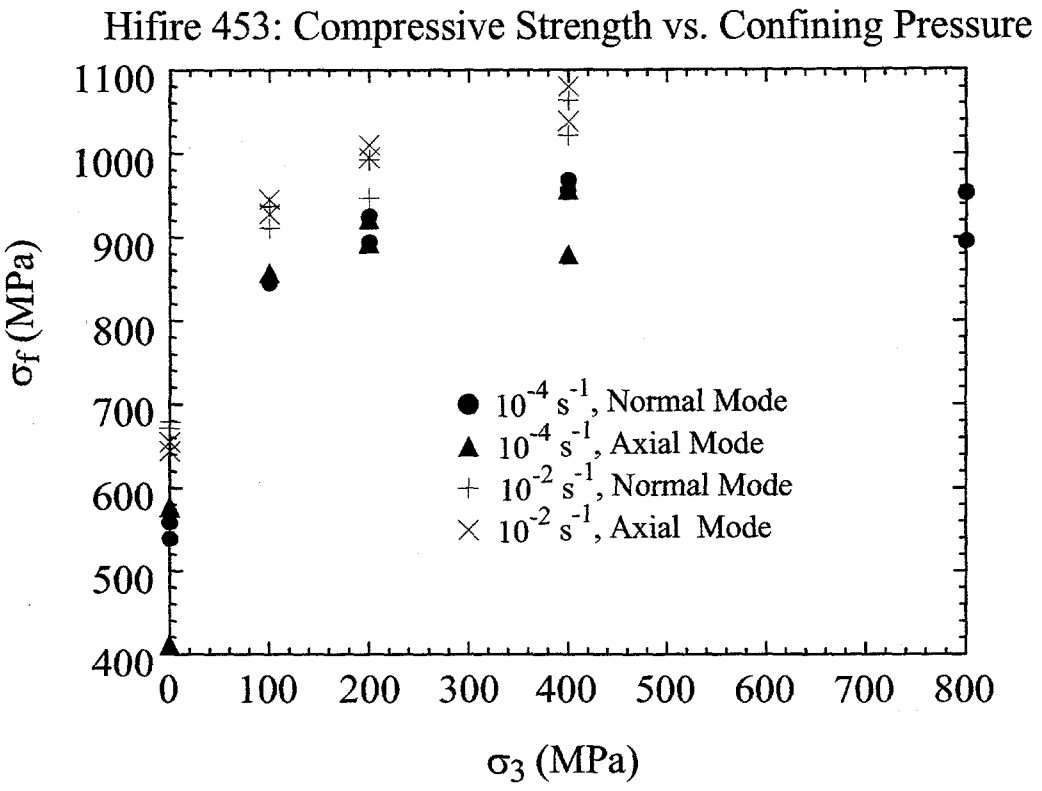

Figure 3.18: Summary plot of the effects of confining pressure and strain rate on the strength of poled, hifire 453 ceramic. Note that normal- and axial-mode experiments typically exhibit comparable strengths, though the scatter is perhaps greater for axial-mode experiments.

rotation. Furthermore, the distribution of dipoles should be symmetrical about the axis of compression in the axial mode, so we would expect lateral strains caused by dipole rotation to be symmetric about the axis of compression. In the normal mode, the distribution of dipoles is anisotropic in the plane perpendicular to the applied deviatoric stress, so we would expect the lateral strains caused by dipole rotation to be similarly anisotropic. In either instance, these larger, inelastic strains would likely mask smaller, elastic differences

This, in fact, is exactly what we observe (Figure 3.21). In the axial mode, the axial strain exhibits an anomalous, compressive departure from linearity at about σ_1=75 MPa, exactly what would be expected as the elongated dipoles rotate away from the applied stress. Similarly, the lateral strains

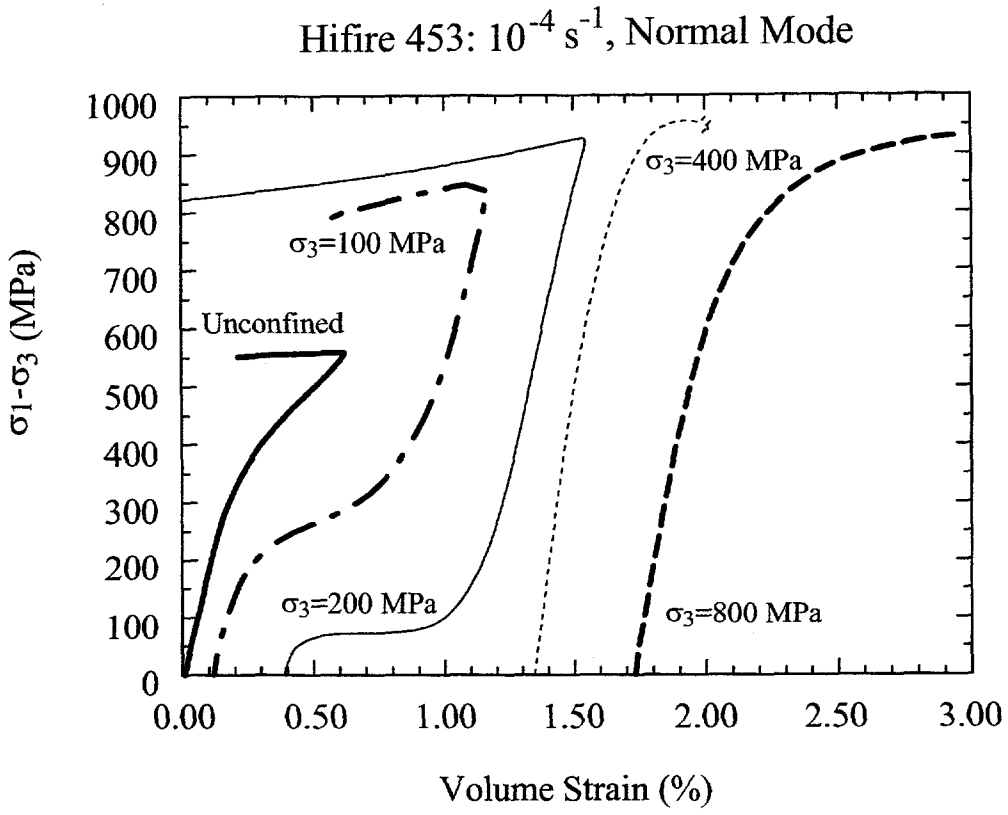

Figure 3.19: Plots of stress difference *vs.* volume strain for normal-mode experiments at $\dot{\epsilon}$=10^{-4}s^{-1}. Change in the failure mechanism is indicated by the change in the sense of volume strain at failure at confining a pressure somewhere above 400 MPa. The change to a compressive sense indicates that pore collapse is becoming important.

display a sudden, anomalous dilatational departure from linearity at exactly the same time. Note also that the lateral strains are identical, as would be expected for compression coaxial with the distribution of dipoles.

The specimen deformed in the normal mode also exhibits sudden departures from linearity in its axial and lateral strains at about 75 MPa. In contrast to the axial mode, however, the lateral strains are anisotropic, and the departures from linearity are less pronounced than those for the axial mode. Note also that lateral strain parallel to the poling direction is less than the lateral strain perpendicular to the poling direction, also as would be expected. Thus, it appears that the nonlinearities in the stress-strain response that begin at about 75 MPa can be attributed to the onset of ap-

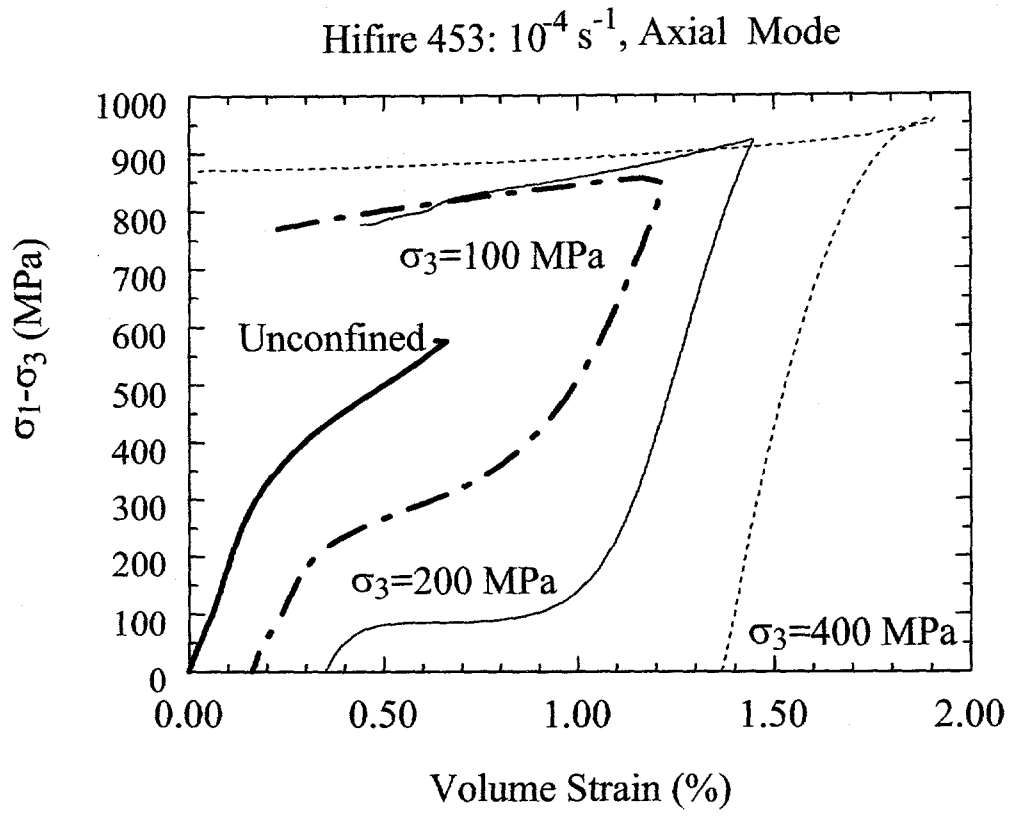

Figure 3.20: Plots of stress difference *vs.* volume strain for axial-mode experiments at $\dot{\epsilon}$=$10^{-4}s^{-1}$. Although no experiment was performed at σ_3=800 MPa, the same systematics that indicated the impending onset of stable pore collapse as a failure mechanism in Figure 3.19 are present here.

preciable amounts of dipole rotation. It is less clear when or if this process terminates, given that the transformation may still be continuing (at least in uniaxial compression) when the specimens fail [Fritz, 1979; Zeuch *et al.*, 1997; in preparation].

At a stress of 200-250 MPa, the volume strains finally depart from linearity (Figure 3.21), indicating onset of the transformation [Zeuch *et al.*, 1997; in preparation]. For the same reasons outlined above, we would expect lateral transformation strains associated with axial-mode deformation to be identical, whereas those associated with normal-mode deformation would be greater in the direction parallel to poling. Again, this is generally what we observe. Lateral strains in axial-mode specimens are identical right up to failure (Figure 3.21). Lateral strains in normal-mode specimens continue to

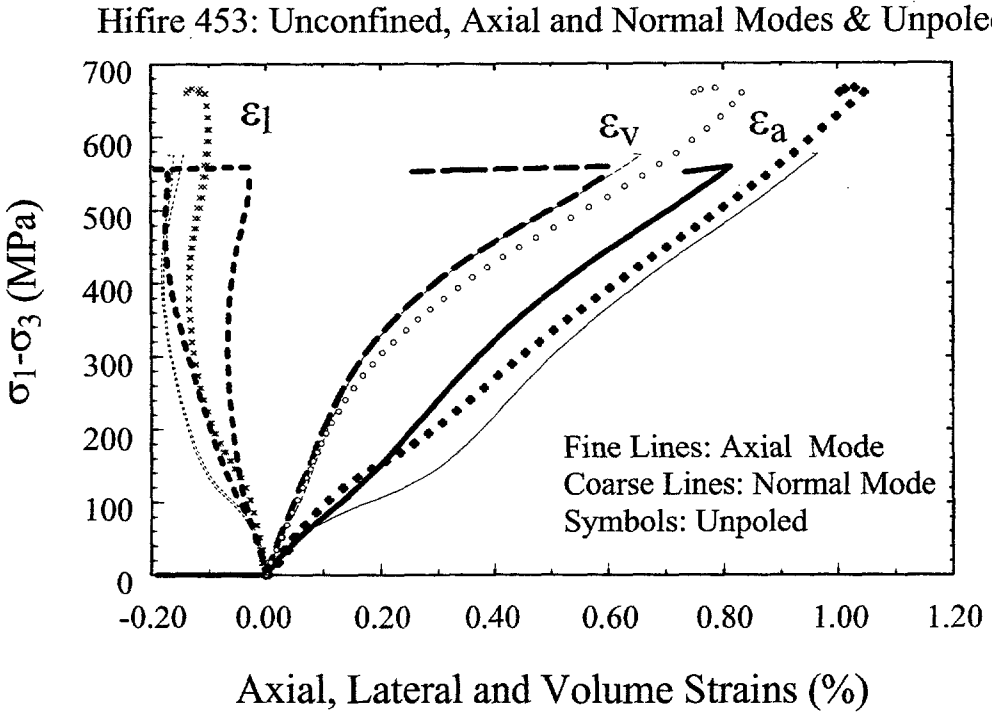

Figure 3.21: Normal- and axial-mode, uniaxial compression experiments on hifire 453 ceramic. ϵ_a, ϵ_l and ϵ_v are the axial, lateral and volume strains, respectively. Results from a similar experiment on unpoled ceramic are shown for comparison.

diverge right up until failure.

As noted earlier, many of the conclusions in this section are qualitative and based largely on the earlier work of Fritz [1979] and ourselves [Zeuch *et al.*, 1997; in preparation]. It is our intention to further investigate the relationship between applied stress and dipole rotation, using additional diagnostics such as acoustic velocity measurements and changes in electrical state.

3.4.3 Effect of Poling Direction on Onset of the $F_{R1} \rightarrow A_O$ Transformation in Triaxial Compression

Zeuch *et al.* [1994] showed that a convincing case could be made that under nonhydrostatic compression, the $F_{R1} \rightarrow A_O$ transformation of unpoled PZT 95/5-2Nb ceramic began when the maximum compressive stress, σ_1, equalled the hydrostatic pressure at which the transformation would otherwise take

place. Zeuch *et al.* [1997; in preparation] noted that this prediction did not seem to apply to poled ceramic deformed in the normal mode in constant-stress-difference experiments. However, they showed that the results for poled ceramic could be qualitatively reconciled with those for unpoled if not only the magnitude of the compressive stress, but also its orientation relative to the crystallography of PZT 95/5-2Nb, determined onset of the transformation. Zeuch *et al.* [in preparation] showed that under constant-stress-difference conditions, poled ceramic appeared to transform when the compressive stress on a plane at 45° to the poling direction equalled the hydrostatic pressure at which the transformation of poled ceramic otherwise occurred. The reasons for the particular 45° angle were not identified, but appeared to confirm the importance of orientation as well as magnitude of the stress for onset of the transformation.

If the stress-orientation dependence predicted by Zeuch *et al.* [1997; in preparation] is correct, we might expect to see some difference in onset of the phase transformation between those specimens deformed in the normal and axial modes. The two orientations were poled using different field strengths. Thus, the intensities (so to speak) of the poling-induced preferred crystallographic orientations should also be different for the two types of specimen. For any given triaxial stress state, then, the differently-poled specimens present different populations of domains that are favorably oriented for transformation to occur.

In fact, we see no difference between the volumetric strain behaviors of the two types of specimens, indicating that the transformation began at the same stress level, and proceeded identically for the two different poling orientations. This observation is troubling for the proposed qualitative, orientation-dependent model proposed by Zeuch *et al.* [in preparation], because it is difficult to understand how two very different field strengths, applied at orientations 90° apart, could result in a domain distribution (or distributions) that yield the same transformation behavior. We acknowledge that this observation appears to contradict our model, and we have no fully credible explanation for it at this time. However, the model continues to explain many observations for several other hifires, and abandonment is not warranted at this time.

One possibility is that the domain orientations in the axial mode specimens is highly unstable relative to the stress orientation. Domain rotation clearly begins in axial mode specimens at a stress difference of about 75 MPa, when the axial strain curves for uniaxially compressed, axial- and normal-mode specimens deviate from one another (Figure 3.21). However, by a stress difference of about 160 MPa, the axial strain plots for the two deformation modes are identical, albeit separated by a fixed strain, presumably that due

to dipole rotation. The similarity of the axial stress-strain plots suggests that by the time a certain axial stress level is reached, that applied axial stress has completely modified the domain distribution of the axial mode specimens, such that they strongly resemble the normal mode specimens. If this rearrangement occurs prior to triggering of the transformation, then the normal-mode and axial-mode specimens will transform at essentially the same stress conditions.

Careful testing in the future will be required to evaluate this possibility.

3.5 Additional Observations on Poled 453 Ceramic

The uniaxial and triaxial compression experiments that we discuss here are different from our earlier constant-stress-difference (CSD) experiments in that the shear stress, as well as the mean stress applied to the specimens is constantly increasing. However, as with our CSD experiments, we can plot mean stress *versus* volume strain and compare the results with the hydrostatic compression experiments. We do this in Figures 3.23 and 3.24 for both the normal mode and axial mode experiments performed at 10^{-4} s^{-1}. The rate of change of the mean stress for the 10^{-4} s^{-1} experiments is comparable to that for the hydrostatic compression tests, and so this comparison is warranted (Figure 3.25). The experiments at 10^{-2} s^{-1} pressurize two order of magnitude faster, and so the transformation is shifted to somewhat higher mean stresses relative to the hydrostatic tests (Figure 3.26 and 3.27).

Poled 453 ceramic exhibits the same depression of mean stress for onset of the transformation with increasing shear stress that we have observed in all of our previous investigations of poled and unpoled ceramic [Zeuch *et al.*, 1992a,b; 1995; 1997; in preparation]. However, since we are changing both shear and mean stress at the same time in these triaxial compression experiments, we need to look at plots of both variables against volume strain to confirm this.

In Figure 3.28 we replot the results for normal mode experiments conducted at 10^{-4} s^{-1} and confining pressures of 0.1, 100 and 200 MPa; that is, the normal-mode experiments at 10^{-4} s^{-1} which underwent transformation. In Figure 3.28a, we plot stress difference *vs.* volume strain, and in Figure 3.28b, mean stress *vs.* volume strain. Again, assuming that the departure from linearity indicates onset of the transformation for both plots, it is clear from Figure 3.28 that transformations that are triggered at the highest shear stresses are also triggered at the lowest mean stresses, as observed previously.

Furthermore, the transformations that occur at the highest mean stresses

and lowest shear stresses (*i.e.*, experiments at σ_3 =200 MPa), proceed fastest as indicated by the narrow range of stresses spanned before the transformation is completed. Transformations that are triggered at the lowest mean stresses and highest shear stresses (the unconfined experiments) proceed most sluggishly, as indicated by the wide band of stresses that are spanned prior to failure. This is again consistent with our earlier observations, and with our qualitative model that it is the maximum compressive stress that largely controls onset of the transformation of the ceramic polycrystal, and mean stress that controls completion.

Specimens deformed at σ_3 =200 MPa begin axial loading at a confining pressure quite close to the hydrostatic pressure for onset of the transformation. Only a small additional increment of axial loading is required to reach the compressive stress necessary to start the transformation, and a correspondingly small increment needed to reach the mean stress required to complete the transformation. Unconfined experiments and experiments that begin at σ_3 =100 MPa simply take longer to span the range of compressive stresses needed first to start and then complete the transformation for all domain orientations, as shown in Figure 3.29.

In Figure 3.30 we replot the results from uniaxial and triaxial compression tests on 453 ceramic in terms of $\frac{(\sigma_1+\sigma_3)}{2}$ *vs.* volume strain. Unlike our results for CSD experiments on poled ceramic from hifires 541-1 an 424, this does not convincingly reconcile or bring the data into "registry" with the hydrostatic compression experiments. This suggests that the domain orientation for the poled 453 must be somewhat different from that for the other two hifires, despite the similar electric fields that were applied to each set of specimens. By a process of trial and error we could probably find an angular relationship between applied stress and volume strain that achieves the desired result, but in the absence of additional diagnostics to identify the onset of the transformation, this does not appear to be a profitable endeavor at this time.

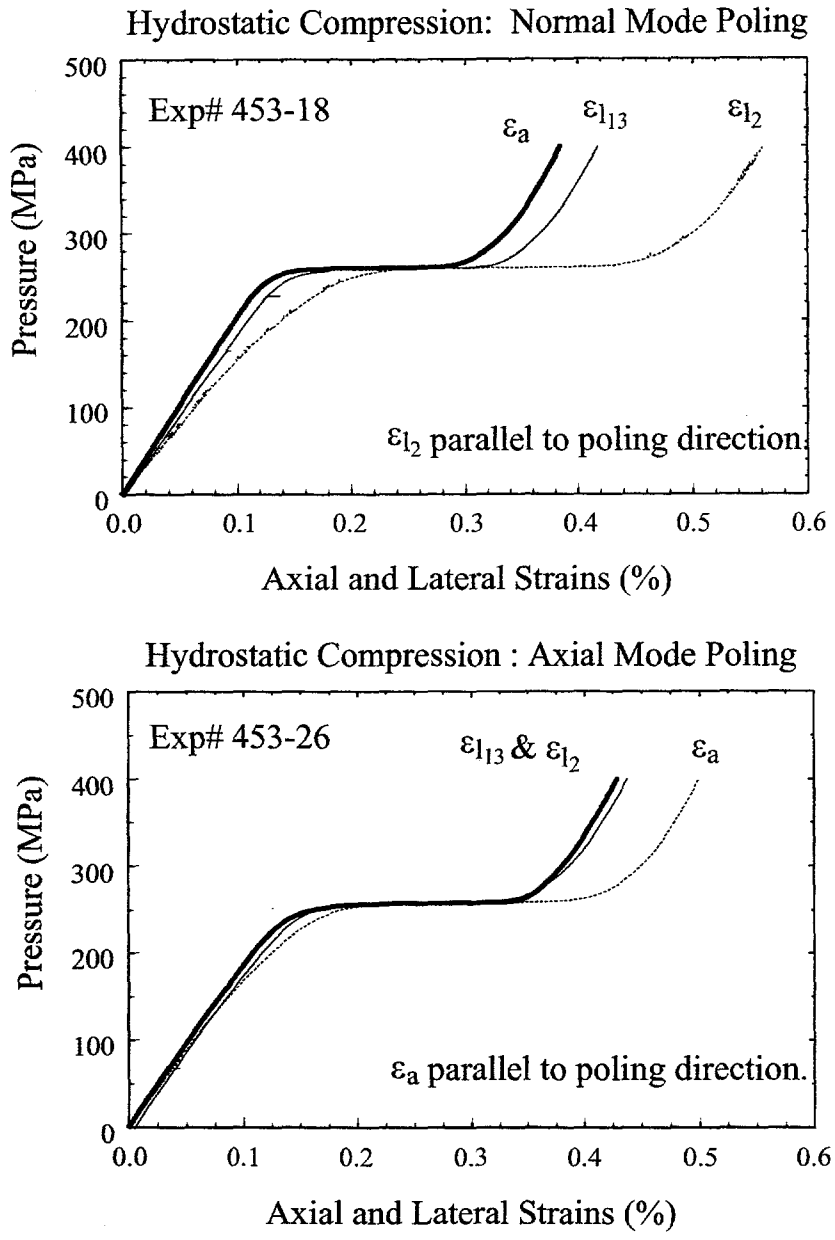

Figure 3.22: Anisotropic strain behavior of poled PZT 95/5-2Nb ceramic during the $F_{R1} \rightarrow A_O$ transformation under hydrostatic compression. ϵ_a is the axial strain, and ϵ_{13} and ϵ_2 are the two orthogonal, lateral strains. Poling directions are indicated on the plots.

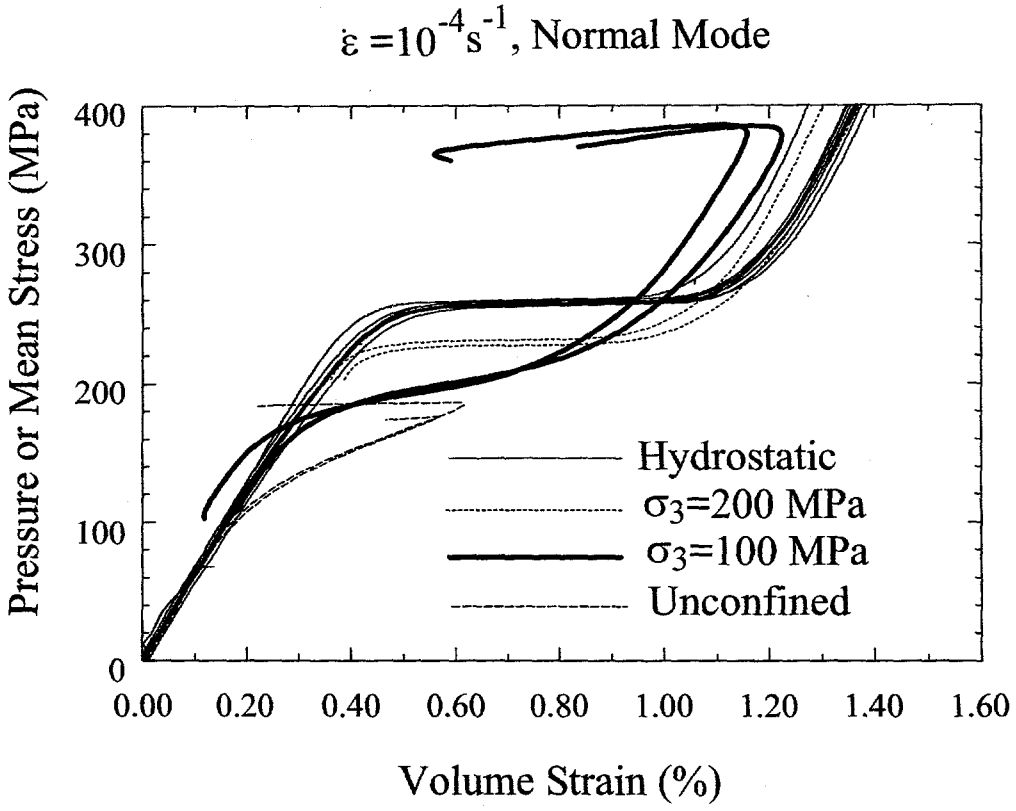

Figure 3.23: Plots of mean stress *vs.* volume strain for normal-mode, uniaxial and triaxial compression experiments at $\dot{\epsilon}$=10^{-4}s^{-1} and confining pressures $\leq$200 MPa. Hydrostatic compression experiments are shown for comparison.

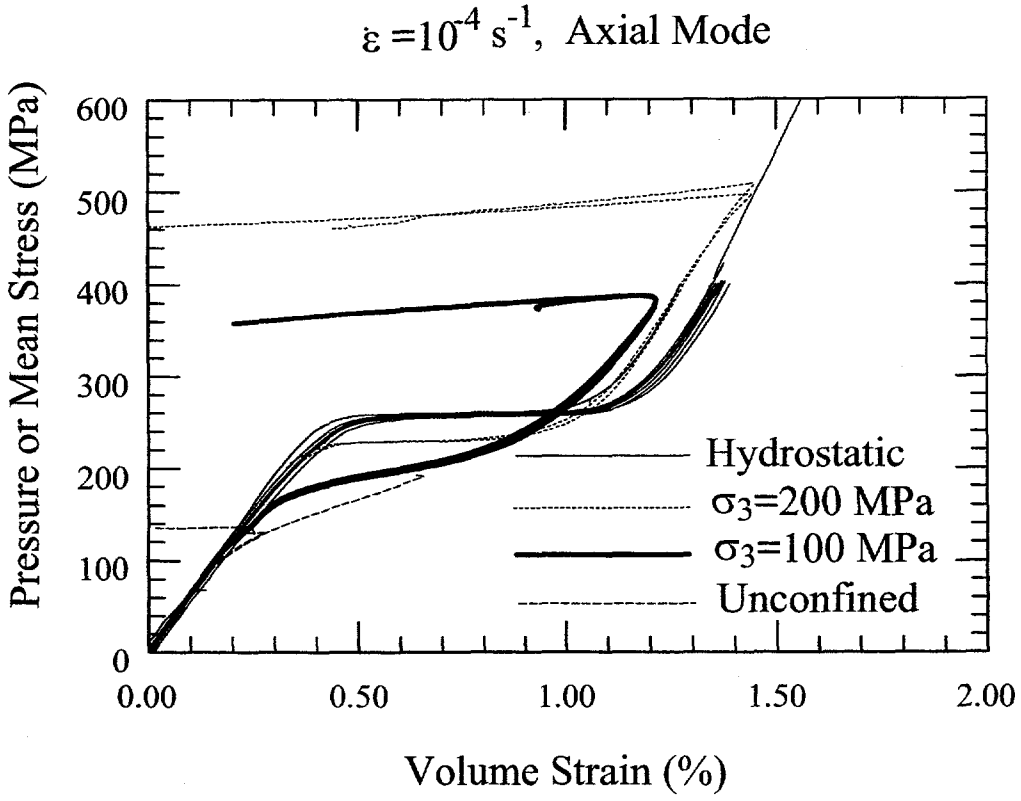

Figure 3.24: Plots of mean stress *vs.* volume strain for axial-mode, uniaxial and triaxial compression experiments at $\dot{\epsilon}=10^{-4}s^{-1}$ and confining pressures $\leq$200 MPa. Hydrostatic compression experiments are shown for comparison.

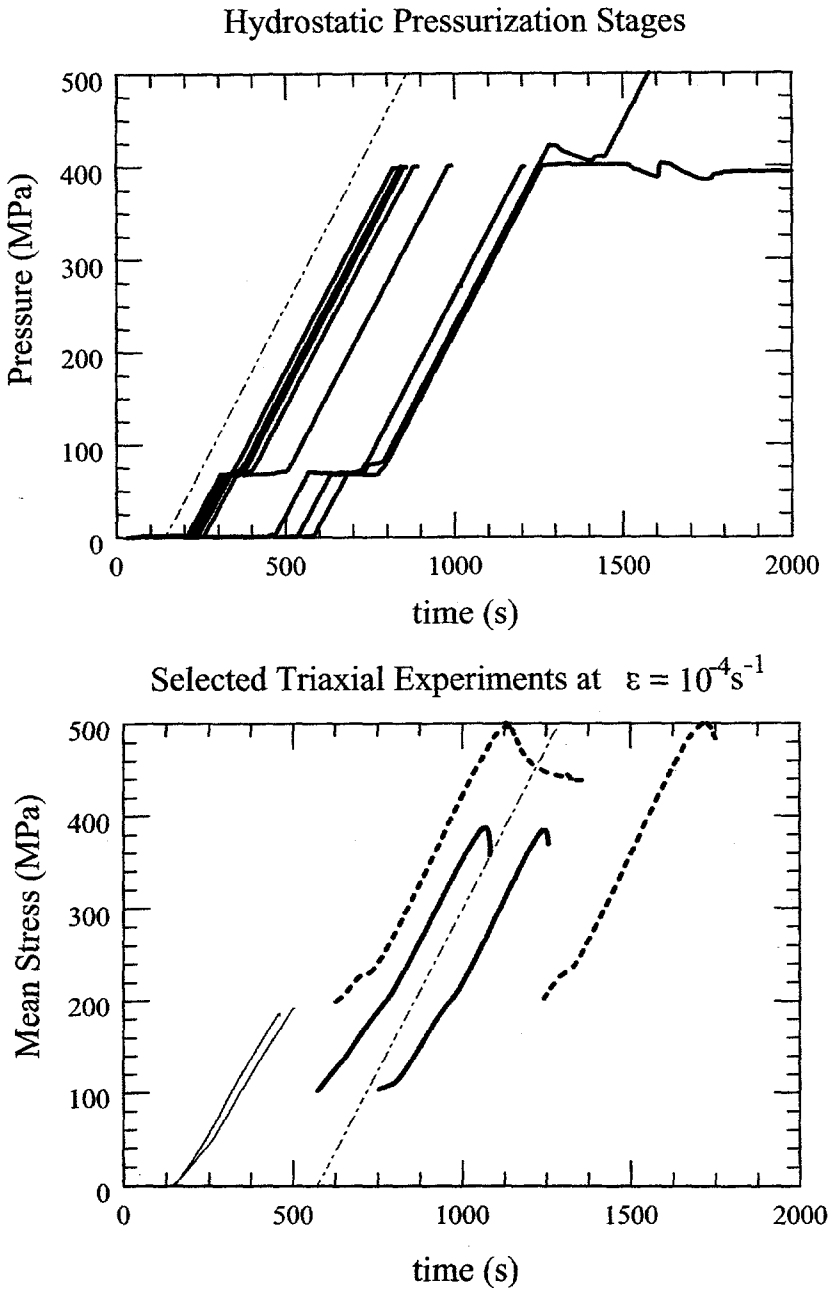

Figure 3.25: Top: Plots of pressure *vs.* time for the hydrostatic compression stages of experiments conducted at 400 or 800 MPa. Broken line has a slope of 0.69 MPa s^{-1}. Bottom: Plots of mean stress *vs.* time for the same normal-mode experiments shown in Fig. 3.24. Despite some variation, the rate of change of the mean stress is very similar to that for the hydrostatic compression experiments (top).

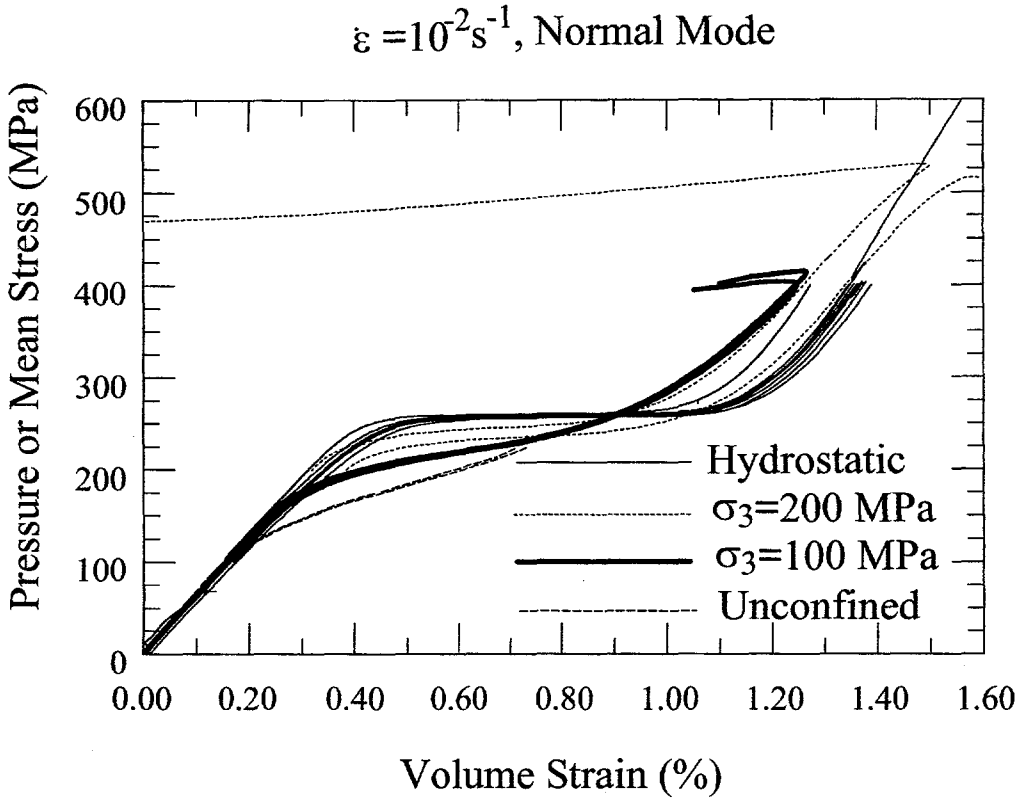

Figure 3.26: Plots of mean stress *vs.* volume strain for normal-mode, uniaxial and triaxial compression experiments at $\dot{\epsilon}$=$10^{-2}s^{-1}$ and confining pressures $\leq$200 MPa. Hydrostatic compression experiments are shown for comparison.

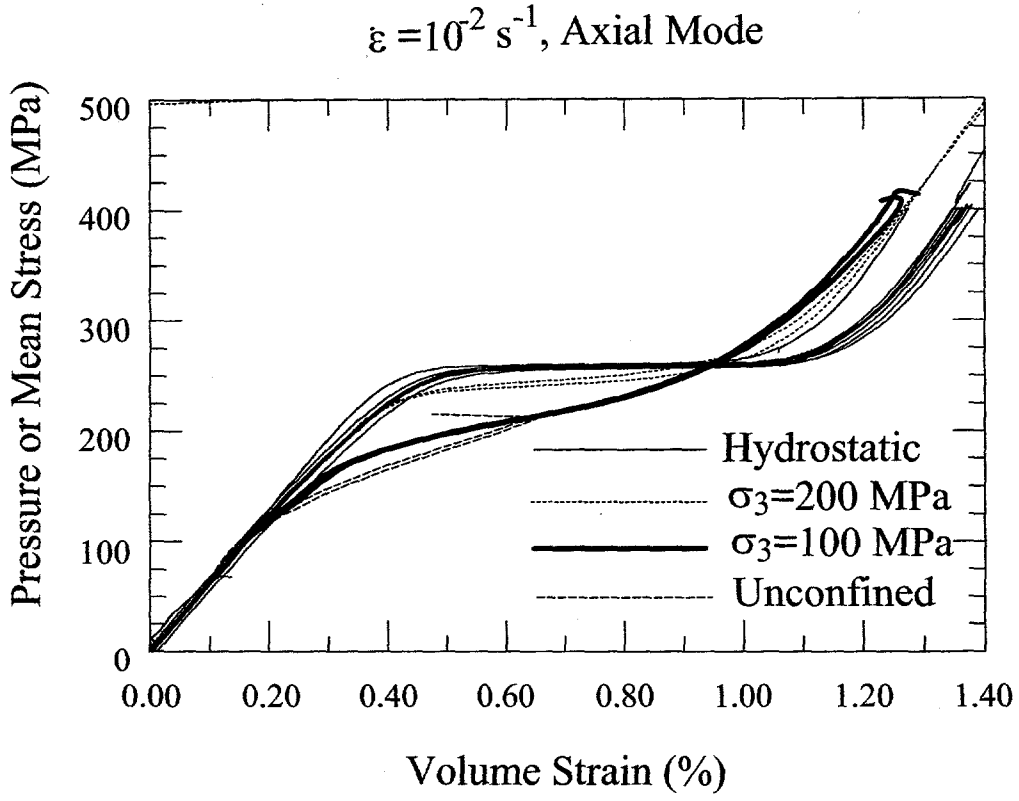

Figure 3.27: Plots of mean stress *vs.* volume strain for axial-mode, uniaxial and triaxial compression experiments at $\dot{\epsilon}=10^{-2}s^{-1}$ and confining pressures $\leq$200 MPa. Hydrostatic compression experiments are shown for comparison.

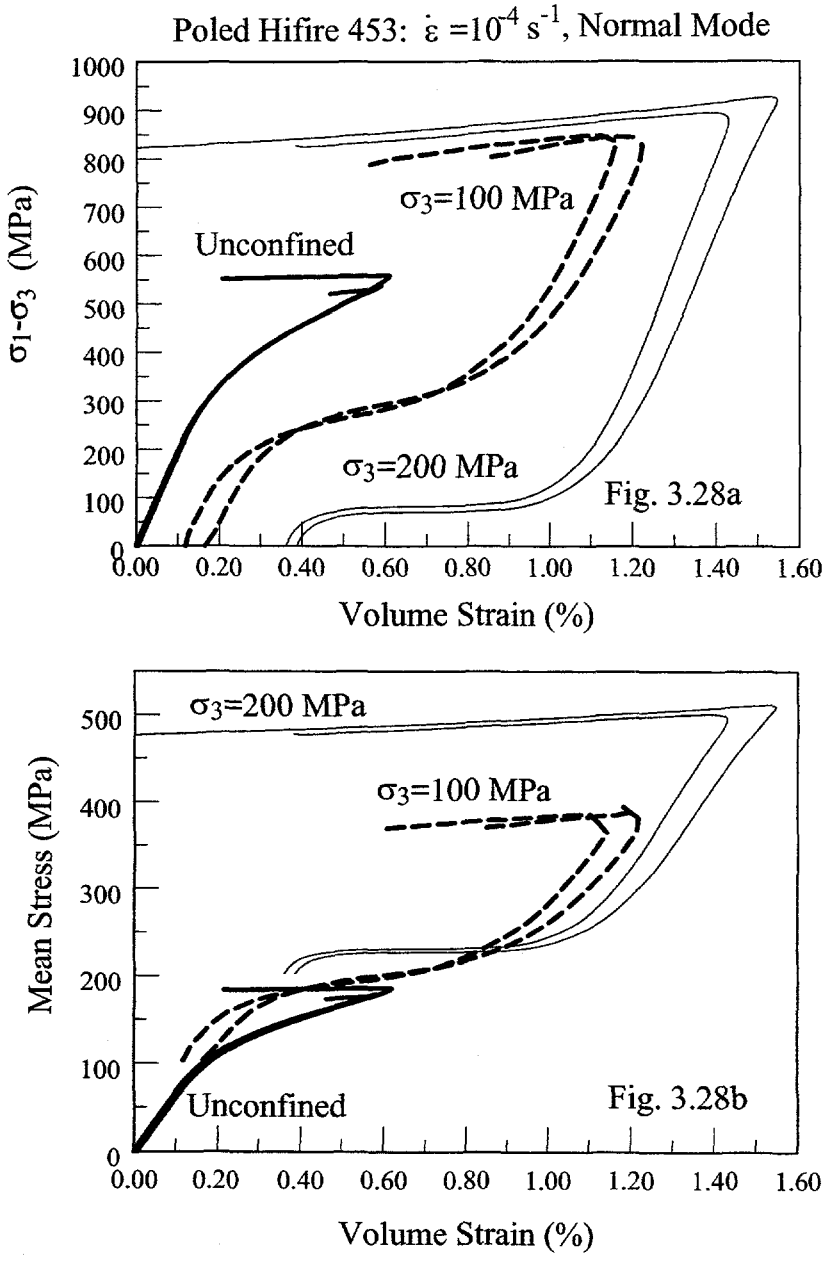

Figure 3.28: Top: Plot of stress-difference *vs.* volume strain for normal-mode, uniaxial and triaxial compression experiments at $\dot{\epsilon}$=10^{-4}s^{-1} and confining pressures ≤200 MPa. Bottom: Plots of mean stress *vs.* volume strain for the same experiments shown above. Note that the specimens that transform at the highest stress differences transform at the lowest mean stresses as indicated by the volume strain anomaly.

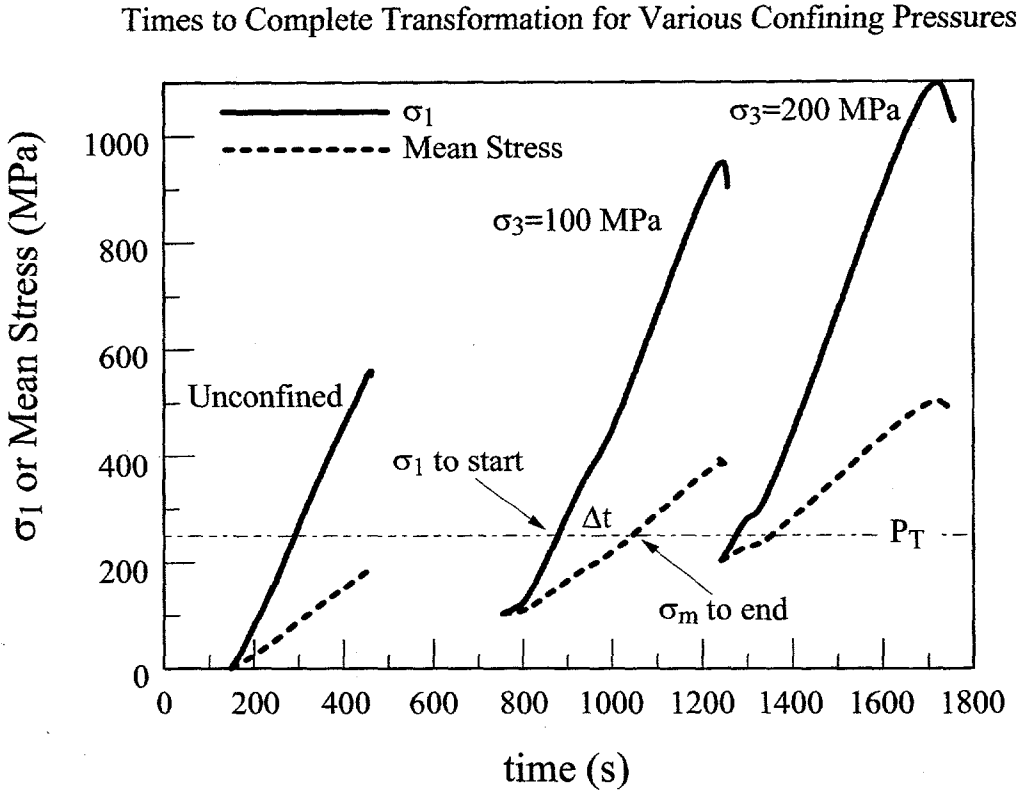

Figure 3.29: Plots of σ_1 and mean stress *vs.* time for three normal-mode experiments at $\dot{\epsilon}$=10^{-4}s^{-1}. The time required to complete transformation is the time difference, Δt, between reaching the value of σ_1 required to start the transformation, and the mean stress required to complete it. The closer the confining pressure is to the hydrostatic pressure for the transformation, P_T, the shorter this time span necessarily is. Note that in uniaxial compression tests, failure occurs before the mean stress for completion is reached.

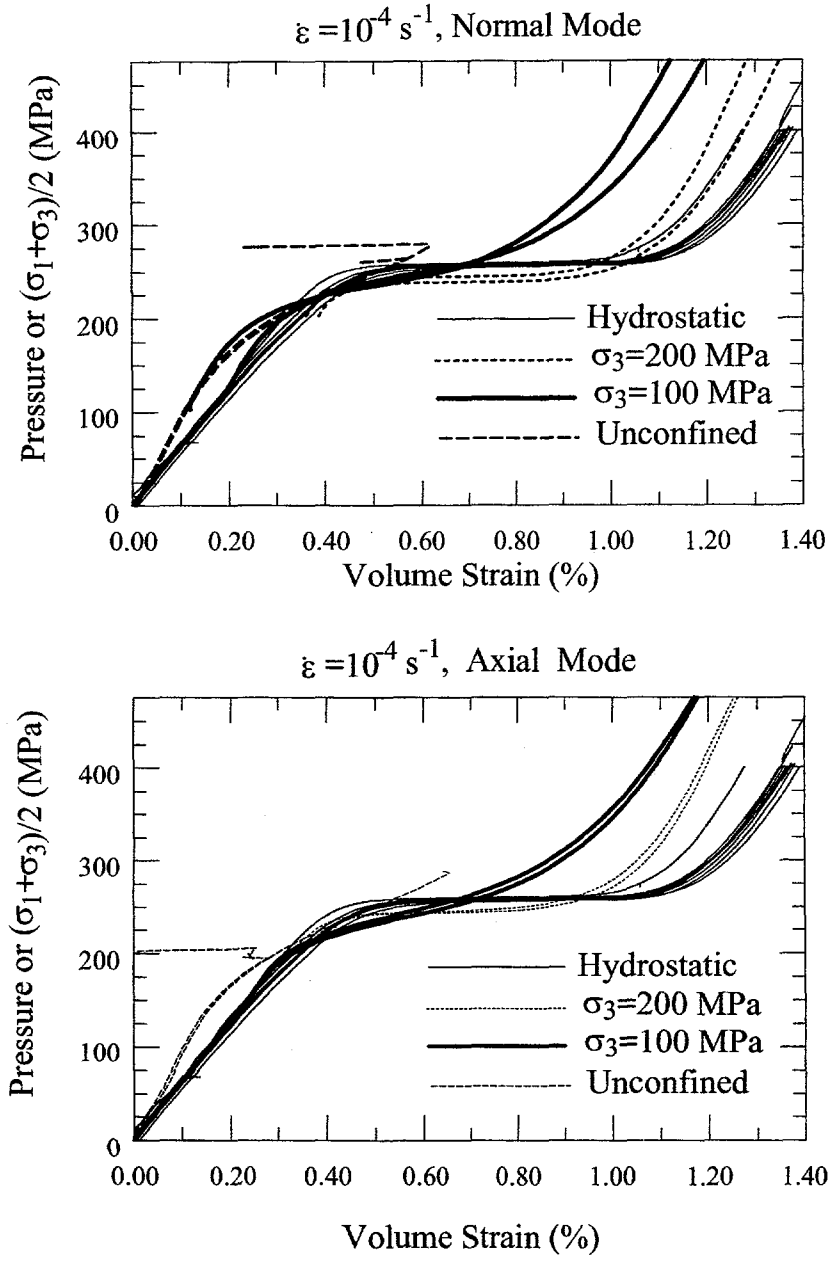

Figure 3.30: Plots of $\frac{\sigma_1+\sigma_3}{2}$ *vs.* volume strain for normal-mode (top), and axial-mode (bottom) uniaxial and triaxial compression experiments at $\dot{\epsilon}=10^{-2}s^{-1}$ and confining pressures $\leq$200 MPa. Hydrostatic compression experiments are shown for comparison.

Chapter 4

Experimental Results: Confirmatory Experiments on Unpoled Ceramic

4.1 Uniaxial Compression Experiments: Strength and Elastic Properties

Two uniaxial compression experiments to failure were performed on unpoled 453 ceramic at a strain rate of 10^{-4} s^{-1} (Figures 4.1 and 4.2). We performed two unload/reload cycles at axial stresses below 100 MPa during each of the two uniaxial compression experiments. Stresses were deliberately kept low during the cycles in order to stay within the stability field of the ferroelectric, rhombohedral phase as indicated by the absence of permanent volumetric strain upon complete unloading. Detectable amounts of axial strain did remain, however, upon complete unloading (Figures 4.1 and 4.2), indicating that some dipole switching may have occurred.

Failure strengths, and Young's moduli and Poisson's ratios determined from the unload/reload cycles are summarized in Table 4.1. Shown for comparison in Tables 4.2 and 4.3 are failure strengths and elastic properties measured by Zeuch *et al.* [1997] in identical uniaxial compression experiments on unpoled hifire 541-1 and 424 ceramic. The former hifire, which had Avicel added as a pore former, was qualified voltage bar material with a density and porosity comparable to hifire 453; the latter ceramic was qualified current stack ceramic, which had no pore former added, and, hence, a comparatively lower porosity and higher density [Keck, 1990]. Compressive strengths and Young's modulus for hifire 453 (Table 4.1) are comparable to those for hifire 541- 1. Both compressive strengths and Young's modulus for

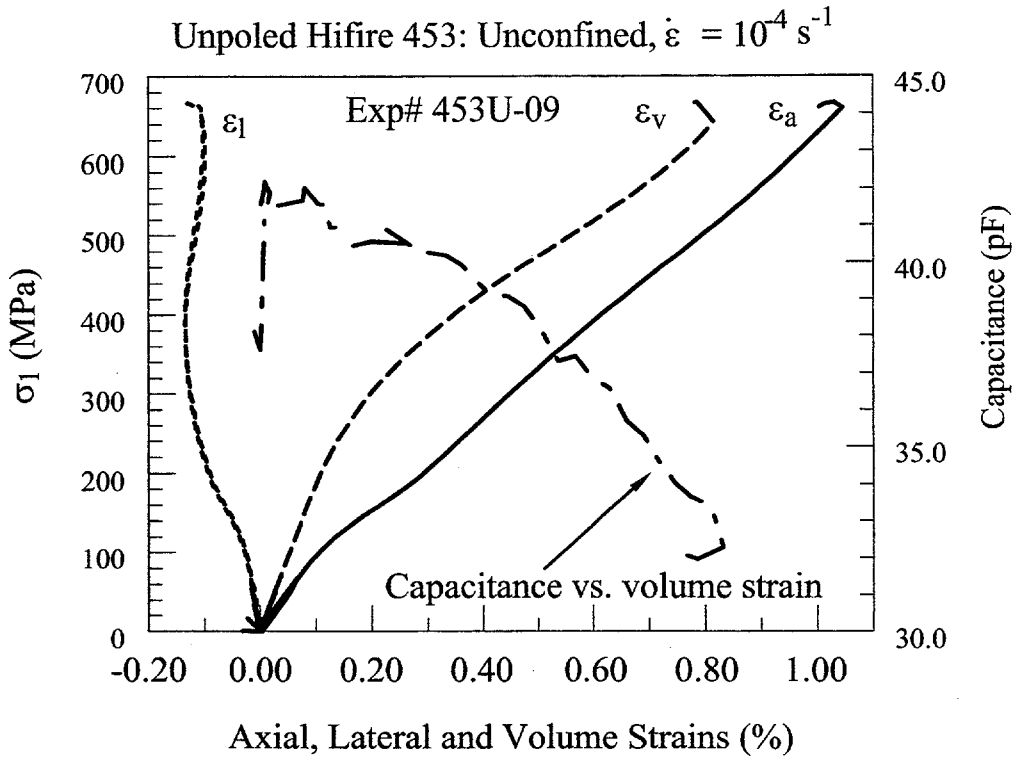

Figure 4.1: Uniaxial compression experiment at 10^{-4} s^{-1} on unpoled 453 ceramic. ϵ_a, ϵ_l and ϵ_v are the axial, lateral and volume strains, respectively. Capacitance is plotted *vs.* ϵ_v on the right abscissa.

the denser 424 ceramic are higher than those for the voltage bar ceramics 453 and 541- 1.

In the interest of completeness, stress-strain and capacitance data for the uniaxial compression experiments on unpoled, 541-1 and 424 ceramic, and poled 541-1 reported by Zeuch *et al.* [1997] are included in Appendices E, F and G, respectively. Additional information on these two hifires are given by Keck [1990] and Zeuch *et al.* [1992a, b].

Interestingly, the unconfined compressive strengths of the poled, normal- and axial-mode 453 ceramic specimens deformed at $\dot{\epsilon}$ =10^{-4} s^{-1} (Tables 3.1 and 3.2) are consistently lower, by 80 to 100 MPa, than those for the unpoled 453 specimens (Table 4.2). This was not something that was observed in two normal-mode, uniaxial compression experiments at 10^{-4} s^{-1} on poled hifire 541-1 ceramic, however [Zeuch *et al.*, 1997] (Appendix G). Those specimens failed at 651 and 668 MPa (Table 4.4), very comparable to results for unpoled

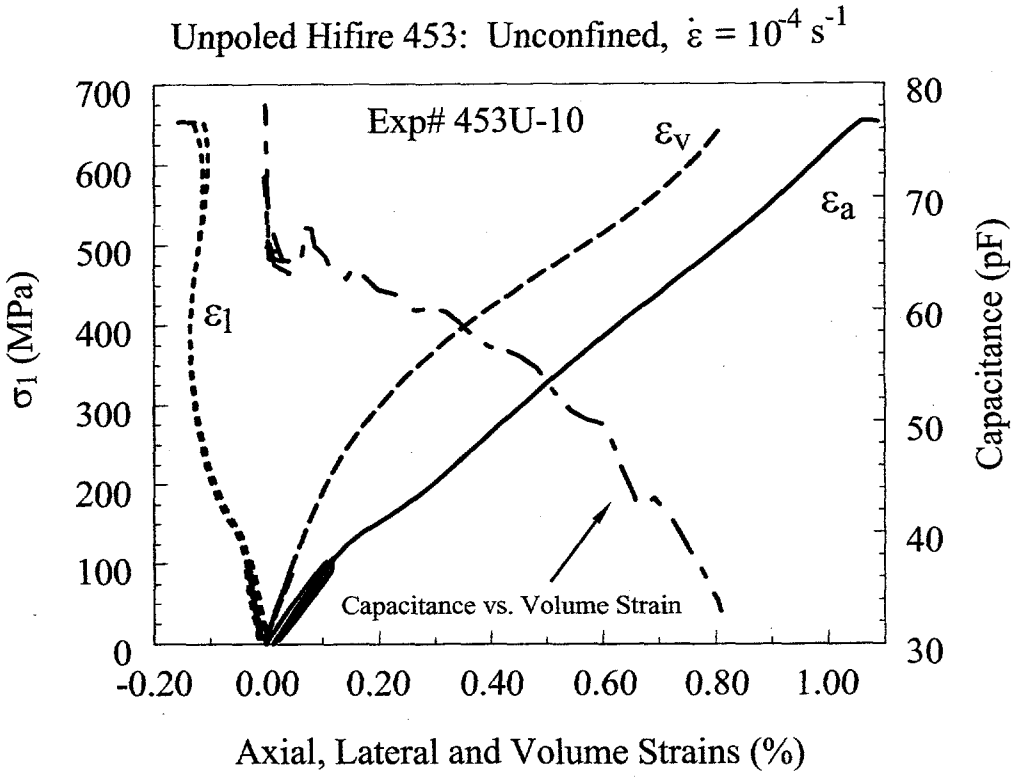

Figure 4.2: Uniaxial compression experiment at 10^{-4} s^{-1} on unpoled 453 ceramic. ϵ_a, ϵ_l and ϵ_v are the axial, lateral and volume strains, respectively. Capacitance is plotted *vs.* ϵ_v on the right abscissa.

541-1 ceramic (Table 4.2). These observations suggest that: (1) poling may introduce damage in the form of microcracks that serves to weaken the poled specimens [Lynch *et al.*, 1995], and (2) some hifires may be more susceptible to damage by poling than others.

Other than the low failure strengths of the poled 453 specimens, comparison of Figures 4.1 and 4.2 with those shown in Appendix E, and comparison of Figure 3.1 with those in Appendix G, indicates that unpoled and poled 453 ceramic behave essentially identically to unpoled and poled 541-1 ceramic, respectively. This includes the peculiar behavior of the capacitance during uniaxial compression of unpoled ceramic, which has been discussed at length elsewhere [Zeuch *et al.*, 1997; Zeuch *et al.*, in preparation].

Experiment ID	σ_1 at failure (MPa)	E (GPa)	ν
453U-09	666	104*	0.23*
453U-10	654	92*	0.26*

Table 4.1: Uniaxial compression experiments on unpoled, hifire 453 ceramic. Strain rate was $1.0 \times 10^{-4} s^{-1}$. Asterisk (*) indicates average of two unload/reload cycles.

Experiment ID	σ_1 at failure (MPa)	E (GPa)	ν
541-1-01	648	105*	0.23*
541-1-02	651	N/D	N/D
541-1-03	708	N/D	N/D
541-1-04	N/D	N/D	N/D
541-1-05	638	N/D	N/D

Table 4.2: Uniaxial compression experiments on unpoled, hifire 541-1 ceramic. Strain rate was $1.0 \times 10^{-4} s^{-1}$ [Zeuch *et al.*, 1997]. Asterisk (*) indicates average of two unload/reload cycles. N/D: not determined.

4.2 Hydrostatic Compression and Constant-Stress-Difference Experiments

Mean stress-volume strain data from the two hydrostatic compression and six CSD experiments on unpoled ceramic are summarized in Figure 4.3. Also included on the figure are data from the two uniaxial compression experiments discussed in the foregoing section.

These results are qualitatively identical to those from earlier test series on unpoled 424, 541-1 and 435 ceramic [Zeuch *et al.*, 1992a,b; in preparation]. At a constant pressurization rate, increasing shear stress lowers the mean stress for onset of the transformation, and increases the time required to complete the reaction.

Quantitatively, however, an applied stress difference of 50 MPa has no detectable effect on the transformation compared to the hydrostatic condition (Figure 4.3), unlike our earlier results for hifire 424 [Zeuch *et al.*, 1992a,b]. Furthermore, a stress difference of 150 MPa clearly has begun to trigger the transformation as indicated by the small, but reproducible discontinuities in the mean stress-volume strain plots for the experiments at $\sigma_1 - \sigma_3$=150 MPa, indicated by the small arrow on Figure 4.3. Note, however, that the reaction stops until the mean stress begins to increase. This is consistent

Experiment ID	σ_1 at failure (MPa)	E (GPa)	ν
424-01	792	120*	0.23*
424-02	872	N/D	N/D
424-04	479	N/D	N/D
424-05	803	N/D	N/D
424-06	N/D	N/D	N/D
424-07	839	N/D	N/D

Table 4.3: Uniaxial compression experiments on unpoled, hifire 424 ceramic. Strain rate was $1.0 \times 10^{-4} s^{-1}$ [Zeuch *et al.*, 1997]. Asterisk (*) indicates average of two unload/reload cycles. N/D: not determined.

Experiment ID	σ_1 at failure (MPa)
541-1-07	661
541-1-08	668

Table 4.4: Normal-mode, uniaxial compression experiments on poled, hifire 541-1 ceramic. Strain rate was $1.0 \times 10^{-4} s^{-1}$ [Zeuch *et al.*, 1997].

with our orientation-dependent model for onset of the transformation under nonhydrostatic stress [Zeuch *et al.*, in preparation].

Capacitance data were collected during the hydrostatic compression and CSD experiments (Figure 4.4-4.7). Qualitatively and quantitatively, these results are identical to those obtained earlier for unpoled hifire 424 ceramic, and quite different from those obtained for 541-1 ceramic [Zeuch *et al.*, 1992a,b]. In hydrostatic compression (Figure 4.4) the capacitance increases slightly with increasing pressure until onset of the transformation, at which point the capacitance drops precipitously. Under CSD conditions, the capacitance drops during deviatoric loading (Figures 4.5-4.7), and then increases gradually with increasing mean stress until onset of the transformation. At the transformation, the capacitance again drops dramatically. Overall drops upon transformation are comparable in magnitude to those for hifire 424.

As we did for our test series on unpoled hifire 424 ceramic [Zeuch *et al.*, 1994], we have examined the volume strain and peak capacitance data in terms of σ_1 as well as mean stress. The objective here, of course, is to identify some invariant criterion for onset of the transformation under nonhydrostatic stress. The results shown in Figure 4.3 clearly indicate that the mean stress is *not* the critical parameter, or the volume strain anomalies would all begin

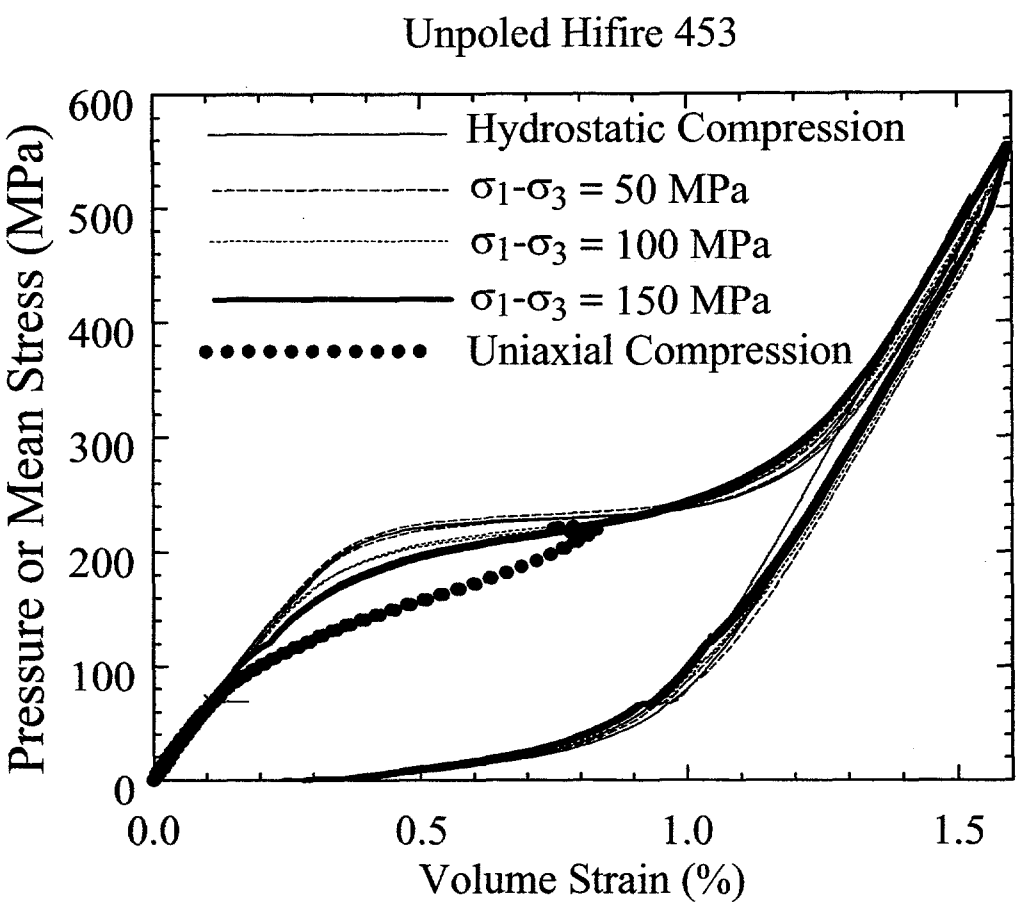

Figure 4.3: Plot of mean stress or pressure *vs.* volume strain for hydrostatic and uniaxial compression, and constant-stress-difference experiments on unpoled, hifire 453 ceramic.

at the same value of σ_m. Zeuch *et al.* [1994] showed, using volume strain and capacitance data, and friction-corrected values for σ_1 that the transformation of unpoled ceramic under nonhydrostatic stress began when σ_1 equalled the hydrostatic pressure at which the transformation otherwise occurred.

Some of the experiments shown in Figure 4.3 are replotted in terms of σ_1 *vs.* volume strain in Figure 4.8; we have excluded the experiments performed at $\sigma_1 - \sigma_3$=150 MPa, because these have demonstrably begun to transform upon full deviatoric loading. If we take onset of the transformation as the first (estimated) departure of the data from linearity, and recall that the values for σ_1 have not been corrected for friction (that is, they are too high by an estimated 12 to 15 MPa), it is *possible*, though far from convincing,

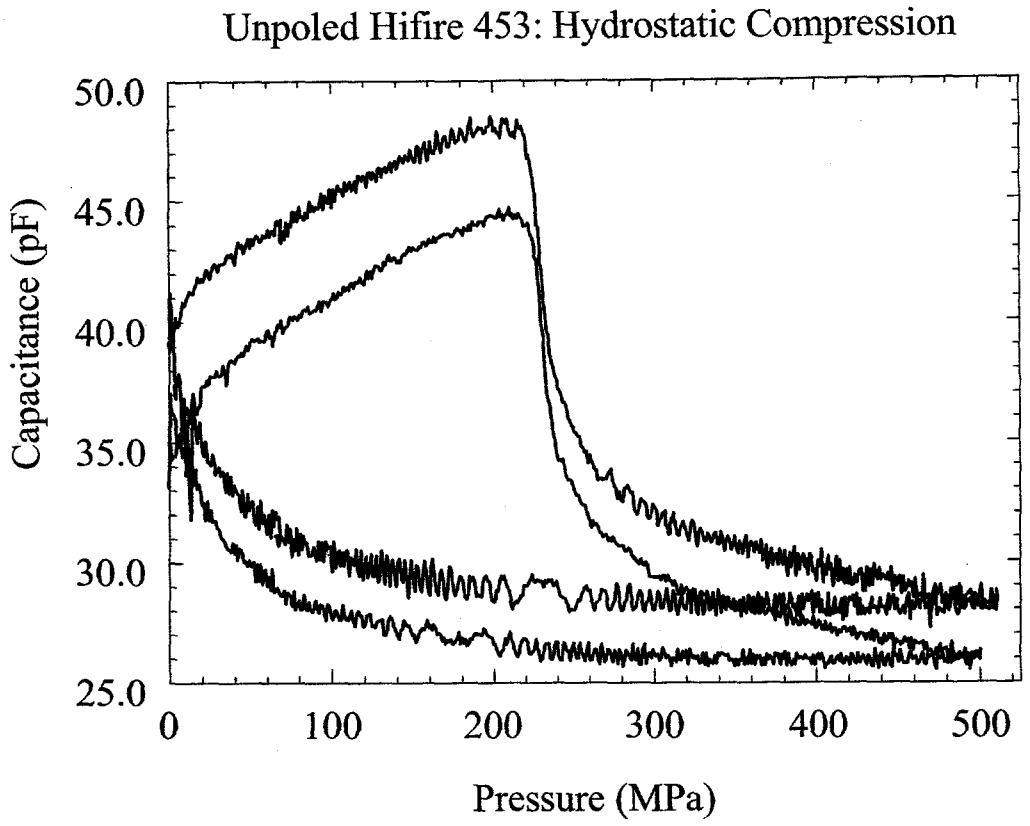

Figure 4.4: Plot of capacitance *vs.* pressure for hydrostatic compression experiments on unpoled 453 ceramic.

that the transformation begins when σ_1 equals the hydrostatic pressure for transformation.

Zeuch *et al.* [1994] showed that there was an excellent correlation between the peak capacitance reached in the hydrostatic compression and CSD experiments, and onset of the transformation as indicated by the volume strain anomaly, Unlike onset as indicated by volume strain, however, the peak capacitance could be unambiguously identified.

As we did earlier [Zeuch *et al.*, 1994], we identified the peak capacitance for each hydrostatic compression and CSD experiment. We then identified the corresponding values for the confining pressure and σ_1. Using the results from the friction loops conducted in the earlier triaxial compression experiments on poled ceramic, we estimated the friction correction to each CSD experiment, recalculating σ_1 and the mean stress corresponding to each value of the peak capacitance. In Figure 4.9, we plot the peak capacitances

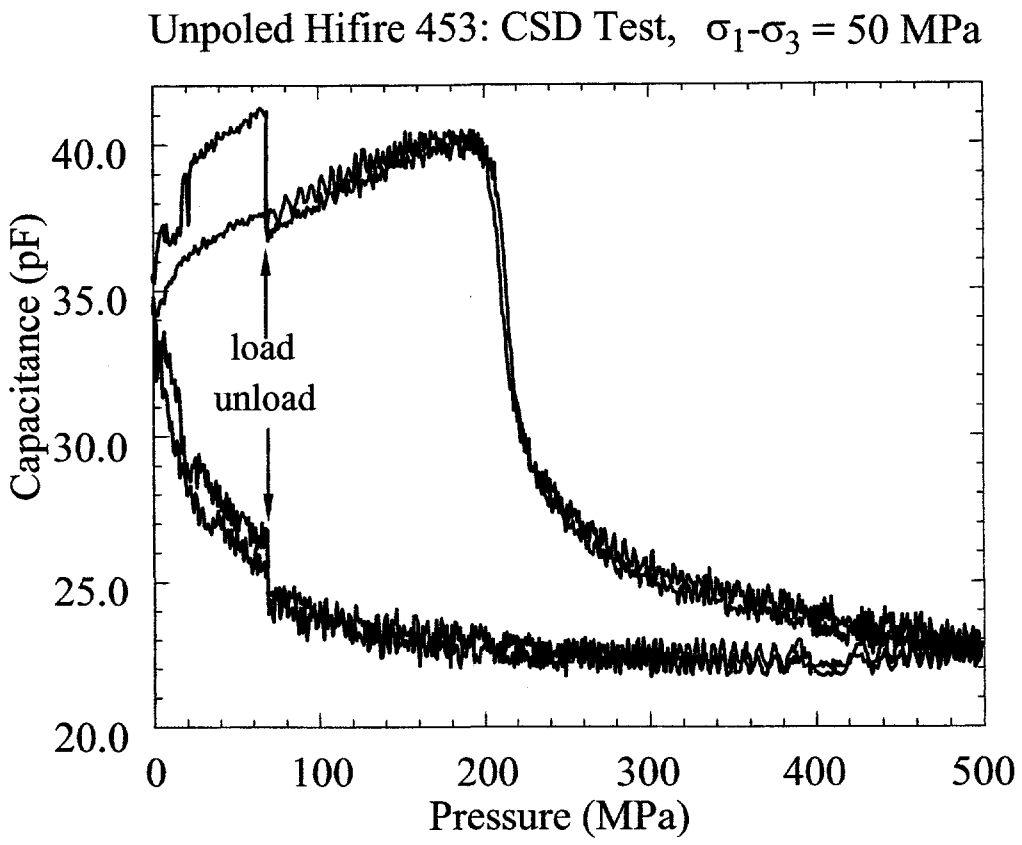

Figure 4.5: Plot of capacitance *vs.* mean stress for constant-stress-difference experiments on unpoled 453 ceramic at $\sigma_1 - \sigma_3$=50 MPa.

for the CSD experiments *vs.* corrected mean stress and σ_1. Again, we have excluded the experiments conducted at $\sigma_1 - \sigma_3$=150 MPa, because these have demonstrably begun to transform upon deviatoric loading.

Unlike our results for highfire 424, it is impossible to conclude that the transformation begins when σ_1 equals the hydrostatic pressure for transformation. In fact, peak capacitance actually seems to correlate better with the mean stress than with σ_1 in this instance. We have no explanation for this discrepancy with our earlier observations, except to note that, perhaps owing to the greater porosity, the onset of the transformation is much more difficult to "pick" for hifire 453 than for 424. Examination of the pressure-volume strain plots for the hydrostatic compression experiments on unpoled 453 ceramic indicate that the plots first depart from linearity well below 200 MPa, perhaps as low as 175 MPa (Figure 4.3). However, the peak capacitances would suggest an onset of the transformation that is in the range of

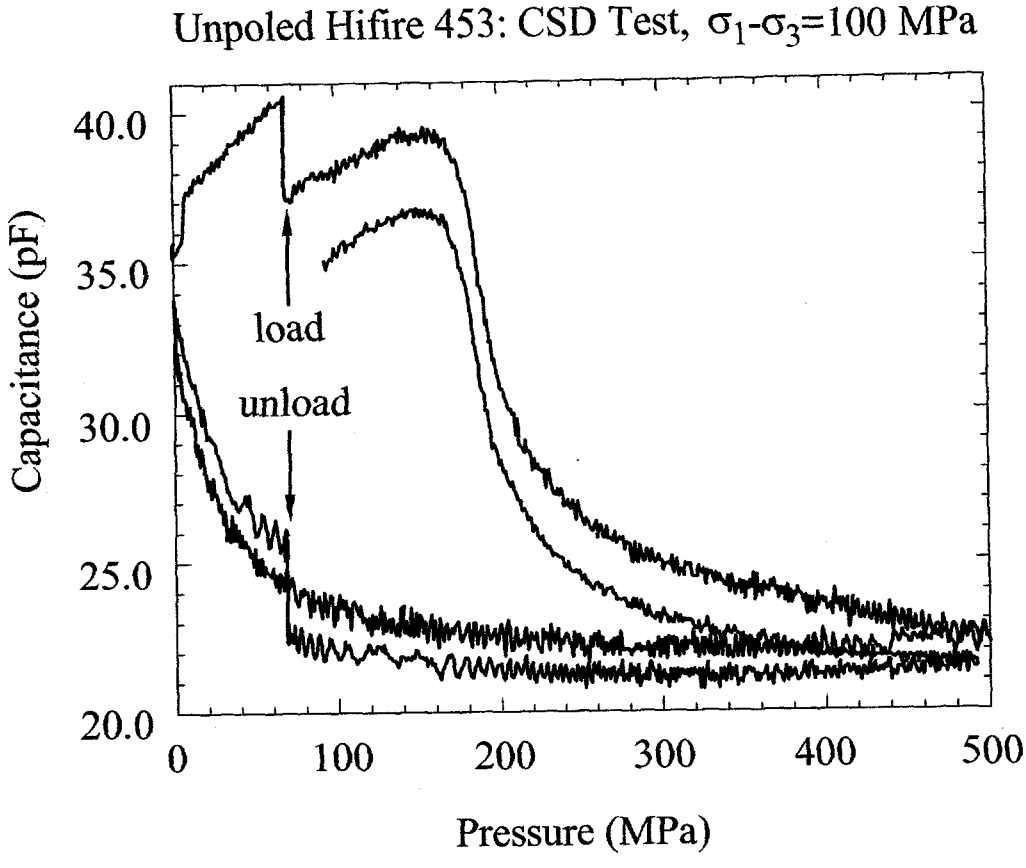

Figure 4.6: Plot of capacitance *vs.* mean stress for constant-stress-difference experiments on unpoled 453 ceramic at $\sigma_1 - \sigma_3$=100 MPa.

198-209 MPa. This is a substantial spread in pressures, compared with the good correlation between the volume strain and capacitance anomalies for hydrostatic compression of hifire 424 ceramic [Zeuch *et al.*, 1994].

Alternatively, it is possible that our correction for friction is faulty, although this seems unlikely.

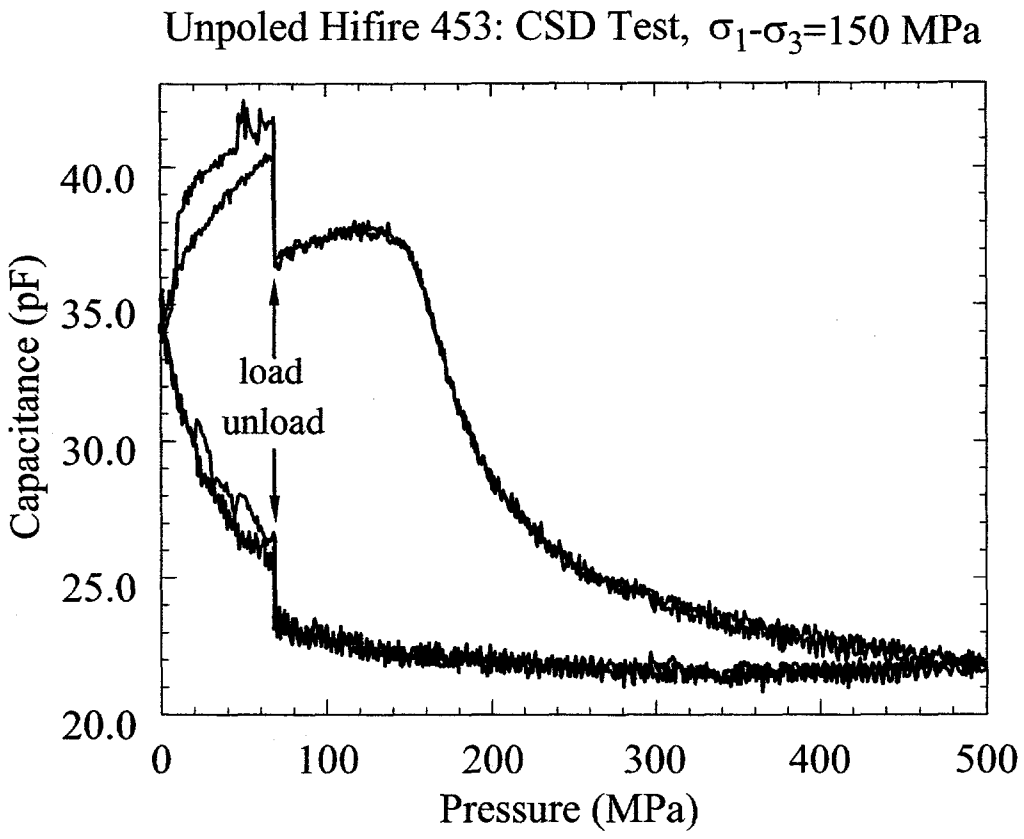

Figure 4.7: Plot of capacitance *vs.* mean stress for constant-stress-difference experiments on unpoled 453 ceramic at $\sigma_1 - \sigma_3$=150 MPa.

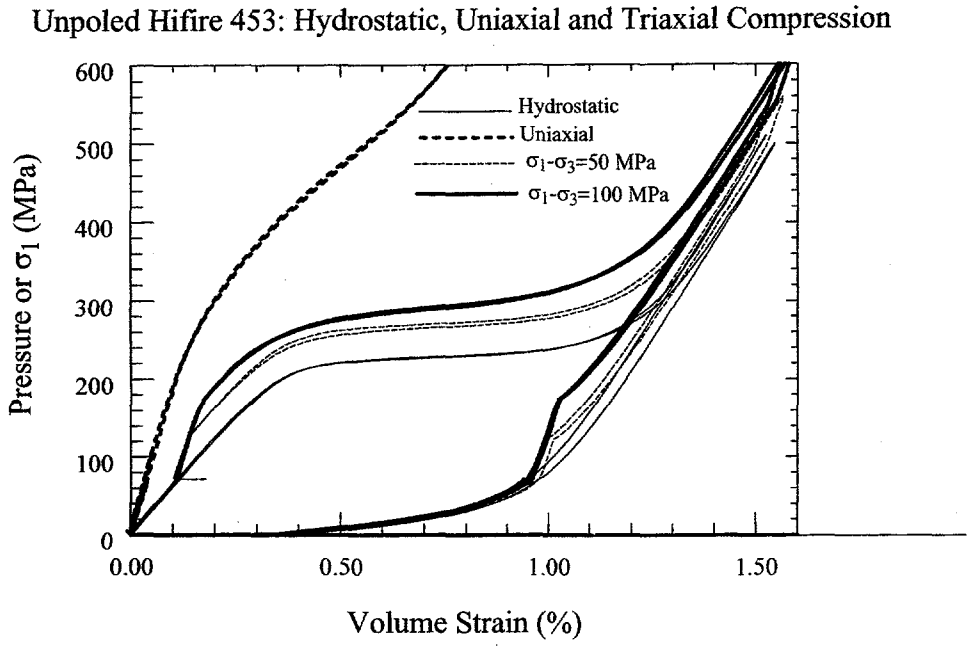

Figure 4.8: Plots of pressure or σ_1 *vs.* volume strain for selected uniaxial and hydrostatic compression, and constant-stress-difference experiments on hifire 453 ceramic.

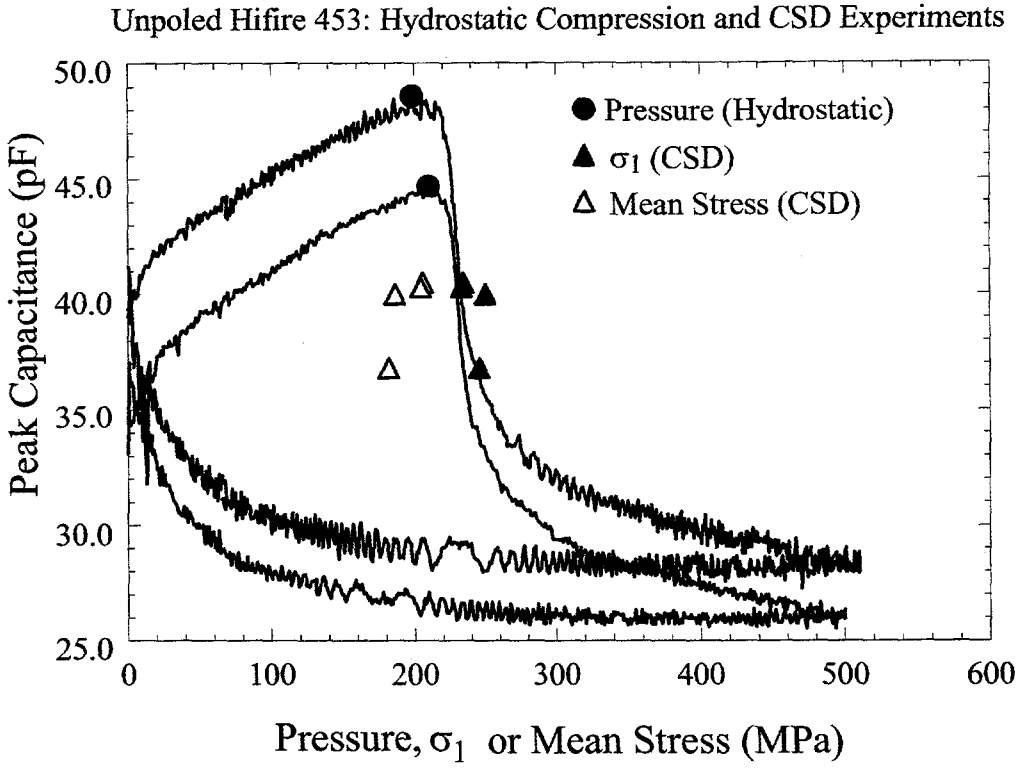

Figure 4.9: Plot of peak capacitance *vs.* pressure, or corrected values of σ_1 or mean stress. See text for explanation.

Chapter 5

Discussion and Conclusions

We have conducted a series of uniaxial and triaxial compression experiments on poled PZT 95/5-2Nb ceramic. All test specimens were fabricated from a single, qualified Sandia voltage bar hifire, 453. Specimens were poled both transverse (normal- mode) and parallel (axial-mode) to the axis of compression. The strain rate was either 1×10^{-2} or 1×10^{-4} s^{-1}, and confining pressures were 0.1 (unconfined), 100, 200, 400 or 800 MPa. Owing to a shortage of electrical feedthroughs, poling electrodes were shorted together, and capacitance measurements were not performed.

Strength of the ceramic increased with both strain rate and confining pressure. Ductility also increased with confining pressures. With increasing confinement, several transitions in fracture mechanism were observed. Under unconfined conditions, failure occurred by violent, axial splitting. At 100 MPa, failure occurred along a single shear fracture. At 200 and 400 MPa, failure occurred by increasingly distributed microfracturing. At 400 MPa, the first indications of pore collapse were detected, in the form of a brief period of enhanced, nonlinear, volumetric compaction. However, this brief period of compaction was unstable: compressive volume strain rapidly gave way to the same dilation observed at lower confining pressures. At 800 MPa, however, compaction continued out to axial strains of about 5%, when the experiments were terminated. Differences in strengths between specimens deformed at pressures of 400 and 800 MPa appeared to be minimal. However, if deformation had continued, the specimens deformed at 800 MPa might be expected to experience a second hardening phase once all pore space is eliminated.

No significant differences in strength or ductility were associated with the two different poling orientations. However, both normal- and axial-mode specimens deformed in uniaxial compression were weaker than two unpoled hifire 453 specimens that were tested under identical conditions. This sug-

gests that poling may introduce some form of damage, possibly microcracks, that weakens poled specimens. Experience with a previous voltage bar hifire, 541-1, further suggests that some hifires may be more susceptible to poling damage than others.

Clear evidence for onset of the FE-AFE transformation was observed in the triaxial compression experiments on poled ceramic that were performed at confining pressures at about 200 MPa. Hydrostatic transformation pressure for the poled specimens appeared to begin at about 200 MPa and be complete by about 250 MPa. Thus, experiments conducted at pressures of 400 and 800 MPa had already passed through the transformation during hydrostatic pressurization, so no peculiarities of the stress-strain curves associated with the transformation were observed in these experiments.

Probably owing to a higher porosity, even under hydrostatic conditions the transformation was spread out over a relatively large range of pressures compared to ceramic from other hifires that we have examined [Zeuch *et al.*, 1995]. The specimens that transformed under triaxial conditions exhibited the same depression of the mean stress for onset of the transition that we have observed earlier. Similarly, the values of σ_1 at onset of the transformation appear to be higher than the hydrostatic pressure for transformation of poled ceramic [Zeuch *et al.*, 1995].

Although axial and lateral strains for the normal- and axial-mode specimens were different both before and after onset of the transformation under deviatoric loading, surprisingly, volume strains were not. This indicated that the transformation was starting at the same stress for either normal-mode or axial-mode deformation. This was something of a surprise, because Zeuch *et al.* [in preparation] have recently proposed that under nonhydrostatic loading, transformation occurs when the magnitude of the principal compressive stress on some particular crystallographic surface(s) reaches the pressure for transformation. Thus, transformation depends not only on the magnitude of the stress, but its orientation relative to the poling direction. The differently-poled specimens should have transformed at different stresses, owing to differing preferred crystallographic orientations relative to the applied stress.

We suggest that during axial-mode deformation, deviatoric loading rapidly re-orients many of the dipoles perpendicular to the compression axis well before the stress necessary to trigger the transformation is reached. Thus, the preferred crystallographic orientations of the two types of specimens are essentially identical by the time the transformation can start, so the two types of specimens exhibit identical behavior at and beyond onset of the transformation. We base this hypothesis on the observation that the axial strain responses of the two types of specimens are very different at low stresses, but become identical well below σ_1=200 MPa. We plan to test this hypoth-

esis in the near future. If this hypothesis is true, it suggests that poling somehow eases or "preconditions" subsequent stress-induced dipole switching. We suggest this because the axial strain response of *unpoled*, uniaxially compressed specimens never becomes identical to poled specimens deformed in the normal mode. This indicates that the unpoled specimens cannot switch as readily as the poled, axial-mode specimens, whose axial strain behavior *does* approach that of the normal mode specimens.

Interestingly, the higher the confining pressure at which the triaxial compression experiment was run, the more rapidly the transformation was completed once it started. This confirms our earlier assertion [Zeuch *et al.*, in preparation] that there is a critical mean stress for completion of the transformation: the higher the confining pressure at which the experiment is run, the more rapidly the critical mean stress would be reached, even at the same pressurization rate.

Finally, we conducted a series of hydrostatic and uniaxial compression, and constant-stress-difference experiments on unpoled hifire 453 ceramic to ensure that its behavior is similar to other hifires that we have investigated in the past. Under hydrostatic conditions, the unpoled ceramic begins to transform at a pressure of about 175 MPa, and is complete by about 225 MPa. Thus, as should be the case, the poled ceramic transforms at a higher pressure [Berlincourt *et al.*, 1964; Zeuch *et al.*, 1995].

In CSD experiments, unpoled hifire 453 ceramic exhibits behavior consistent with our earlier experience with other hifires. Increasing shear stress depresses the mean stress for onset of the transformation, and increases the amount of time required to complete it. However, 453 ceramic is less sensitive to shear stress than earlier hifires: an applied stress difference of 50 MPa had no detectable effect on the transformation, unlike our earlier experience with hifire 424 ceramic. And an applied stress difference of 150 MPa had clearly begun to trigger the transformation, again unlike our prior experience with hifires 424 and 541-1.

Using capacitance data and friction-corrected values for σ_1 and the mean stress, we attempted to correlate onset of the transformation with one or the other of the two criteria. Unlike our earlier results [Zeuch *et al.*, 1994], onset of the transformation actually appeared to correlate better with the mean stress. That is, the transformation appeared to begin when the mean stress equalled the pressure for transformation under hydrostatic conditions. This result is puzzling, in view of the clear depression of the mean stress for onset of the transformation when using the volume strain as the indicator. The source of this discrepancy is unclear, but may relate to the much blurrier character of the transformation of 453 ceramic, whether capacitance or volume strain is used as the criterion for occurrence.

The issue of developing a criterion for onset of the transformation under nonhydrostatic stress is an important one for the purposes of modeling the operation of neutron generator power supplies. Zeuch *et al.* [in preparation], Montgomery and Zeuch [1998], Horie *et al.* [in preparation] have, together, developed a preliminary model for onset of the transformation that relates maximum compressive stress to poling direction. The model explains many observations in both our quasistatic experiments and recent shock wave experiments on poled and unpoled ceramic.

Though many of the results that we have presented here for poled and unpoled hifire 453 ceramic are consistent with that model, other results, particularly for unpoled ceramic, are equivocal if not entirely contradictory. These issues should be investigated further. In view of the fact that our clearest observations have been obtained from a hifire into which no additional porosity was introduced, 424, perhaps future investigation should focus on newly-fabricated hifires that do not have the complication of added porosity. Investigation along these lines might have the added benefit of finally allowing us to understand why voltage bar ceramic must have added porosity in order to work successfully in functional test units [Storz and Dungan, 1985].

In any event, minor differences between every hifire of PZT 95/5-2Nb is well documented. The uniaxial compressive strength of unpoled 453 ceramic is consistent with our earlier results, and elastic properties are also similar. Thus, at this time there is no reason to believe that 453 ceramic is substantially different from any other voltage bar material, and that the failure surfaces that we have determined are anything other than representative. This should certainly be checked as new hifires are characterized in the future, but it is a reasonable assumption at this time for the purposes of modeling.

Chapter 6

References

Bauer, F., K. Vollrath, Y. Fetiveau and L. Eyraud [1976]. *Ferroelectric ceramics: application to mechanical energy conversion under shock compression.* Ferroelectrics, **10**:61-64.

Berlincourt, D., H. H. A. Krueger and B. Jaffe [1964]. *Stability of phases in modified lead zirconate with variation in pressure, electric field, temperature and composition.* J. Phys. Chem. Solids, **25**:659-674.

Chhabildas, L. C. [1984]. *Dynamic Shock Studies of PZT 95/5 Ferroelectric Ceramic.* Rept. No. SAND84-1729, Sandia National Laboratories, Albuquerque, NM, 31pp.

Chhabildas, L. C., M. J. Carr, S. C. Kunz and B. Morosin [1986]. *Shock-recovery experiments on PZT 95/5.* In: Gupta, Y. M. (ed.), *Shock Waves in Condensed Matter,* pp. 785-790. Plenum, New York, 954pp.

Dungan, R. H., and L. J. Storz [1985]. *Relation between chemical, mechanical and electrical properties of Nb_2O_5-modified 95 mol% $PbZrO_3$ 5-mol% $PbTiO_3$.* J. Amer. Ceram. Soc., **68**:530-533.

Fritz, I. J. [1978]. *Uniaxial stress effects in a 95/5 lead zirconate titanate ceramic.* J. Appl. Phys., **49**: 4922-4928.

Fritz, I. J. [1979]. *Stress effects in two modified lead zirconate titanate ferroelectric ceramics.* J. Appl. Phys., **50**:5265-5271.

Fritz, I. J., and J. D. Keck [1978]. *Pressure-temperature phase diagrams for several modified lead zirconate ceramics.* J. Phys. Chem. Solids, **39**:1163-1167.

Hallam, S. D., and M. F. Ashby [1990]. *Compressive brittle fracture and the construction of multi-axial failure maps.* In: Barber, D. J., and P. G. Meredith (Eds), *Deformation Processes in Ceramics, Minerals and Rocks,* pp.84-108, Unwin- Hyman, London, 1990. 423pp.

Hardy, R. D. [1993]. *Event Triggered Data Acquisition in the Rock Mechanics Laboratory.* Rept. No. SAND93-0256, Sandia National Laboratories, Albuquerque, NM, 120pp.

Hardy, R. D., 1997. *Event Triggered Data Acquisition in the Rock Mechanics Laboratory: Upgrades and Revisions.* Rept. No. SAND97-0950, Sandia National Laboratories, Albuquerque, NM, 25pp.

Haun, M. J., E. Furman, S. J. Jang and L. E. Cross [1989]. *Thermodynamic theory of the lead-zirconate-titanate solid solution system, part I: phenomenology.* Ferroelectrics, **99**:13-25.

Keck, J. D. [1990]. *Comments on a Memo from R. H. Moore to F. P. Gerstle, Jr., 7476, dtd March 29, 1990. Subject: Comments Regarding SNL Memo "Laboratory Characterization of Ferroelectric Ceramics," by W. R. Wawersik and D. H. Zeuch, 6232, 2/6/90."* Internal memorandum to J. A. Wilder, 2565, 18 April 1990. Sandia National Laboratories, Albuquerque, NM. 2pp.

Lankford, J. [1981]. *The role of tensile microfracture in the strain rate dependence of compressive strength of fine- grained limestone–analogy with strong ceramics.* Int. J. Rock Mech. Min. Sci. & Geomech. Abstr., **18**:173-175.

Lynch, C. S., W. Yang, L. Collier, Z. Suo and R. M. McMeeking [1995]. *Electric field induced cracking in ferroelectric ceramics.* Ferroelectrics, **166**:11-30.

Lysne, P. C., and C. M. Percival [1975]. *Electric energy generation by shock compression of ferroelectric ceramics: normal-mode response*

of PZT 95/5. J. Appl. Phys., **46**:1519-1525.

Meredith, P. G. [1990]. *Fracture and failure of brittle polycrystals: an overview.* In: Barber, D. J., and P. G. Meredith (Eds), *Deformation Processes in Ceramics, Minerals and Rocks,* pp.5-47, Unwin-Hyman, London, 1990. 423pp.

Montgomery, S. T. [1986]. *Analysis of transitions between ferroelectric and antiferroelectric states under conditions of uniaxial strain.* In: Gupta, Y. M., (ed), *Shock Waves in Condensed Matter*, pp.179-184, Plenum, New York, 954pp.

Newnham, R. E. [1989]. *Structure-property relationships in perovskite electroceramics.* In: Navrotsky, A., and D. J. Weidner (Eds), *Perovskite: A Structure of Great Interest to Geophysics and Materials Science*, pp.91-98, American Geophysical Union, Washington, D.C.

Olsson, W. A. [1991]. *The compressive strength of tuff as a function of strain rate from 10^{-6} to 10^{3} s^{-1}.* Int. J. Rock Mech. Min. Sci. & Geomech. Abstr., **28**:115-118.

Paterson, M. S. [1978]. *Experimental Rock Deformation: the Brittle Field.* Springer–Verlag, New York, 1978. 254pp.

Poirier, J.-P. [1982]. *On transformation plasticity.* J. Geophys. Res., **87**:6791-6797.

Storz, L. J., and R. H. Dungan [1985]. *A Study of the Electrical, Mechanical, and Microstructural Properties of 95/5 PZT as a Function of Pore Former Type and Concentration.* Rept. No. SAND85-1612, Sandia National Laboratories, Albuquerque, NM. 24pp.

Wong, T.-f, H. Szeto and J. Zhang [1992]. *Effect of loading path and porosity on the failure mode of porous rocks.* In: Li, V. C. (Ed), *Micromechanical Modelling of Quasi-Brittle Materials Behavior,* pp. 281-294, American Society of Mechanical Engineers, New York.

Zeuch, D. H., S. T. Montgomery, J. D. Keck and D. J. Zimmerer [1992a]. *Hydrostatic and Triaxial Compression Experiments on Unpoled PZT 95/5-*

2Nb Ceramic: The Effects of Shear Stress on the $F_{R1} \rightarrow A_O$ Polymorphic Phase Transformation. Report No. SAND92-0484, Sandia National Laboratories, Albuquerque, NM, 164pp.

Zeuch, D. H., S. T. Montgomery and J. D. Keck [1992b]. *Hydrostatic and triaxial compression experiments on unpoled PZT 95/5-2Nb ceramic: the effects of shear stress on the $F_{R1} \rightarrow A_O$ polymorphic phase transformation.* J. Mater. Res., **7**:3314-3332.

Zeuch, D. H., S. T. Montgomery and J. D. Keck [1994]. *Further observations on the effects of nonhydrostatic compression on the $F_{R1} \rightarrow A_O$ polymorphic phase transformation in niobium-doped, lead-zirconate-titanate ceramic.* J. Mater. Res., **9**:1322-1327.

Zeuch, D. H., S. T. Montgomery and D. J. Zimmerer [1995]. *The Effects of Nonhydrostatic Compression and Applied Electric Field on the Electromechanical Behavior of Poled PZT 95/5-2Nb Ceramic During the $F_{R1} \rightarrow A_O$ Polymorphic Phase Transformation.* Rept. No. SAND 95-1951, Sandia National Laboratories, Albuquerque, NM, 114pp.

Zeuch, D. H., J. M Grazier and D. J. Holcomb [1997]. *Compressive strength and polymorphic transformation effects during uniaxial and triaxial compression of unpoled and poled PZT 95/5-2Nb.* Internal memorandum to S. T. Montgomery, 1567, 15 May 1997. Sandia National Laboratories, Albuquerque, NM, 33pp.

Zeuch, D. H., S. T. Montgomery, D. J. Holcomb, J. M. Grazier, and L. W. Carlson [in preparation]. *Uniaxial Compression Experiments on PZT 95/5-2Nb Ceramic: Evidence for an Orientation-Dependent " Maximum Compressive Stress" Criterion for Onset of the $F_{R1} \rightarrow A_O$ Polymorphic Phase Transformation.* Rept. No. –TBD–, Sandia National Laboratories, Albuquerque, NM.

Appendix A

Hifire 453: Normal–Mode Experiments at $\dot{\epsilon}$=10^{-4} s^{-1}

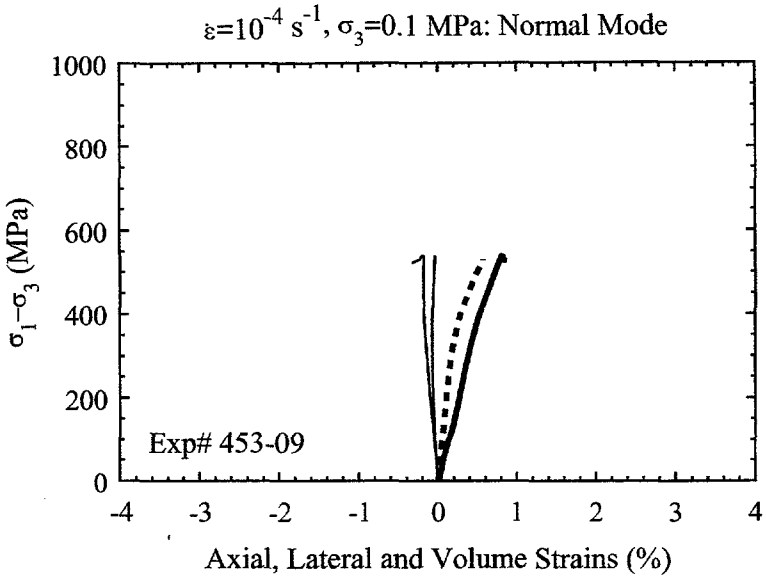

Figure A.1: Coarse solid line: axial strain. Fine solid lines: lateral strains. Dashed line: Volume strain. Normal–mode, unconfined, $\dot{\epsilon}$=10^{-4} s^{-1}.

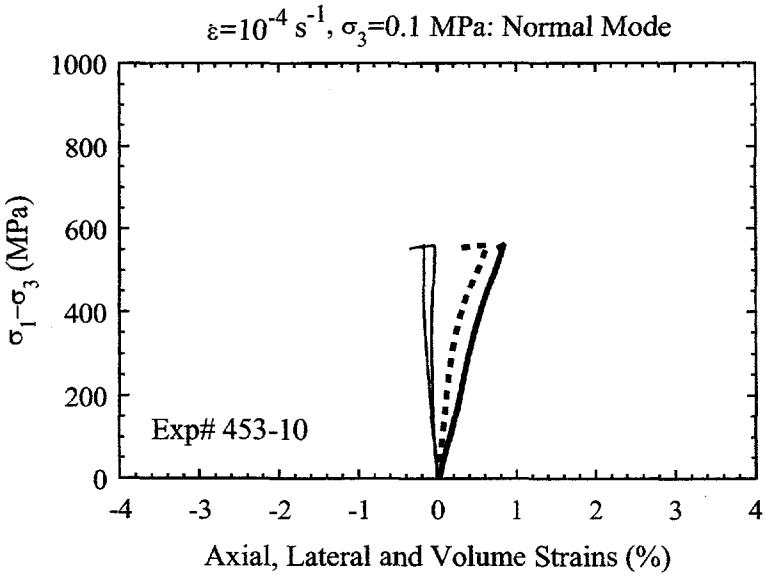

Figure A.2: Coarse solid line: axial strain. Fine solid lines: lateral strains. Dashed line: Volume strain. Normal–mode, unconfined, $\dot{\epsilon}$=10^{-4} s^{-1}.

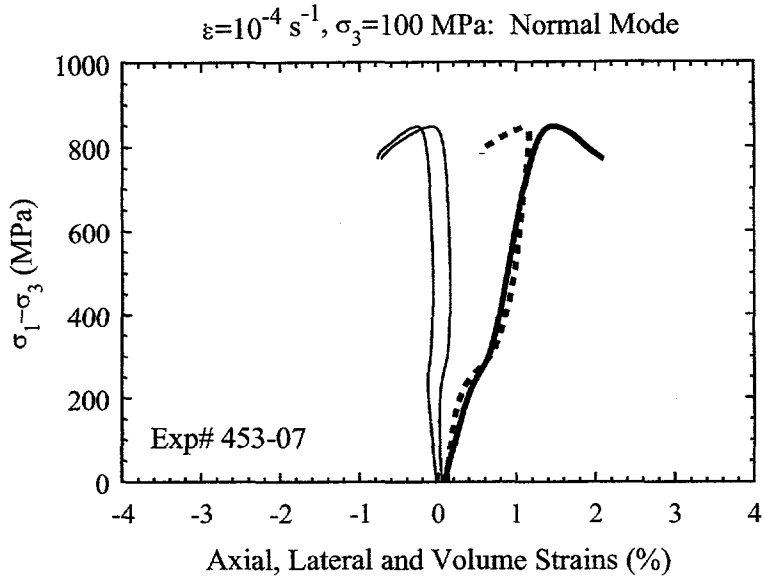

Figure A.3: Coarse solid line: axial strain. Fine solid lines: lateral strains. Dashed line: Volume strain. Normal–mode, σ_3 =100 MPa, $\dot{\epsilon}$=10^{-4} s^{-1}.

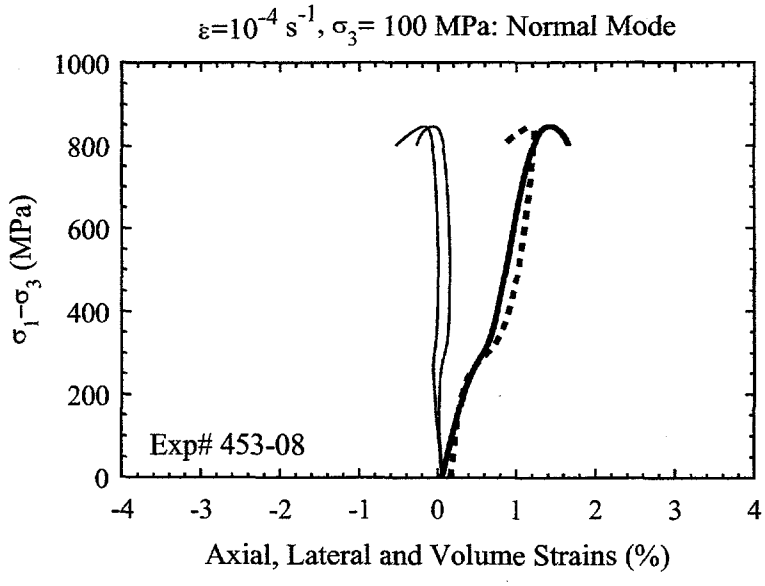

Figure A.4: Coarse solid line: axial strain. Fine solid lines: lateral strains. Dashed line: Volume strain. Normal–mode, σ_3 =100 MPa, $\dot{\epsilon}$=10^{-4} s^{-1}.

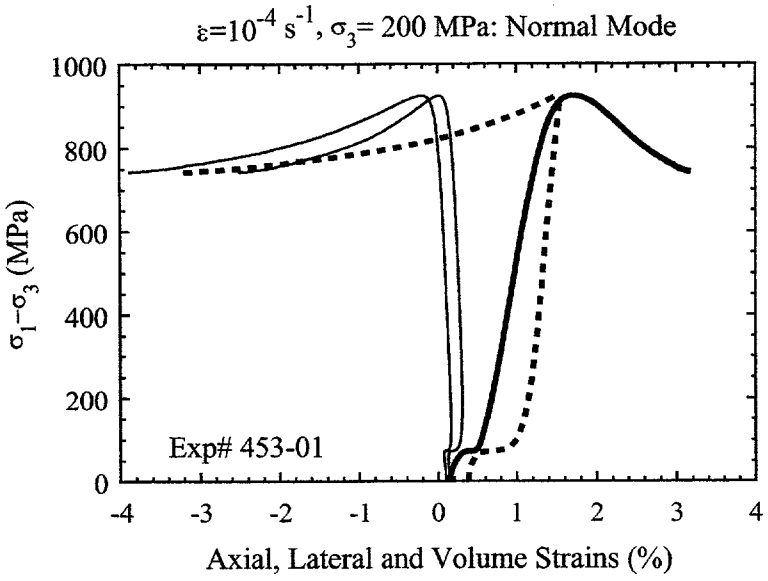

Figure A.5: Coarse solid line: axial strain. Fine solid lines: lateral strains. Dashed line: Volume strain. Normal–mode, σ_3 =200 MPa, $\dot{\epsilon}$=10^{-4} s^{-1}.

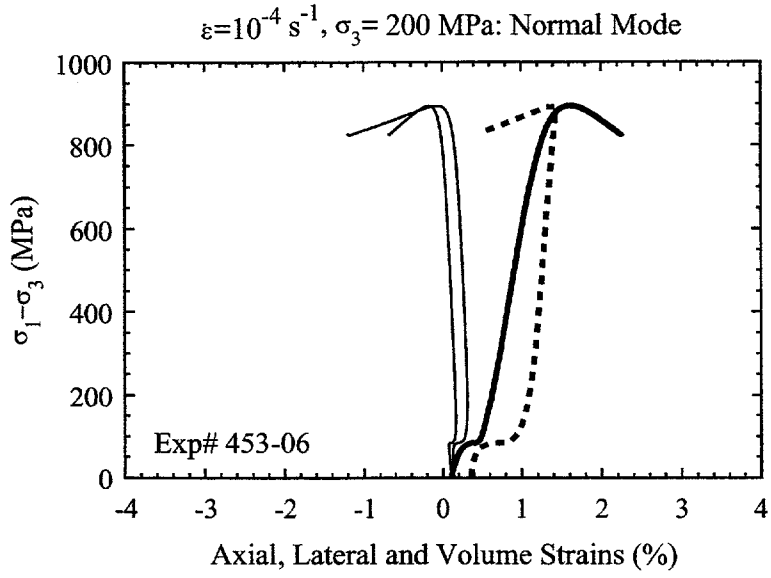

Figure A.6: Coarse solid line: axial strain. Fine solid lines: lateral strains. Dashed line: Volume strain. Normal–mode, σ_3 =200 MPa, $\dot{\epsilon}$=10^{-4} s^{-1}.

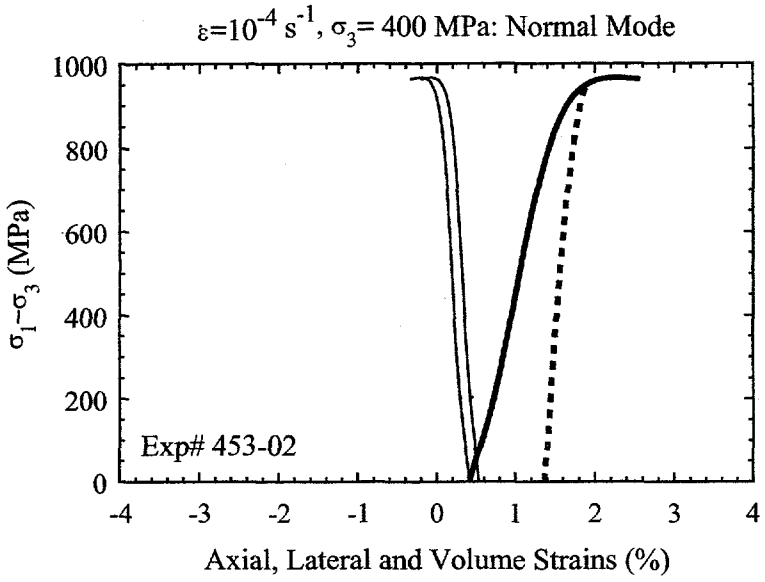

Figure A.7: Coarse solid line: axial strain. Fine solid lines: lateral strains. Dashed line: Volume strain. Normal–mode, σ_3 =400 MPa, $\dot{\epsilon}$=10^{-4} s^{-1}.

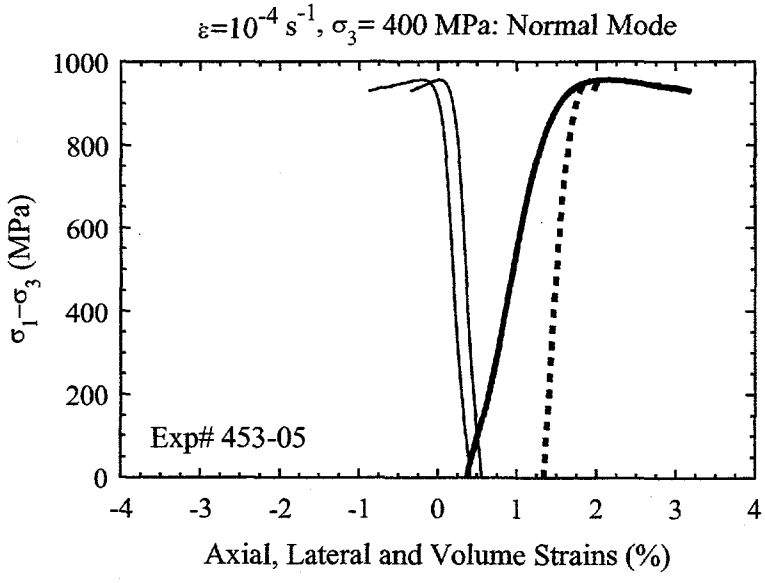

Figure A.8: Coarse solid line: axial strain. Fine solid lines: lateral strains. Dashed line: Volume strain. Normal–mode, σ_3 =400 MPa, $\dot{\epsilon}$=10^{-4} s^{-1}.

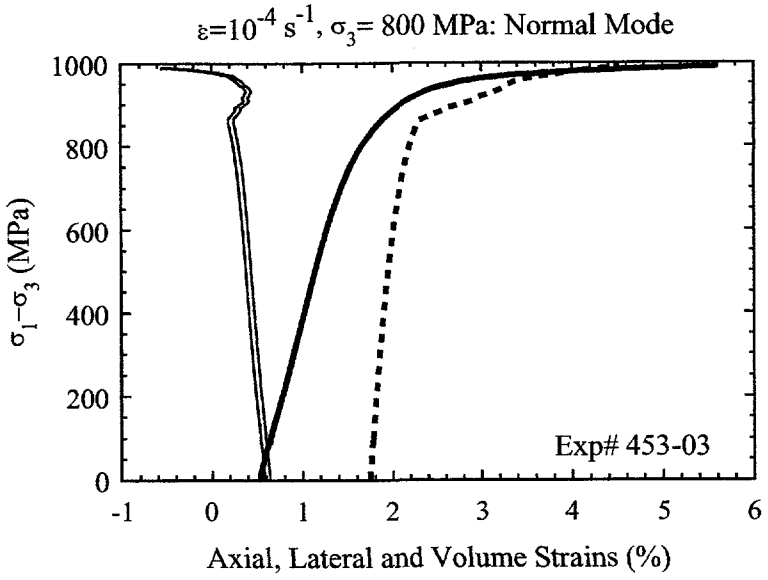

Figure A.9: Coarse solid line: axial strain. Fine solid lines: lateral strains. Dashed line: Volume strain. Normal–mode, σ_3 =800 MPa, $\dot{\epsilon}$=10^{-4} s^{-1}.

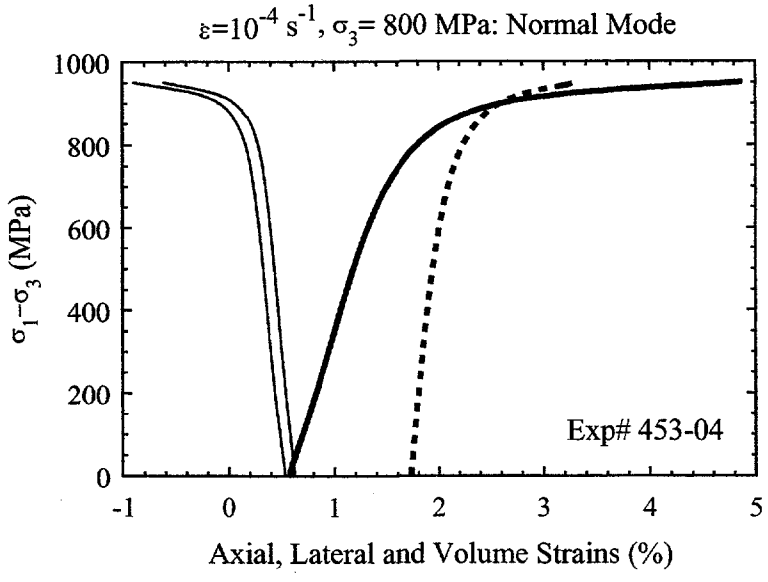

Figure A.10: Coarse solid line: axial strain. Fine solid lines: lateral strains. Dashed line: Volume strain. Normal–mode, σ_3 =800 MPa, $\dot{\epsilon}$=10^{-4} s^{-1}.

Appendix B

Hifire 453: Normal–Mode Experiments at $\dot{\epsilon}$=10^{-2} s^{-1}

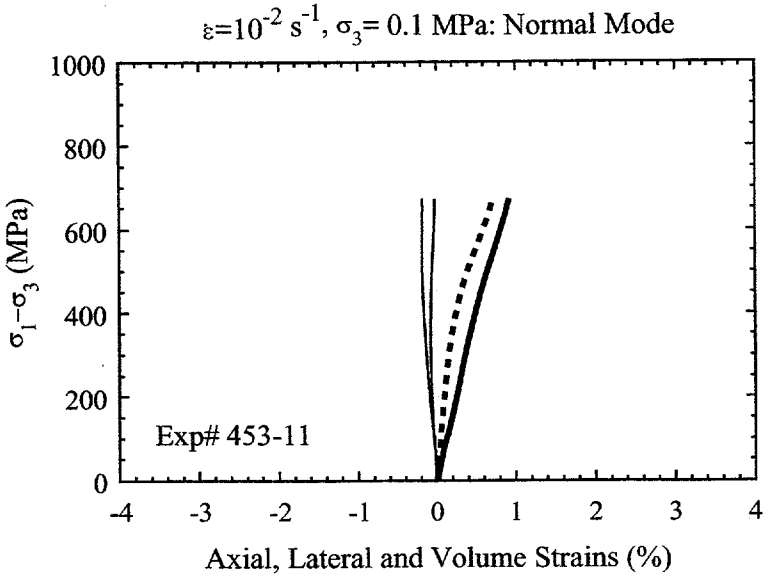

Figure B.1: Coarse solid line: axial strain. Fine solid lines: lateral strains. Dashed line: Volume strain. Normal–mode, unconfined, $\dot{\epsilon}$=10^{-2} s^{-1}.

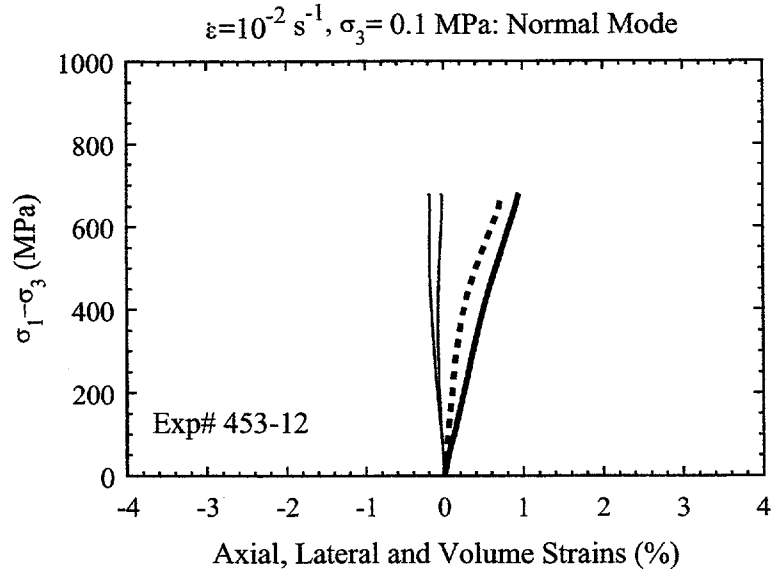

Figure B.2: Coarse solid line: axial strain. Fine solid lines: lateral strains. Dashed line: Volume strain. Normal–mode, unconfined, $\dot{\epsilon}$=10^{-2} s^{-1}.

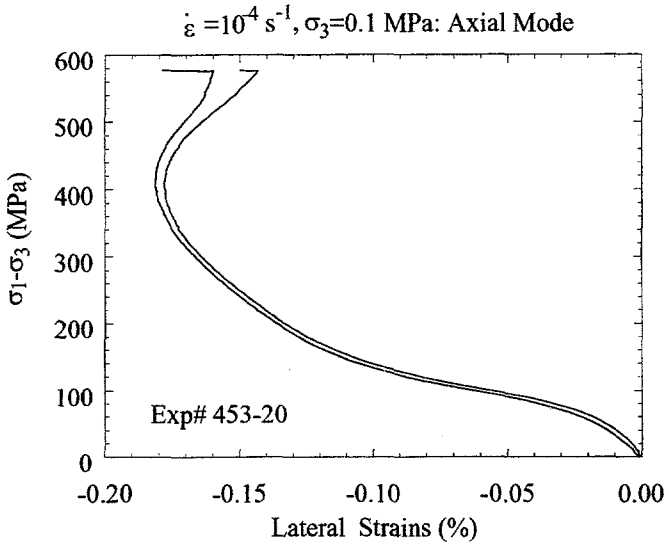

Figure B.3: Coarse solid line: axial strain. Fine solid lines: lateral strains. Dashed line: Volume strain. Normal–mode, σ_3=100 MPa, $\dot{\epsilon}$=10^{-2} s^{-1}.

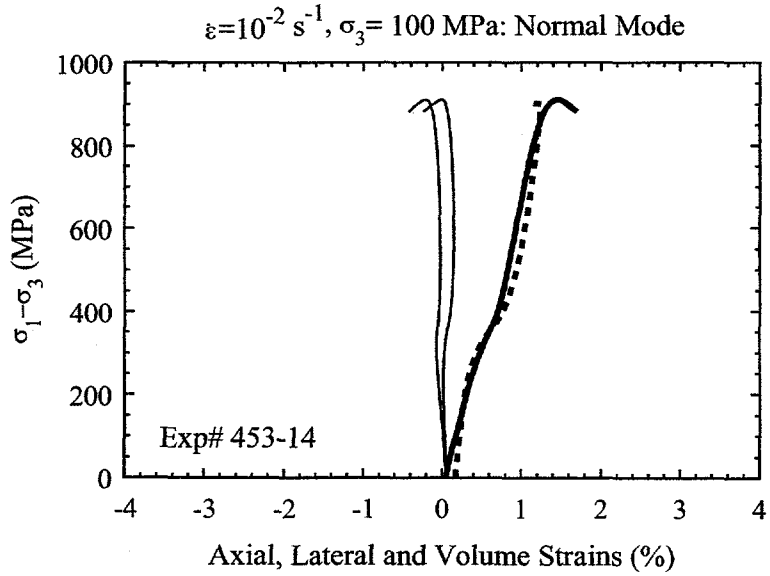

Figure B.4: Coarse solid line: axial strain. Fine solid lines: lateral strains. Dashed line: Volume strain. Normal–mode, σ_3=100 MPa, $\dot{\epsilon}$=10^{-2} s^{-1}.

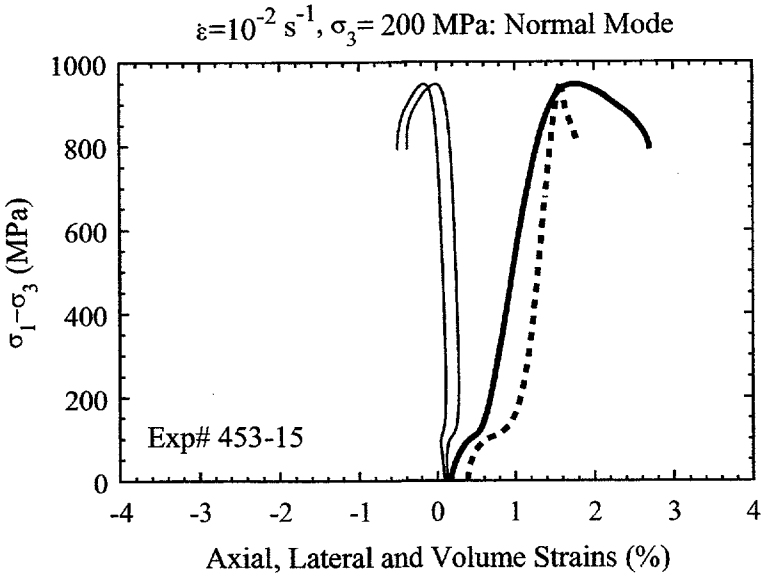

Figure B.5: Coarse solid line: axial strain. Fine solid lines: lateral strains. Dashed line: Volume strain. Normal–mode, σ_3=200 MPa, $\dot{\epsilon}$=10^{-2} s^{-1}.

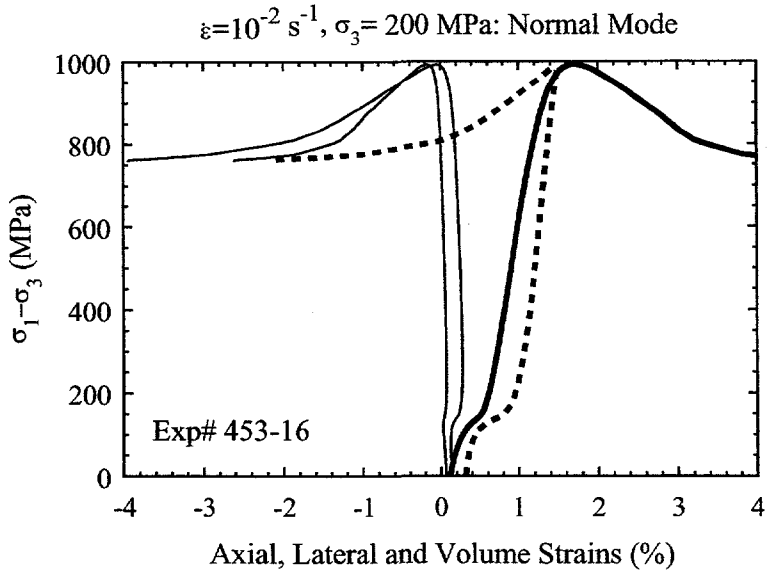

Figure B.6: Coarse solid line: axial strain. Fine solid lines: lateral strains. Dashed line: Volume strain. Normal–mode, σ_3=200 MPa, $\dot{\epsilon}$=10^{-2} s^{-1}.

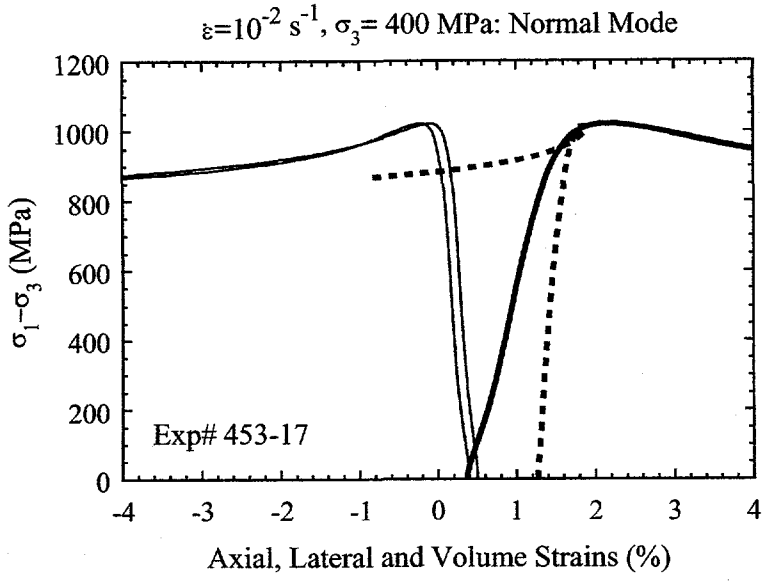

Figure B.7: Coarse solid line: axial strain. Fine solid lines: lateral strains. Dashed line: Volume strain. Normal–mode, σ_3=400 MPa, $\dot{\epsilon}$=10^{-2} s^{-1}.

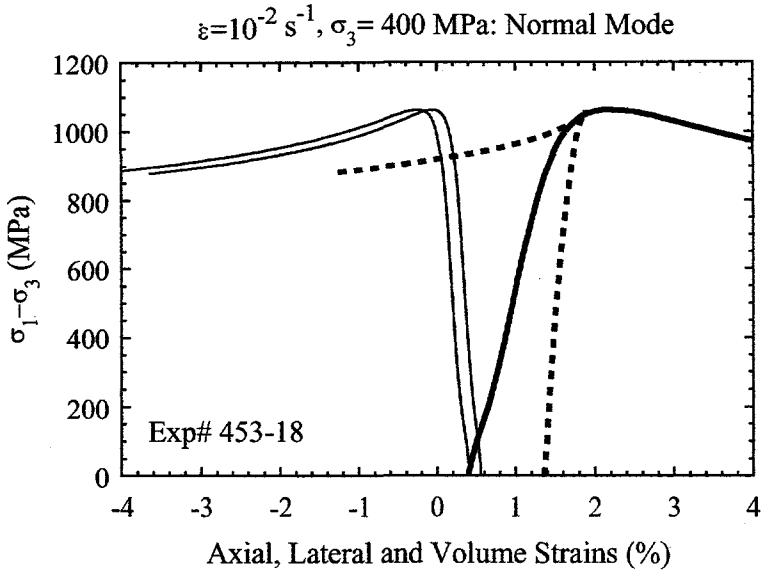

Figure B.8: Coarse solid line: axial strain. Fine solid lines: lateral strains. Dashed line: Volume strain. Normal–mode, σ_3=400 MPa, $\dot{\epsilon}$=10^{-2} s^{-1}.

THIS PAGE INTENTIONALLY LEFT BLANK

Appendix C

Hifire 453: Axial–Mode Experiments at $\dot{\epsilon}$=10^{-4} s^{-1}

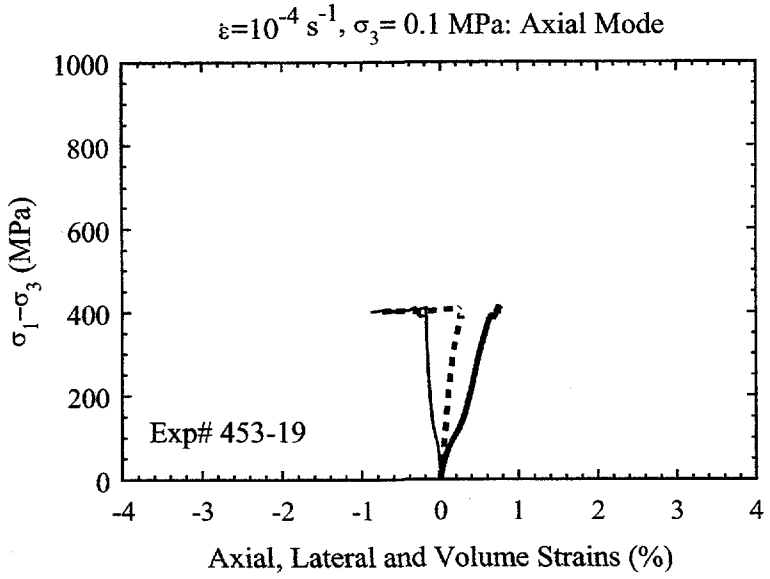

Figure C.1: Coarse solid line: axial strain. Fine solid lines: lateral strains. Dashed line: Volume strain. Axial–mode, unconfined, $\dot{\epsilon}=10^{-4}$ s^{-1}.

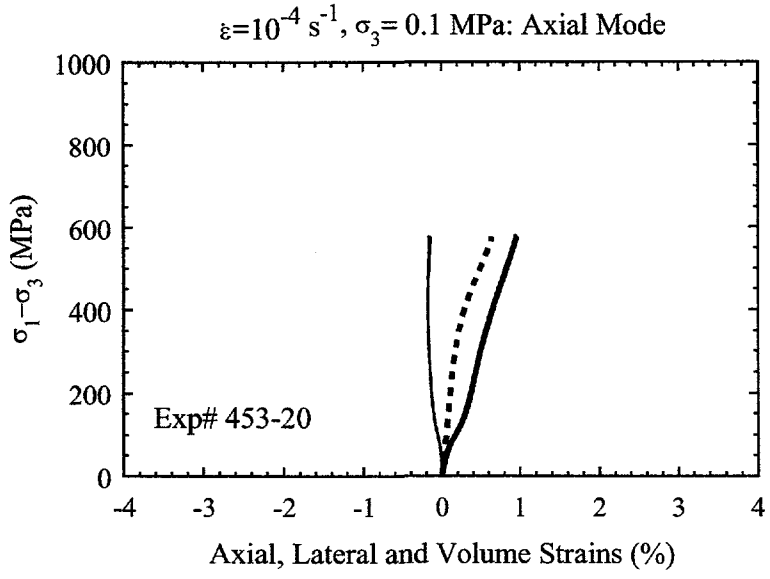

Figure C.2: Coarse solid line: axial strain. Fine solid lines: lateral strains. Dashed line: Volume strain. Axial–mode, unconfined, $\dot{\epsilon}=10^{-4}$ s^{-1}.

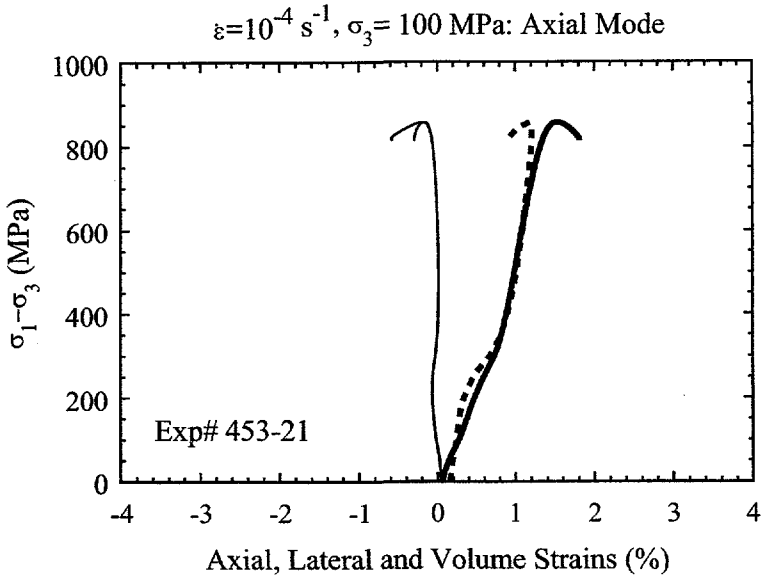

Figure C.3: Coarse solid line: axial strain. Fine solid lines: lateral strains. Dashed line: Volume strain. Axial–mode, σ_3 =100 MPa, $\dot{\epsilon}$=10^{-4} s^{-1}.

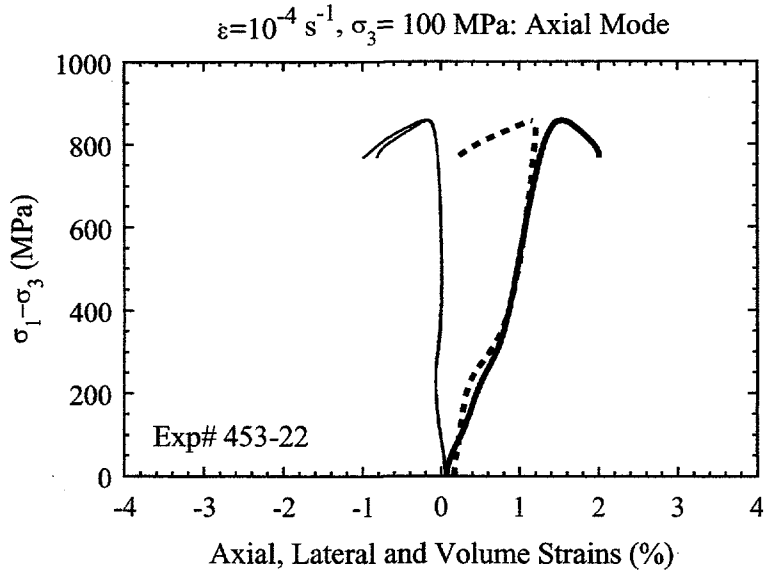

Figure C.4: Coarse solid line: axial strain. Fine solid lines: lateral strains. Dashed line: Volume strain. Axial–mode, σ_3 =100 MPa, $\dot{\epsilon}$=10^{-4} s^{-1}.

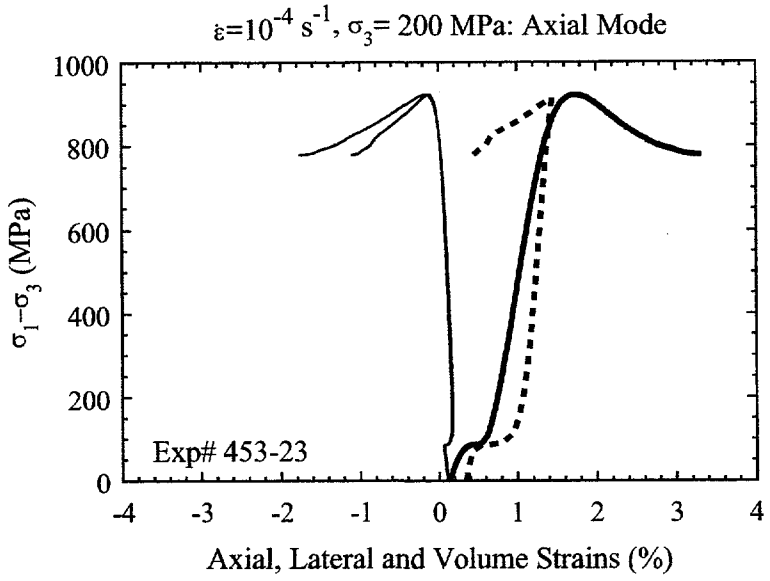

Figure C.5: Coarse solid line: axial strain. Fine solid lines: lateral strains. Dashed line: Volume strain. Axial–mode, σ_3 =200 MPa, $\dot{\epsilon}$=10^{-4} s^{-1}.

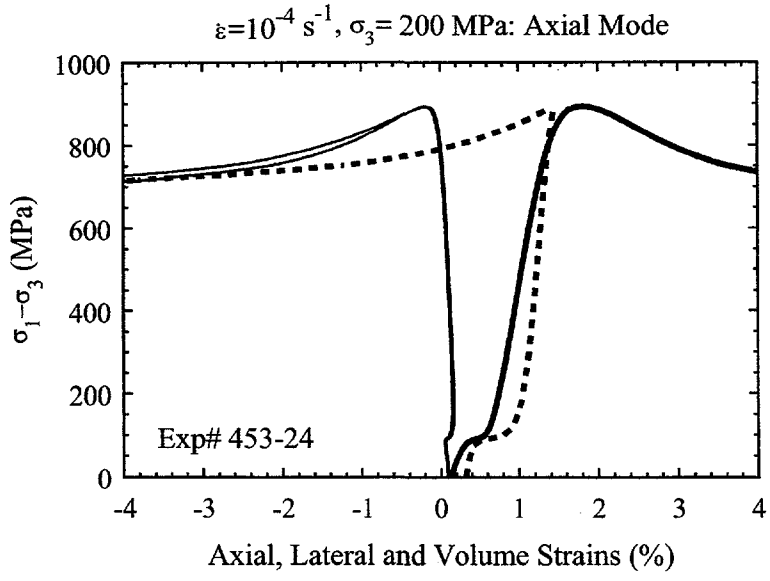

Figure C.6: Coarse solid line: axial strain. Fine solid lines: lateral strains. Dashed line: Volume strain. Axial–mode, σ_3 =200 MPa, $\dot{\epsilon}$=10^{-4} s^{-1}.

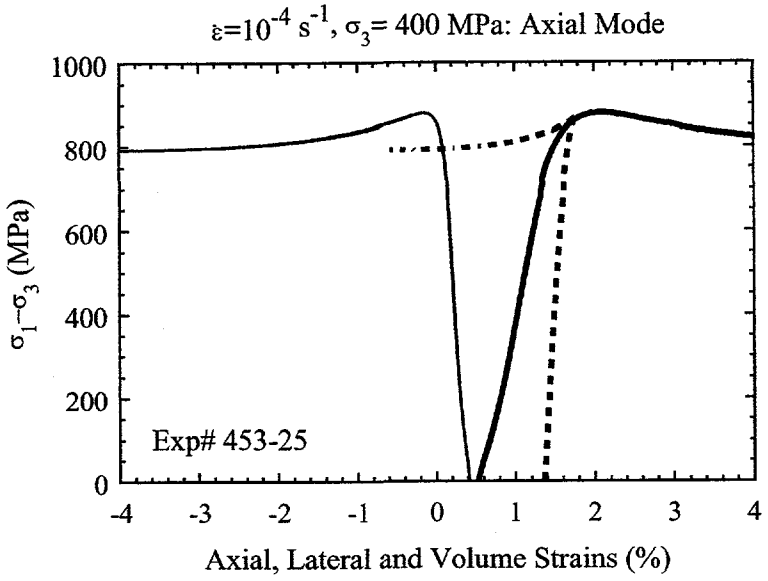

Figure C.7: Coarse solid line: axial strain. Fine solid lines: lateral strains. Dashed line: Volume strain. Axial–mode, σ_3 =400 MPa, $\dot{\epsilon}$=10^{-4} s^{-1}.

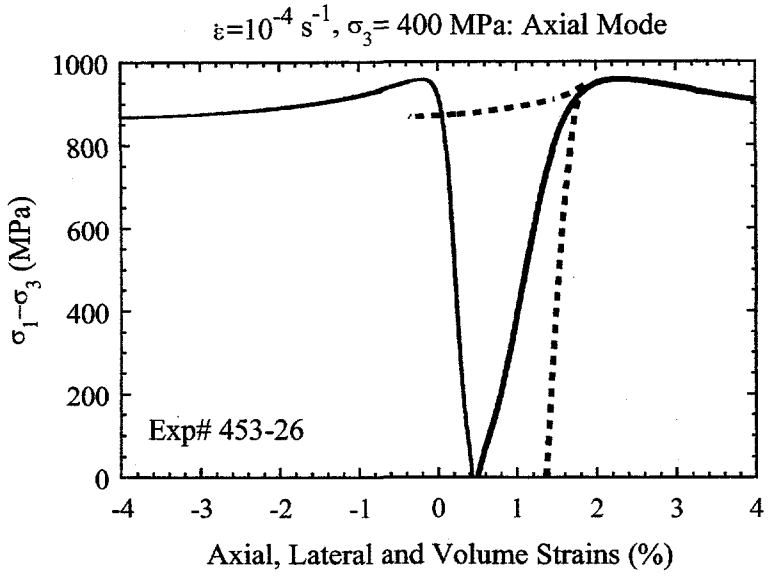

Figure C.8: Coarse solid line: axial strain. Fine solid lines: lateral strains. Dashed line: Volume strain. Axial–mode, σ_3 =400 MPa, $\dot{\epsilon}$=10^{-4} s^{-1}.

THIS PAGE INTENTIONALLY LEFT BLANK

Appendix D

Hifire 453: Axial–Mode Experiments at $\dot{\epsilon}$=10^{-2} s^{-1}

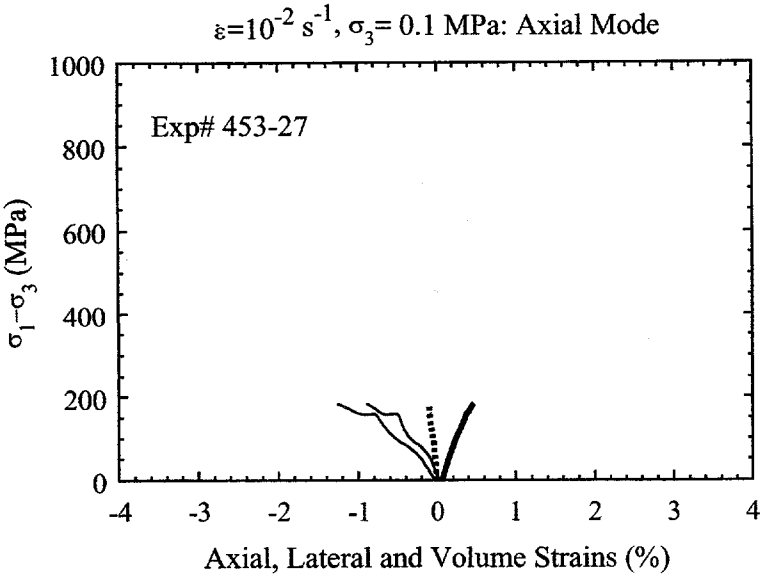

Figure D.1: Coarse solid line: axial strain. Fine solid lines: lateral strains. Dashed line: Volume strain. Axial–mode, unconfined, $\dot{\epsilon}$=10^{-2} s^{-1}.

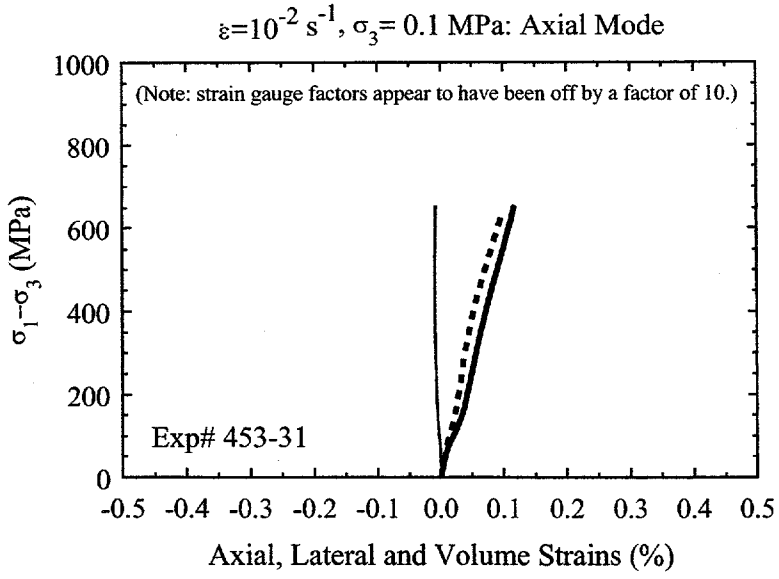

Figure D.2: Coarse solid line: axial strain. Fine solid lines: lateral strains. Dashed line: Volume strain. Axial–mode, unconfined, $\dot{\epsilon}$=10^{-2} s^{-1}.

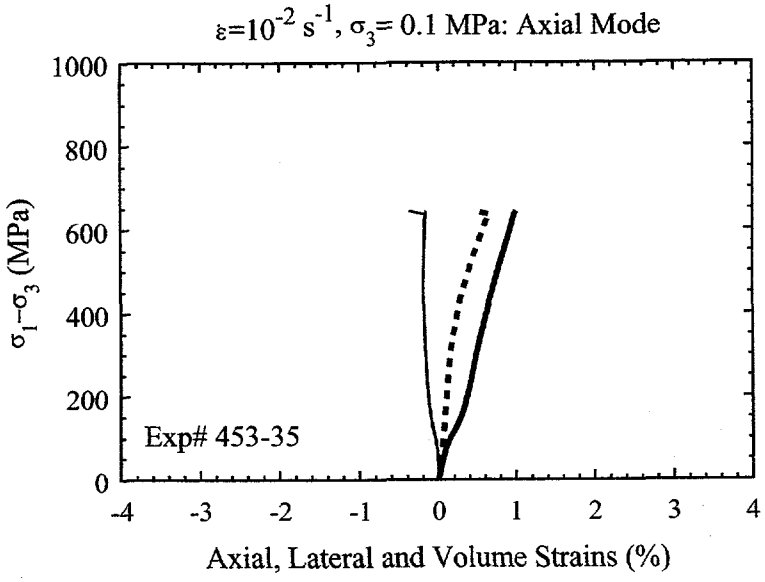

Figure D.3: Coarse solid line: axial strain. Fine solid lines: lateral strains. Dashed line: Volume strain. Axial–mode, unconfined, $\dot{\epsilon}=10^{-2}$ s^{-1}.

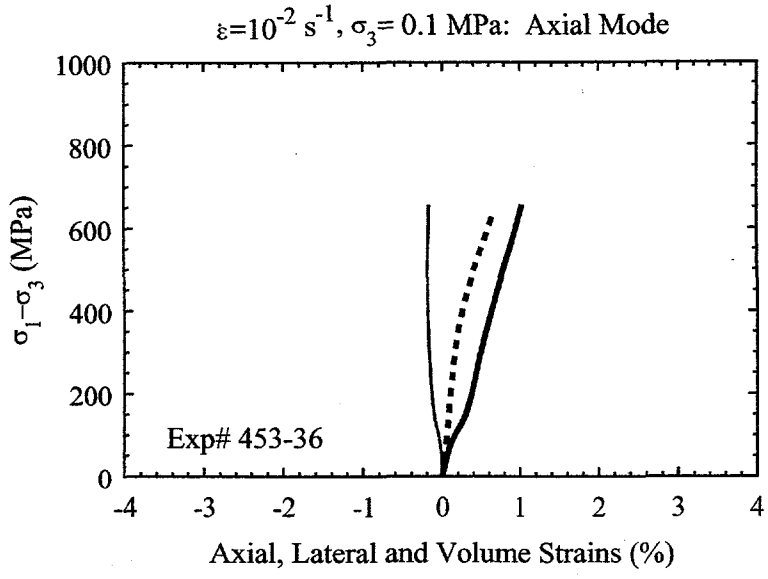

Figure D.4: Coarse solid line: axial strain. Fine solid lines: lateral strains. Dashed line: Volume strain. Axial–mode, unconfined, $\dot{\epsilon}=10^{-2}$ s^{-1}.

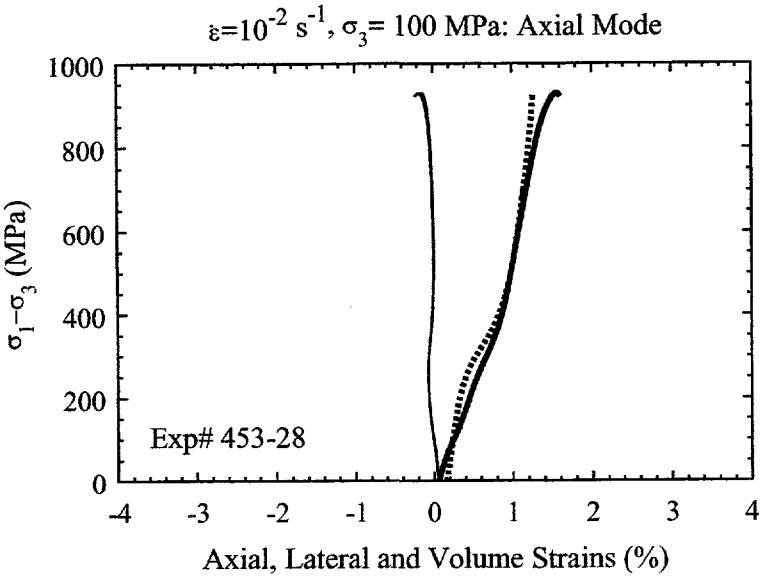

Figure D.5: Coarse solid line: axial strain. Fine solid lines: lateral strains. Dashed line: Volume strain. Axial–mode, σ_3 =100 MPa, $\dot{\epsilon}$=10^{-2} s^{-1}.

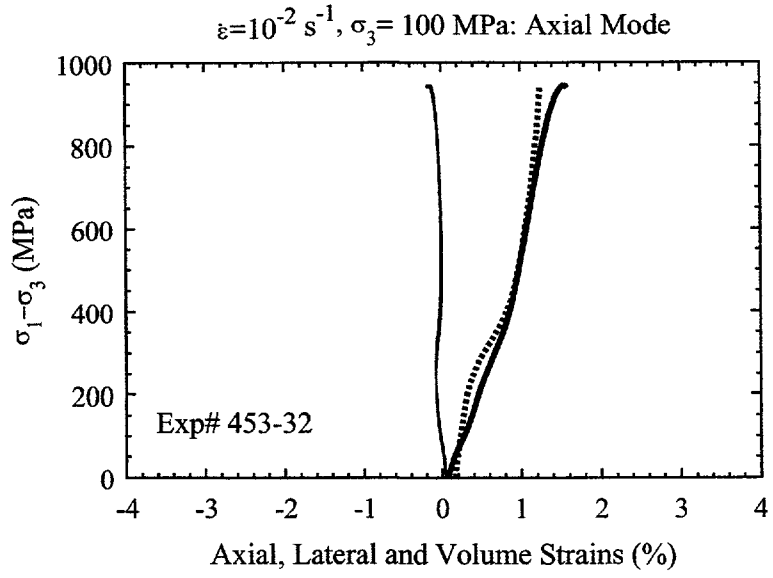

Figure D.6: Coarse solid line: axial strain. Fine solid lines: lateral strains. Dashed line: Volume strain. Axial–mode, σ_3 =100 MPa, $\dot{\epsilon}$=10^{-2} s^{-1}.

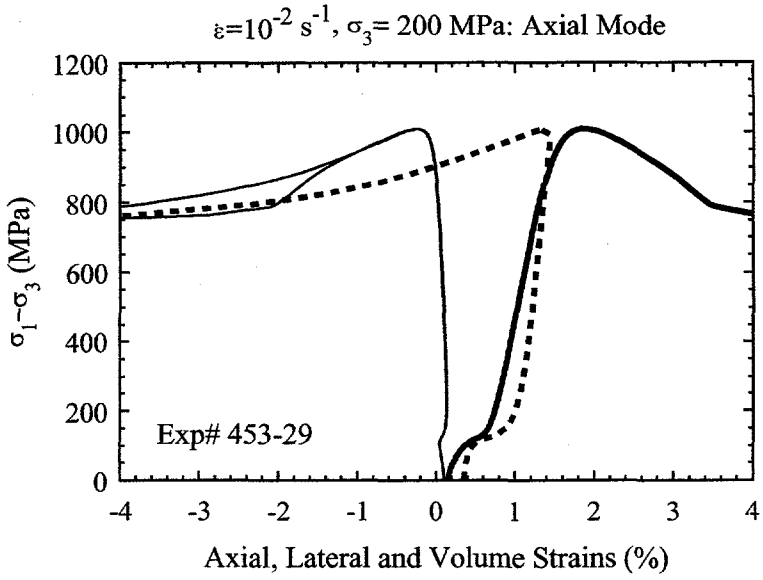

Figure D.7: Coarse solid line: axial strain. Fine solid lines: lateral strains. Dashed line: Volume strain. Axial–mode, σ_3 =200 MPa, $\dot{\epsilon}$=10^{-2} s^{-1}.

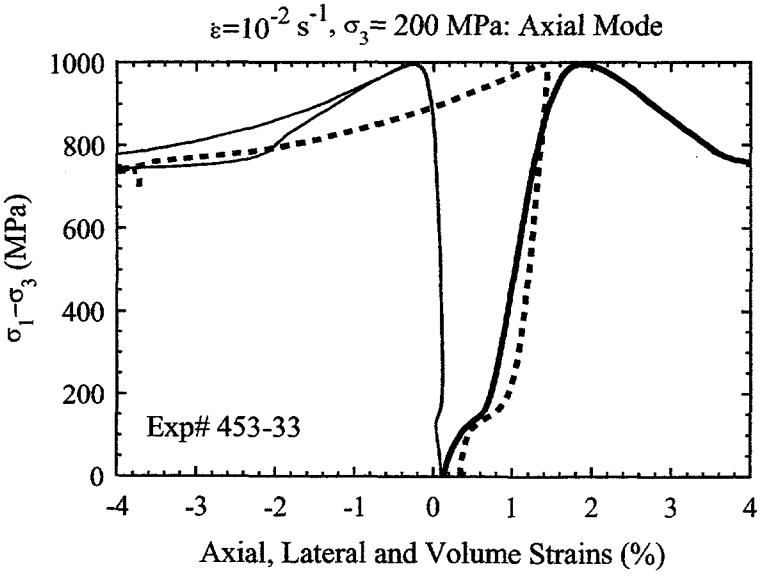

Figure D.8: Coarse solid line: axial strain. Fine solid lines: lateral strains. Dashed line: Volume strain. Axial–mode, σ_3 =200 MPa, $\dot{\epsilon}$=10^{-2} s^{-1}.

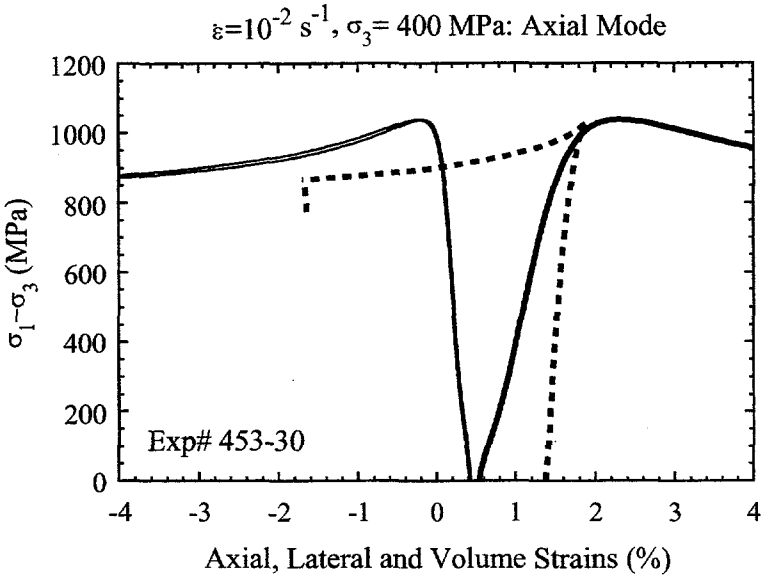

Figure D.9: Coarse solid line: axial strain. Fine solid lines: lateral strains. Dashed line: Volume strain. Axial–mode, σ_3 =400 MPa, $\dot{\epsilon}$=10^{-2} s^{-1}.

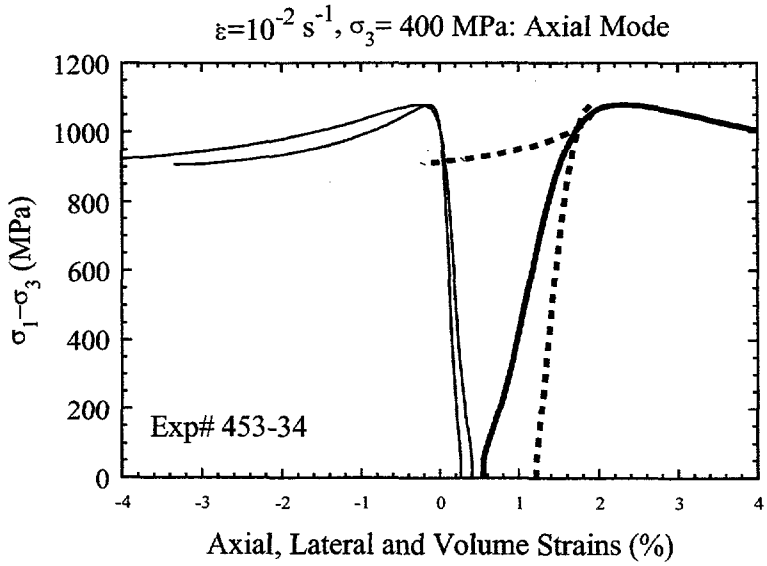

Figure D.10: Coarse solid line: axial strain. Fine solid lines: lateral strains. Dashed line: Volume strain. Axial–mode, σ_3 =400 MPa, $\dot{\epsilon}$=10^{-2} s^{-1}.

Appendix E

Hifire 424: Uniaxial Compression Experiments on Unpoled Ceramic

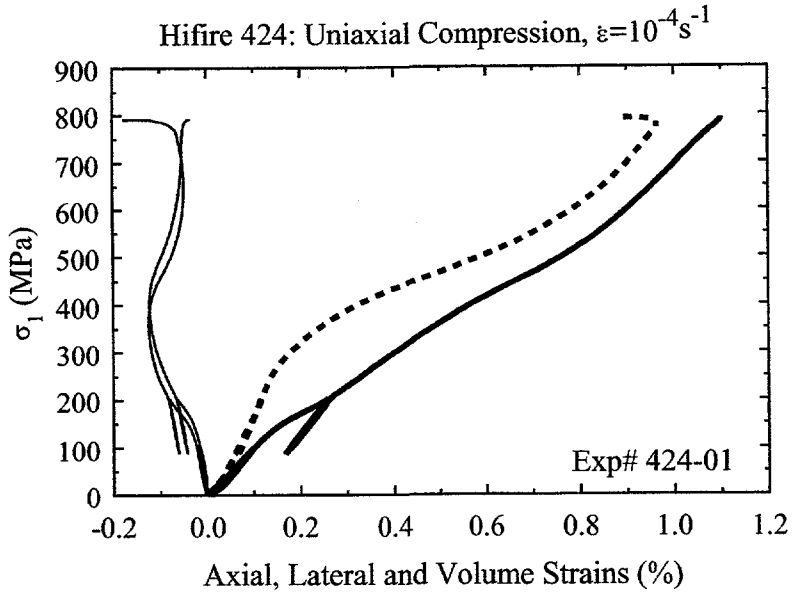

Figure E.1: Coarse solid line: axial strain. Fine solid lines: lateral strains. Dashed line: Volume strain.

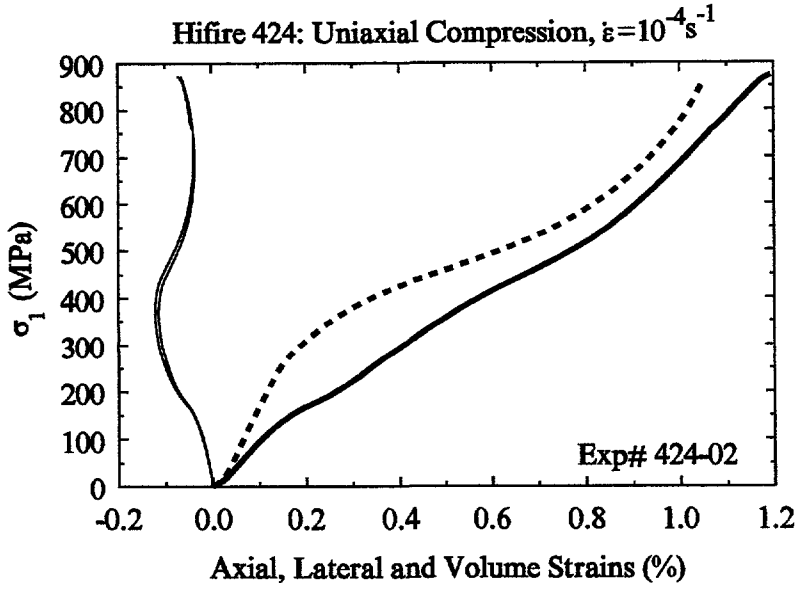

Figure E.2: Coarse solid line: axial strain. Fine solid lines: lateral strains. Dashed line: Volume strain.

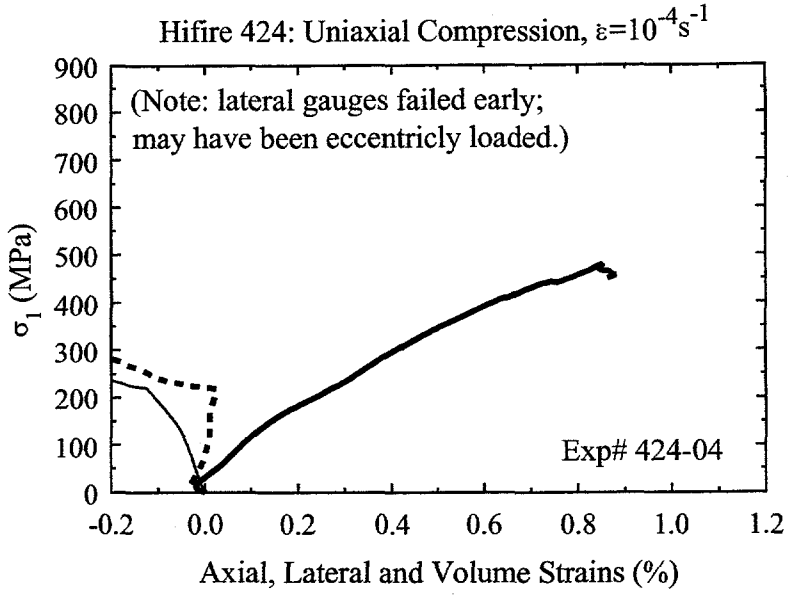

Figure E.3: Coarse solid line: axial strain. Fine solid lines: lateral strains. Dashed line: Volume strain.

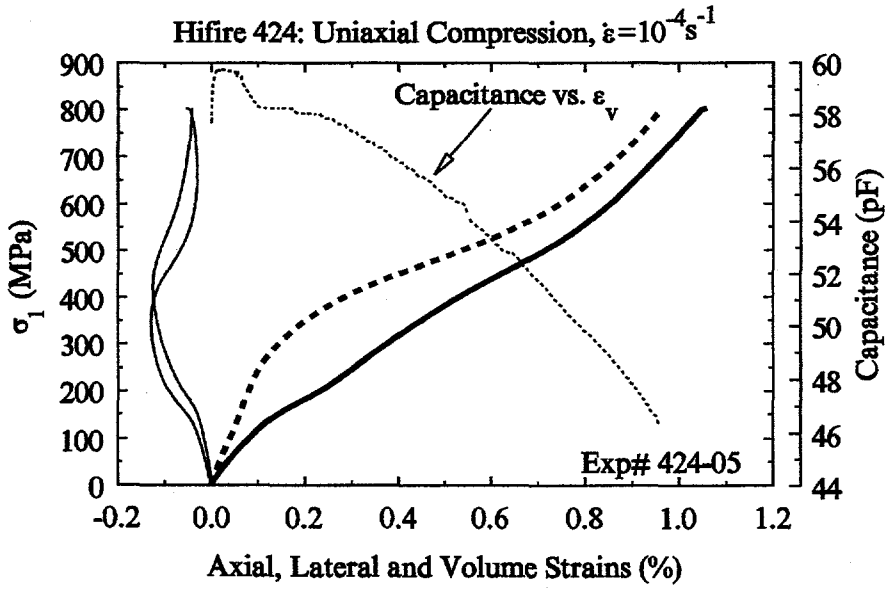

Figure E.4: Coarse solid line: axial strain. Fine solid lines: lateral strains. Dashed line: Volume strain.

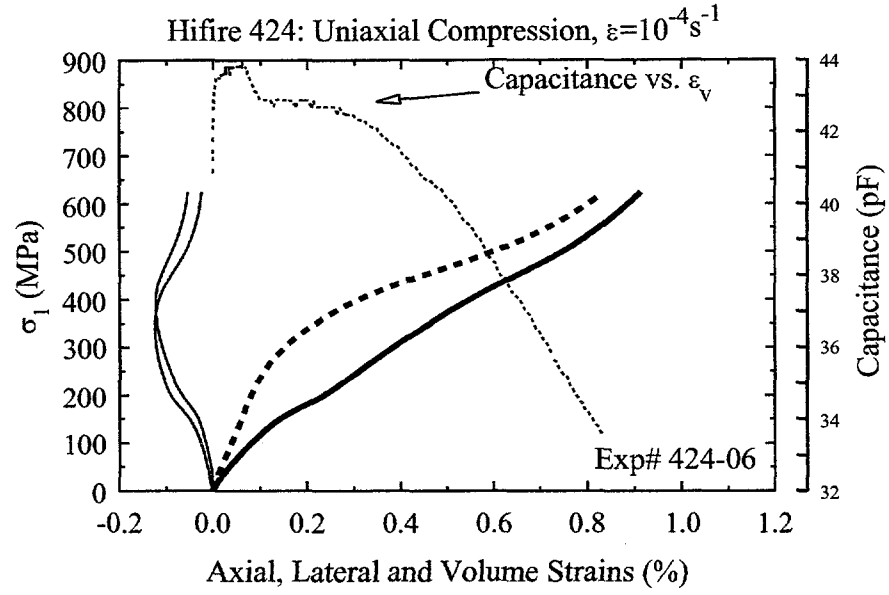

Figure E.5: Coarse solid line: axial strain. Fine solid lines: lateral strains. Dashed line: Volume strain. Note: this specimen was not taken to failure.

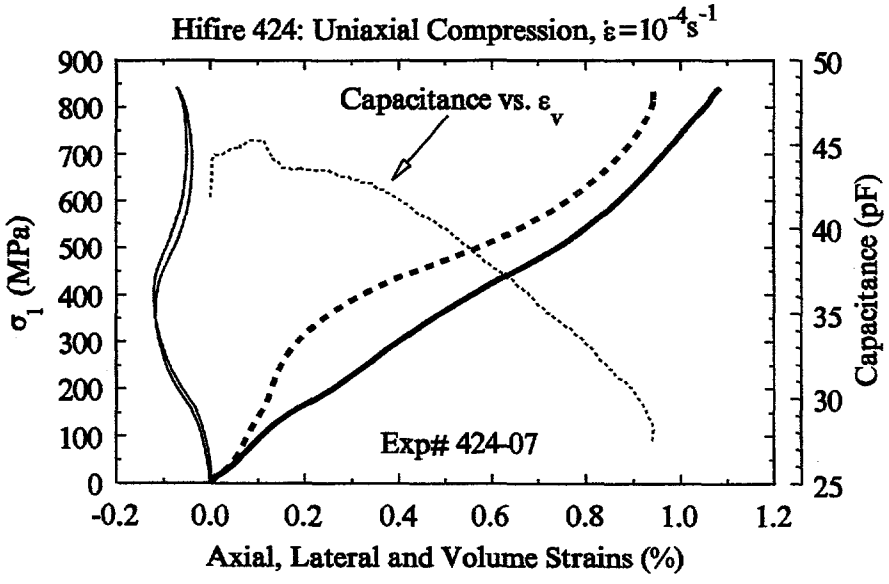

Figure E.6: Coarse solid line: axial strain. Fine solid lines: lateral strains. Dashed line: Volume strain.

Appendix F

Hifire 541-1: Uniaxial Compression Experiments on Unpoled Ceramic

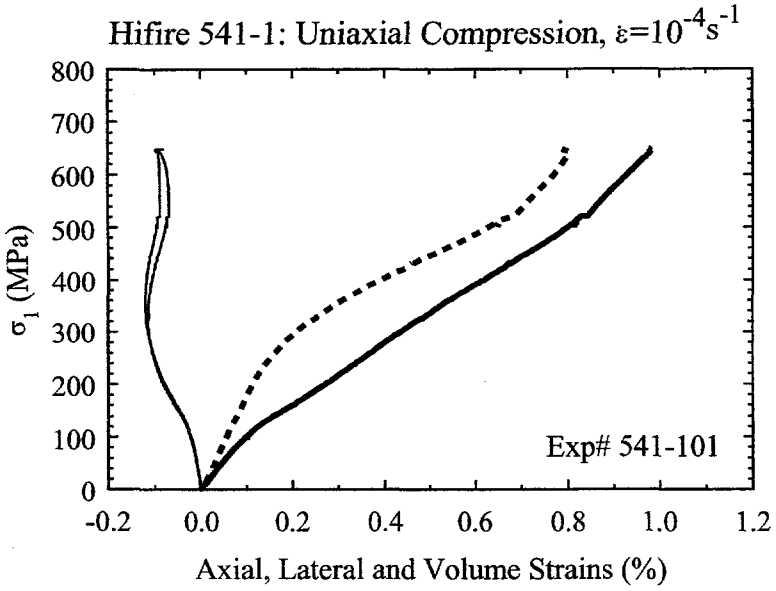

Figure F.1: Coarse solid line: axial strain. Fine solid lines: lateral strains. Dashed line: Volume strain. Note: unload/reload cycles have been removed from the data for clarity.

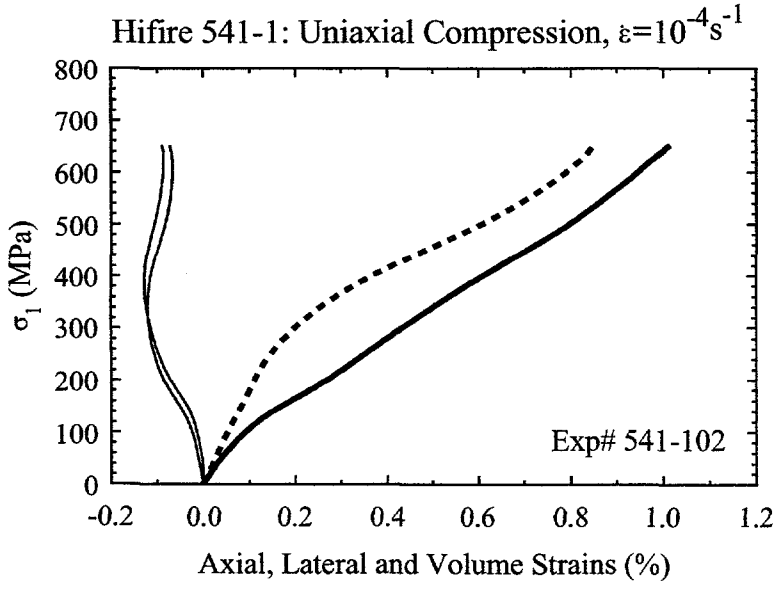

Figure F.2: Coarse solid line: axial strain. Fine solid lines: lateral strains. Dashed line: Volume strain.

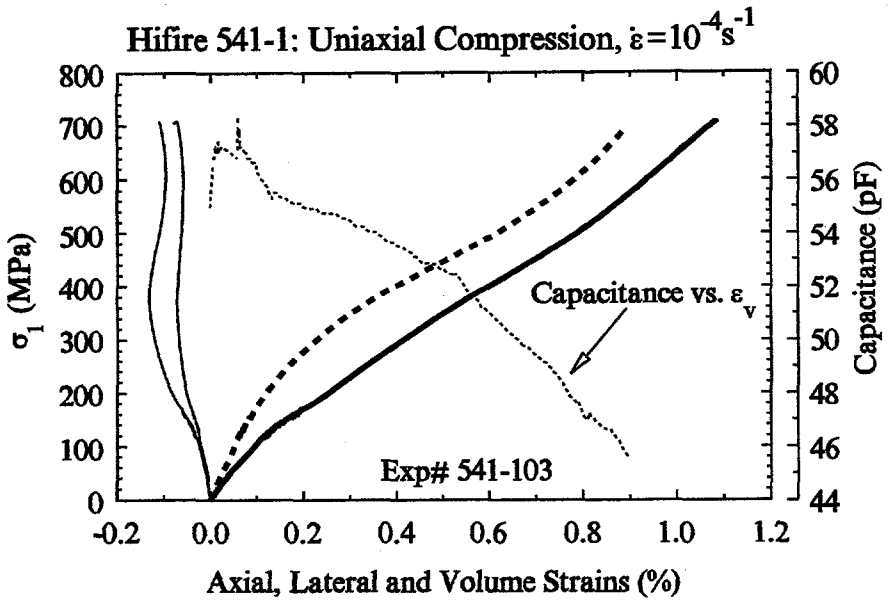

Figure F.3: Coarse solid line: axial strain. Fine solid lines: lateral strains. Dashed line: Volume strain.

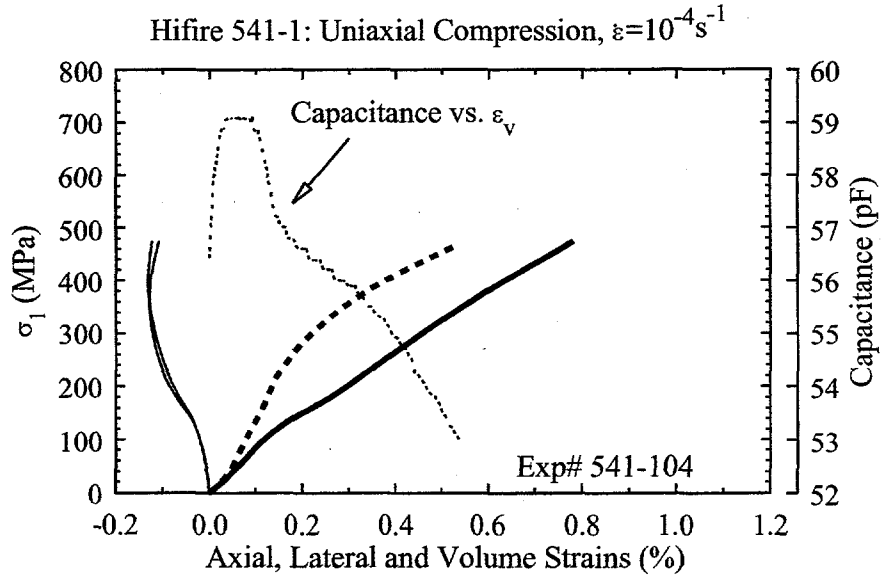

Figure F.4: Coarse solid line: axial strain. Fine solid lines: lateral strains. Dashed line: Volume strain. Note: this specimen was not taken to failure.

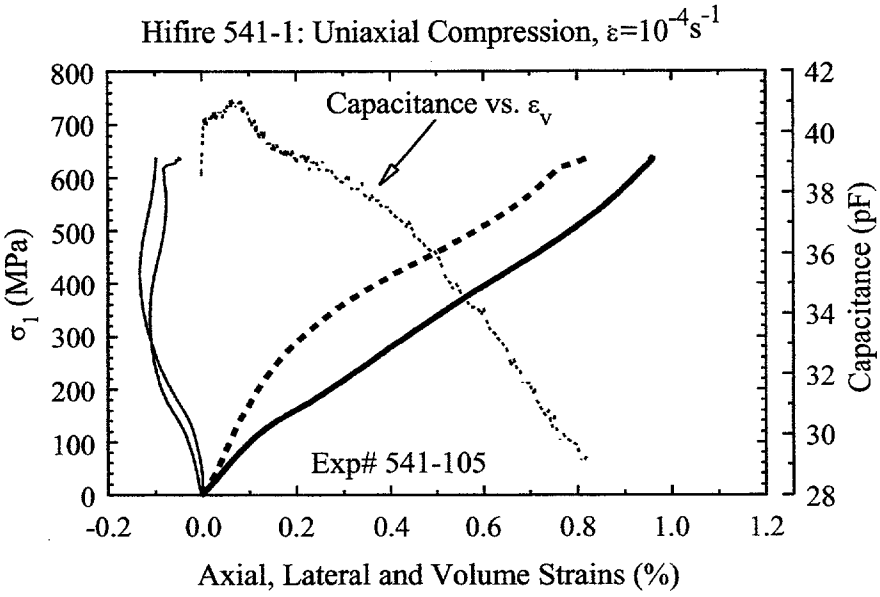

Figure F.5: Coarse solid line: axial strain. Fine solid lines: lateral strains. Dashed line: Volume strain.

Appendix G

Hifire 541-1: Uniaxial Compression Experiments on Poled Ceramic

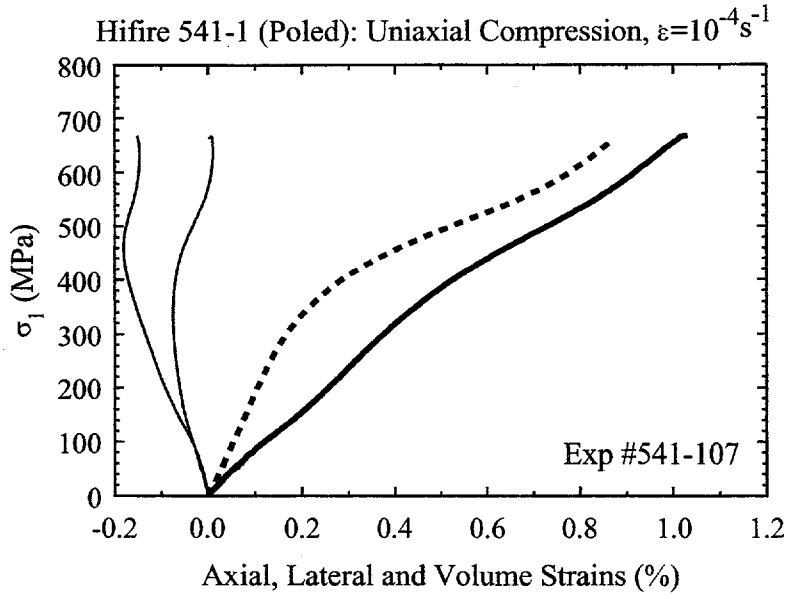

Figure G.1: Coarse solid line: axial strain. Fine solid lines: lateral strains. Dashed line: Volume strain.

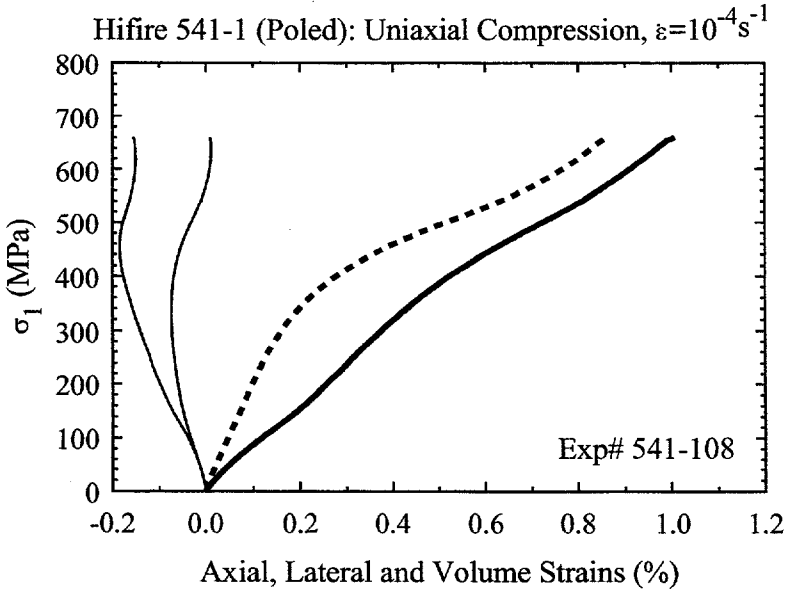

Figure G.2: Coarse solid line: axial strain. Fine solid lines: lateral strains. Dashed line: Volume strain.

Appendix H

Hifire 453: Hydrostatic Compression and CSD Experiments on Unpoled Ceramic

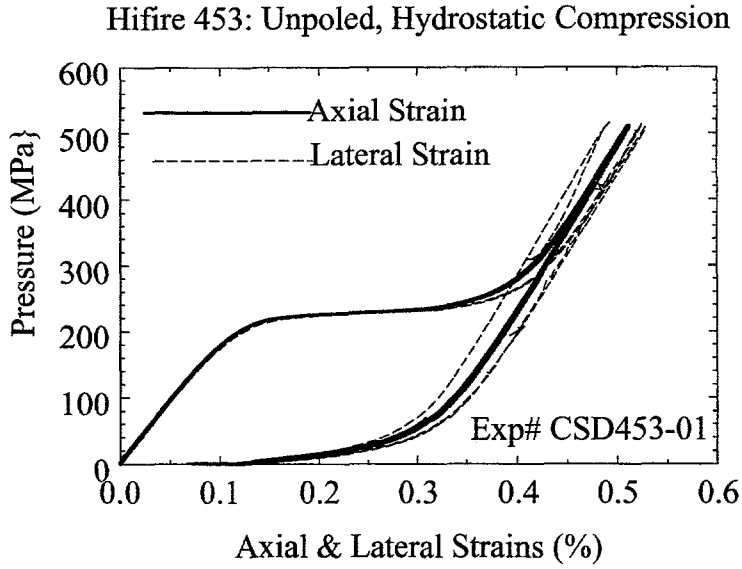

Figure H.1: Coarse solid lines: axial strains. Dashed lines: Lateral strains.

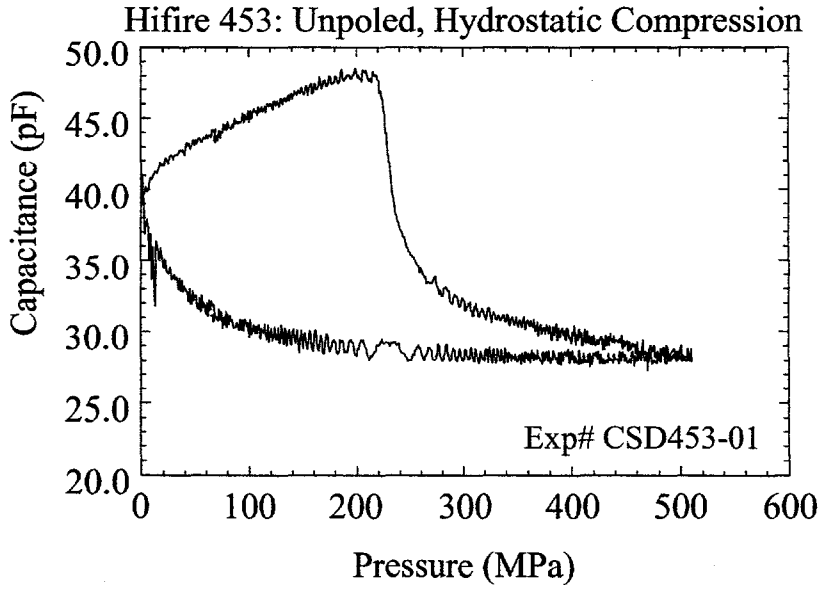

Figure H.2: Capacitance data for hydrostatic compression experiment CSD453-01, above.

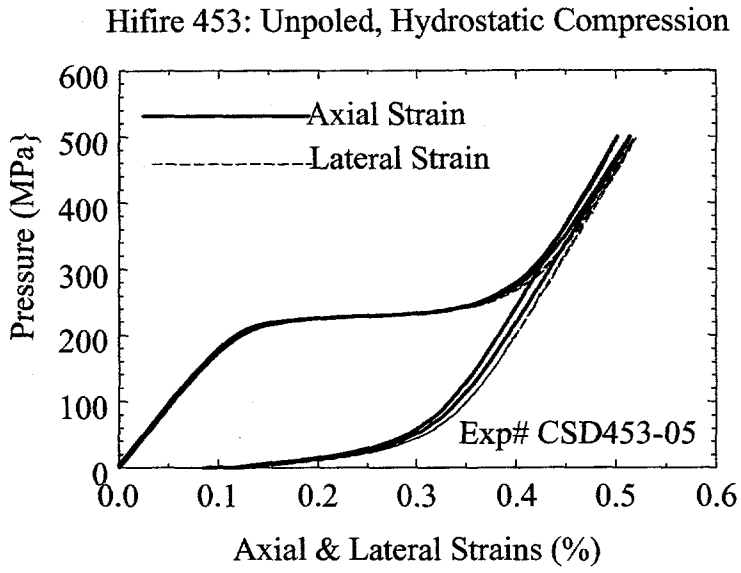

Figure H.3: Coarse solid lines: axial strains. Dashed lines: Lateral strains.

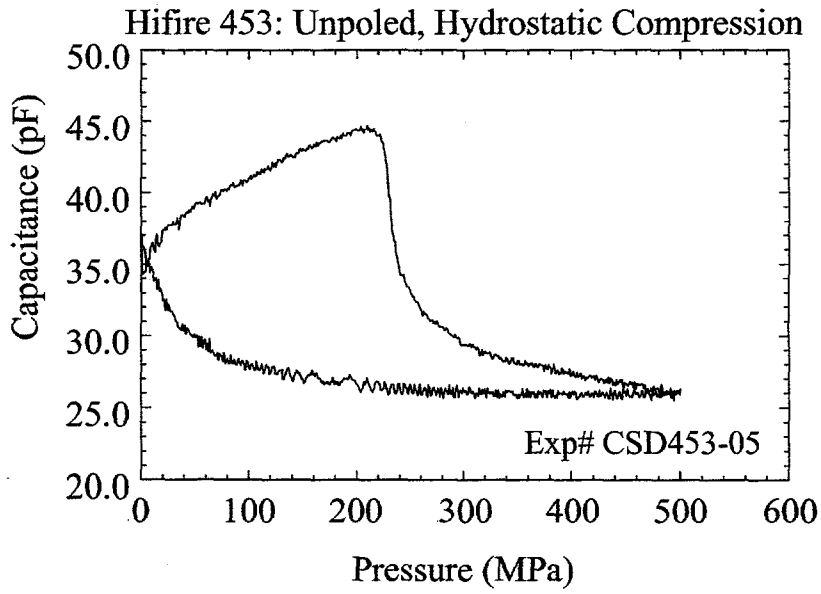

Figure H.4: Capacitance data for hydrostatic compression experiment CSD453-05, above.

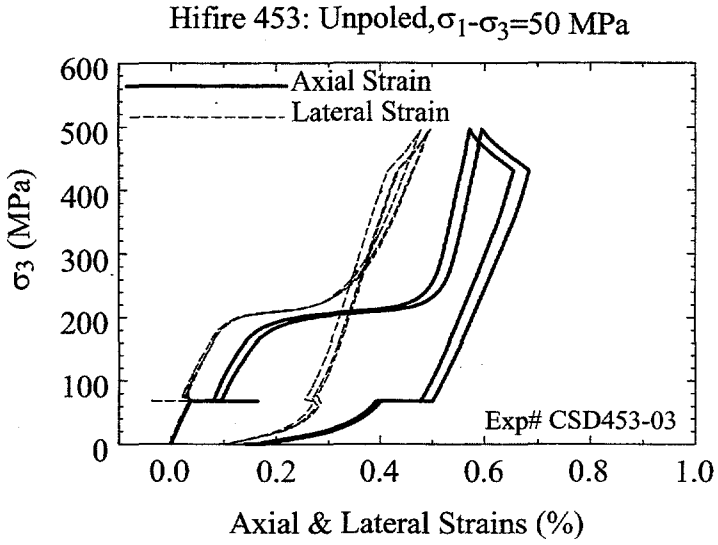

Figure H.5: Coarse solid lines: axial strains. Dashed lines: Lateral strains.

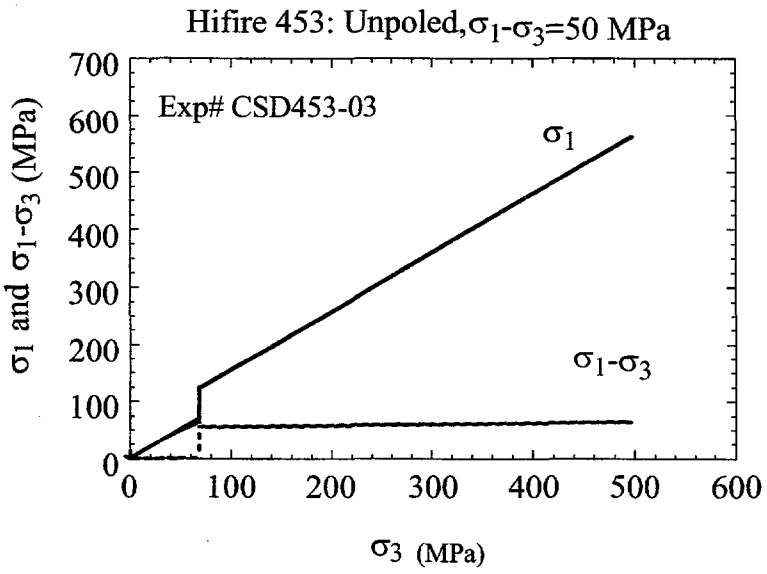

Figure H.6: Load path for experiment CSD453-03, above.

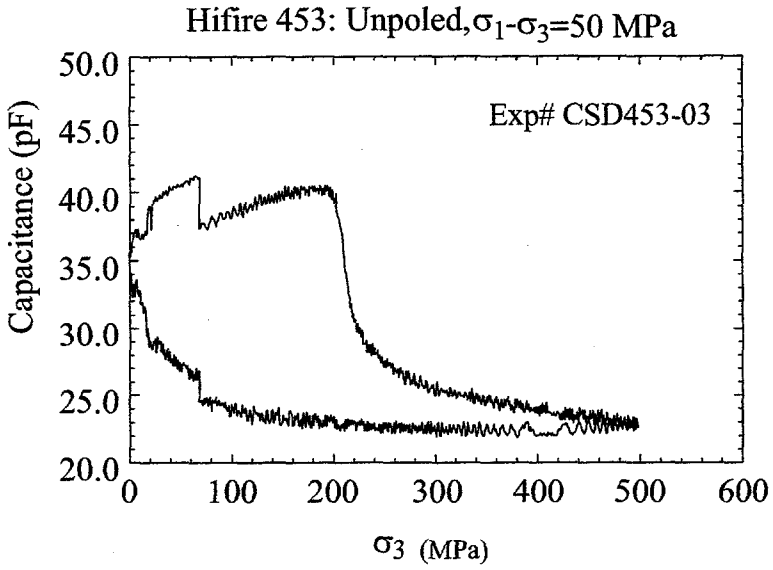

Figure H.7: Capacitance data for experiment CSD453-03, above.

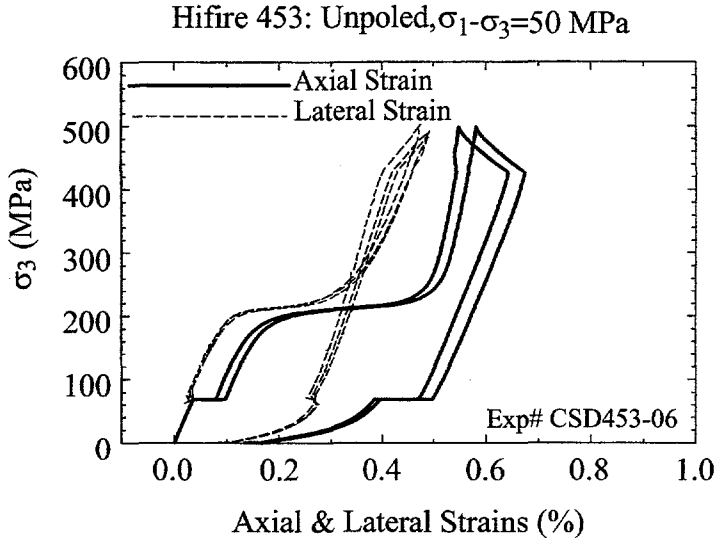

Figure H.8: Coarse solid lines: axial strains. Dashed lines: Lateral strains.

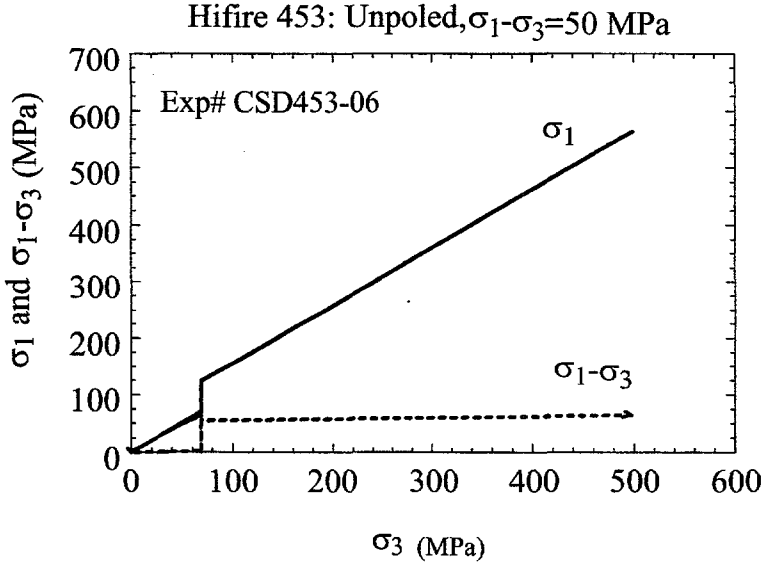

Figure H.9: Load path for experiment CSD453-06, above.

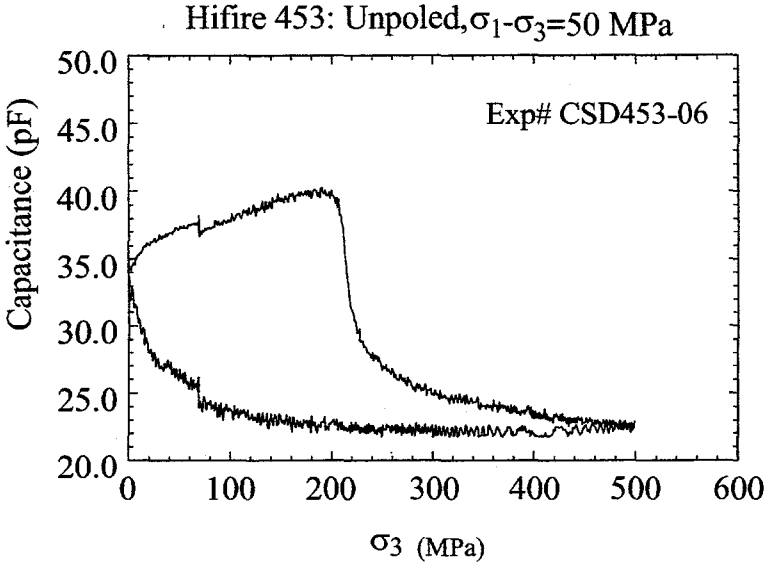

Figure H.10: Capacitance data for experiment CSD453-06, above.

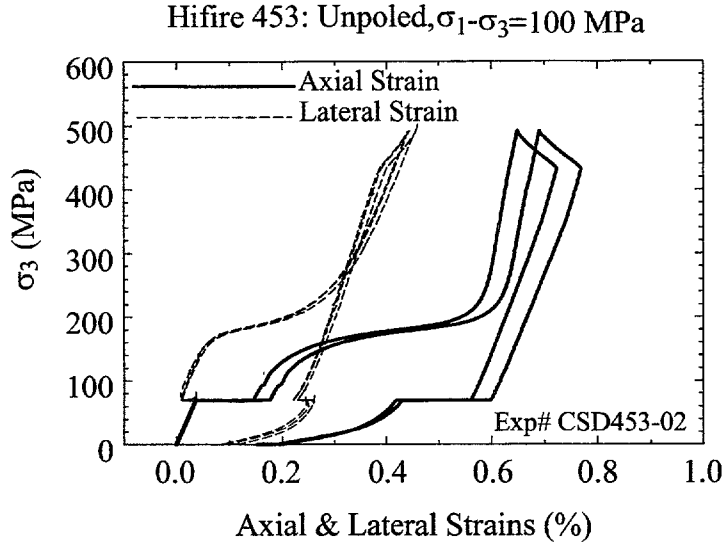

Figure H.11: Coarse solid lines: axial strains. Dashed lines: Lateral strains.

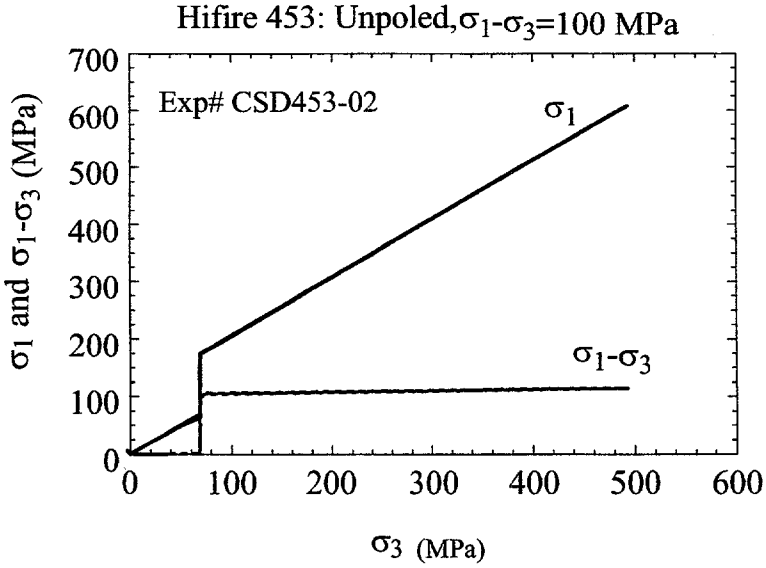

Figure H.12: Load path for experiment CSD453-02, above.

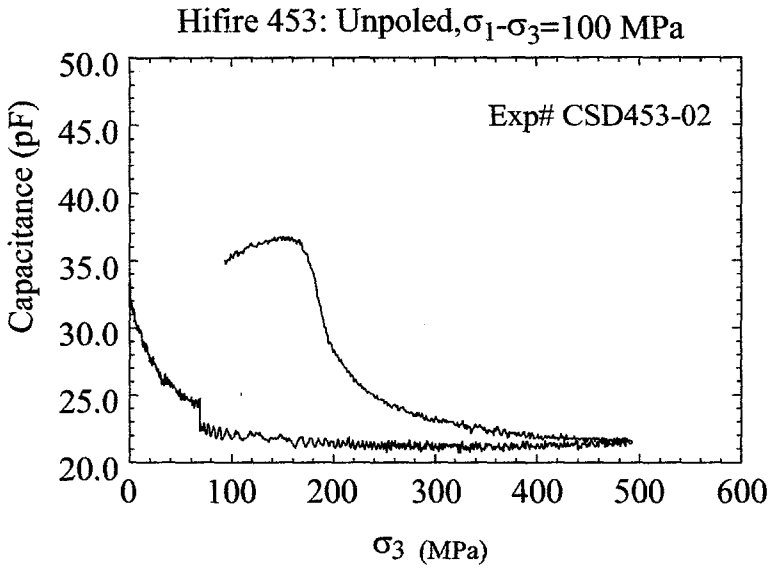

Figure H.13: Capacitance data for experiment CSD453-02, above.

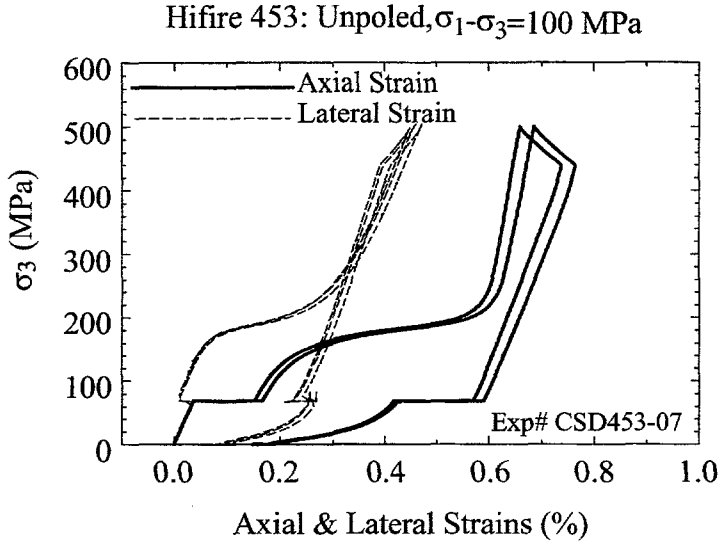

Figure H.14: Coarse solid lines: axial strains. Dashed lines: Lateral strains.

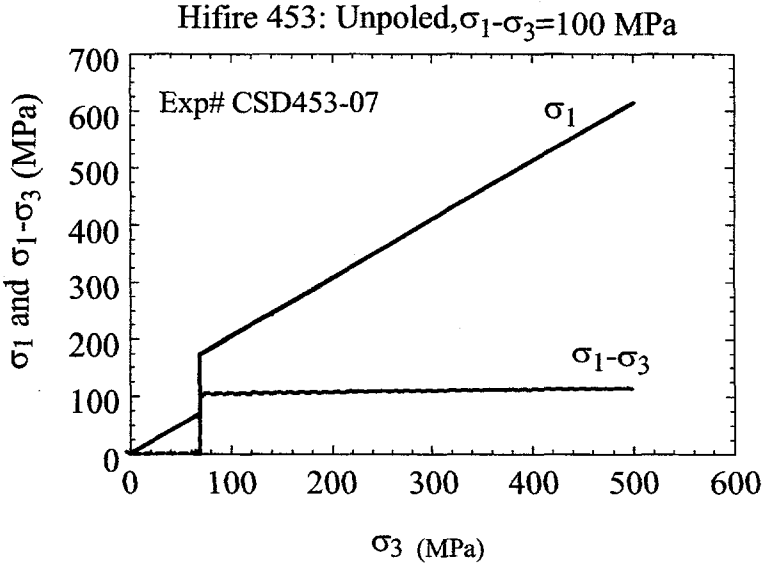

Figure H.15: Load path for experiment CSD453-07, above.

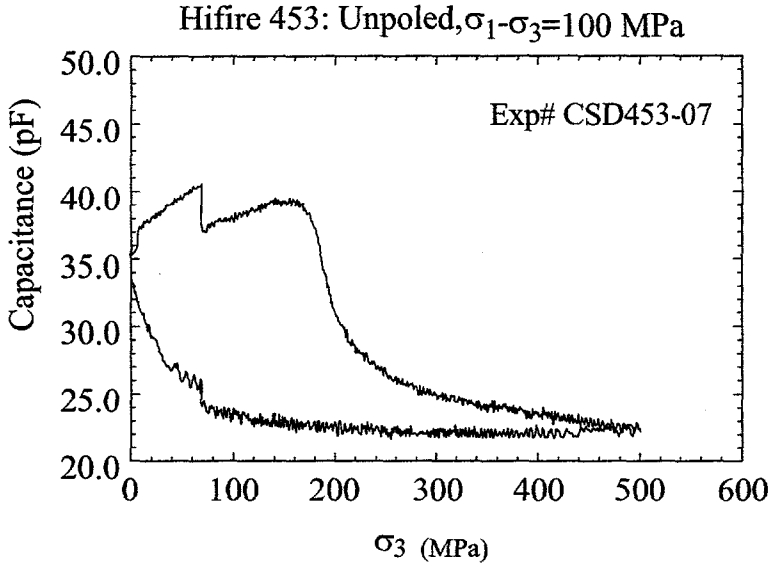

Figure H.16: Capacitance data for experiment CSD453-07, above.

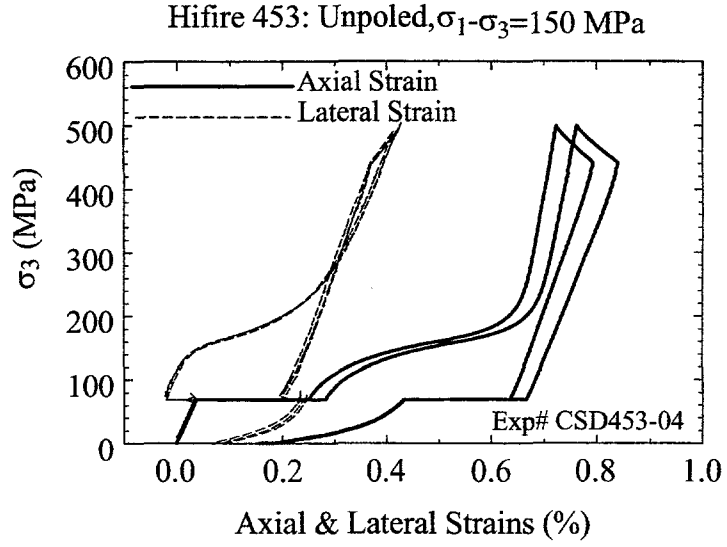

Figure H.17: Coarse solid lines: axial strains. Dashed lines: Lateral strains.

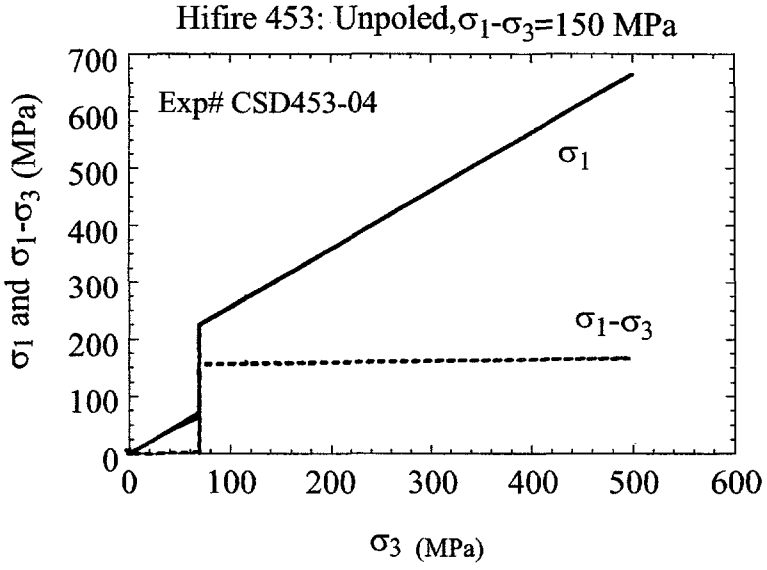

Figure H.18: Load path for experiment CSD453-04, above.

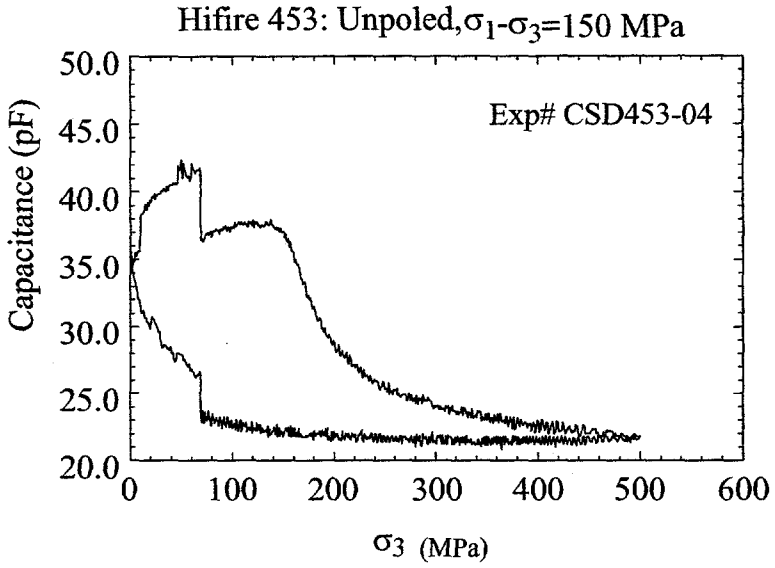

Figure H.19: Capacitance data for experiment CSD453-04, above.

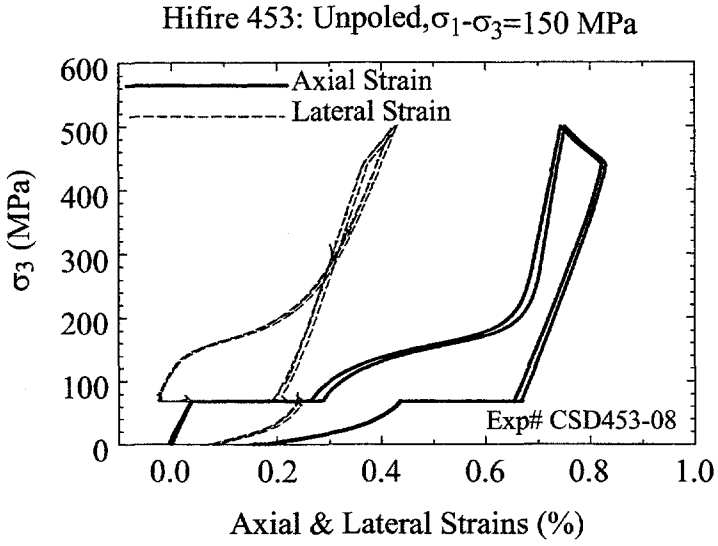

Figure H.20: Coarse solid lines: axial strains. Dashed lines: Lateral strains.

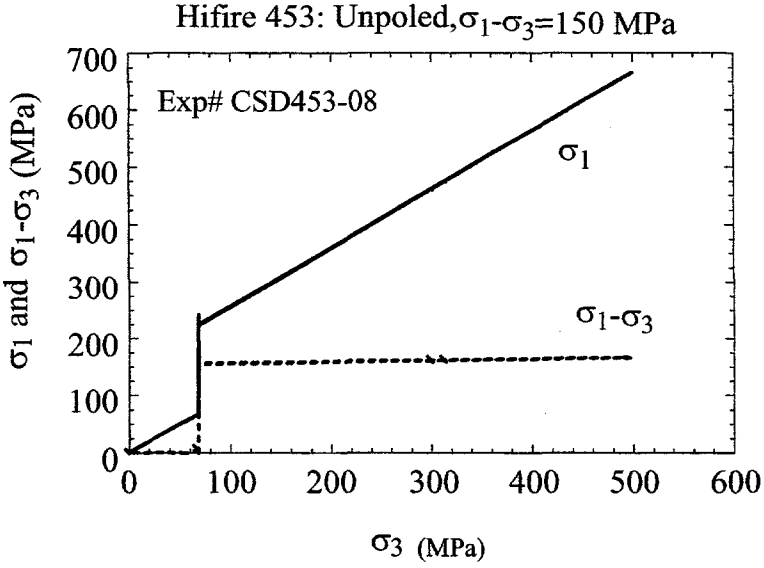

Figure H.21: Load path for experiment CSD453-08, above.

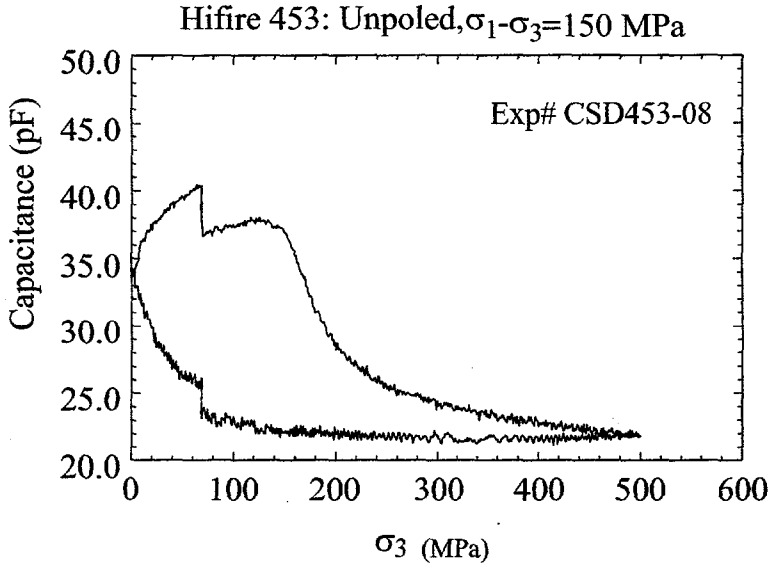

Figure H.22: Capacitance data for experiment CSD453-08, above.

Distribution

Sandia Internal

MS-0303 M. J. Forrestal, 2414
MS-0367 L. W. Carlson, 1833
MS-0367 S. J. Glass, 1833
MS-0443 H. S. Morgan, 9117
MS-0515 F. M. Bacon, 1561
MS-0515 S. G. Barnhart, 1561
MS-0515 T. A. Haverlock, 1561
MS-0515 J. D. Keck, 1561
MS-0515 D. K. Morgan, 1561
MS-0516 G. L. Laughlin, 1564
MS-0521 T. J. Young, 1567
MS-0521 R. A. Damerow, 1567
MS-0521 L. D. Interrante, 1567
MS-0521 S. T. Montgomery, 1567 **(15)**
MS-0521 R. A. Pike, 1567
MS-0521 T. W. Scofield, 1567
MS-0603 I. J. Fritz, 1712
MS-0751 J. M. Grazier, 6117
MS-0751 D. H. Zeuch, 6117 **(15)**
MS-0751 File, 6117
MS-0819 J. S. Peery, 9231
MS-0819 J. R. Weatherby, 9231
MS-0820 P. Yarrington, 9232
MS-0820 R. M. Brannon, 9232
MS-0834 J. B. Aidun, 9117
MS-0953 J. T. Cutchen, 1501
MS-0959 F. P. Gerstle, Jr., 1492
MS-1168 M. D. Furnish, 9321
MS-1181 L. C. Chhabildas, 9511
MS-1349 W. F. Hammetter, 1846
MS-1349 A. J. Hurd, 1841
MS-1405 B. A. Tuttle, 1812
MS-1405 J. A. Voigt, 1846
MS-1411 V. Tikare, 1834
MS-1421 G. A. Samara, 1152
MS-1421 R. E. Setchell, 1152
MS-1434 G. E. Pike, 1802
MS-9006 D. J. Bohrer, 2200
MS-0619 Review & Approval Desk, 15102
for DOE/OSTI
MS-0899 Technical Library, 4916 **(2)**
MS-9018 Central Technical Files, 8940-2